**PSI Proposal No. R-21-02.1**
**Measurement of the Muon Electric Dipole Moment**

M. Giovannozzi
**CERN:** Beams Department, Esplanade des Particules 1, 1211 Meyrin, Switzerland

M. Hoferichter
**UB:** University of Bern, Bern, Switzerland

G. Hiller
**UD:** University of Dortmund, Dortmund, Germany

R. Appleby, I. Bailey
**CI:** *Cockcroft Institute, Daresbury, United Kingdom*

C. Chavez Barajas, T. Bowcock, J. Price, N. Rompotis, T. Teubner, G. Venanzoni, J. Vossebeld
**UL:** University of Liverpool, Liverpool, United Kingdom

R Chislett, G. Hesketh
**UCL:** University College London, London, United Kingdom

N. Berger, M. Köppel[1], A. Kozlinsky, M. Müller[1], F. Wauters
**UMK:** University of Mainz - Kernphysik, Mainz, Germany

A. Keshavarzi, M. Lancaster
**UM:** University of Manchester, Manchester, United Kingdom

F. Trillaud
**UNAM:** Universidad Nacional Autonma de Mexico, Mexico City, Mexico

B. Märkisch
**TUM:** Technical University Munich, Munich, Germany

A. Papa, B. Vitali[1]
**UP:** University and INFN of Pisa, Pisa, Italy

G. Cavoto, F. Renga, C. Voena
**UR:** University and INFN of Roma, Roma, Italy

C. Chen, T. Hu[1], K.S. Khaw, J.K. Ng[1], G.M. Wong[1], Y. Zeng[1]
**SJTU:** Shanghai Jiao Tong University and Tsung-Dao Lee Institute, Shanghai, China

A. Adelmann, C. Calzolaio, R. Chakraborty, M. Daum, A. Doinaki[1], C. Dutsov,
W. Erdmann, T. Hume[1], M. Hildebrandt, H. C. Kästli, A. Knecht, L. Morvaj, D. Reggiani,
A. Rehman, P. Schmidt-Wellenburg[2]
**PSI:** Paul Scherrer Institut, Villigen, Switzerland

K. Kirch[3], M. Sakurai[1,3]
**ETHZ:** ETH Zürich, Switzerland

L. Caminada[3], A. Crivellin[3]
**UZ:** University of Zürich, Zürich, Switzerland

---

[1] PhD student
[2] Spokesperson
[3] also PSI

January 10, 2023

**Contents**

# I. SUMMARY

The Standard Model (SM) of particle physics successfully predicts the fundamental properties and interactions that have been directly tested in many laboratory experiments. However, it is obvious that the model is incomplete and challenged by cosmological observations [1], requiring an extension to explain the origins of matter, dark matter, dark energy, and neutrino masses. Notably, the observed matter-antimatter asymmetry of the Universe [2] hints towards new physics with additional complex phases. In fact, models like baryogenesis or leptogenesis, creating more matter than anti-matter, lead to an additional violation of the combination of charge conjugation and parity symmetry (CP) beyond the SM [3, 4]. In this context, electric dipole moments (EDMs), which violate time-reversal and parity symmetry, and by the virtue of the CPT theorem also CP [5], can test such scenarios.

In this proposal, we describe the first phase of an experiment to search for the EDM of the muon with a sensitivity of $3 \times 10^{-21}\,e\cdot$cm using, for the first time, the frozen-spin technique [6] in a compact storage ring [7]. Furthermore, we give an outlook on a possible second phase with a final precision of better than $6 \times 10^{-23}\,e\cdot$cm. This staged search for a non-zero muon EDM (muEDM) is a unique opportunity to probe previously uncharted territory and to test theories of BSM physics through: ($i$) a roughly three orders of magnitude improvement compared to the current direct experimental limit of $d_\mu < 1.5 \times 10^{-19}\,e\cdot$cm (CL 90%) [8]; ($ii$) a complementary search for an EDM of a bare lepton; ($iii$) a unique test of lepton-flavor symmetries; and ($iv$) in the case of a null result, a stringent limit on an otherwise very poorly constrained Wilson coefficient.

In the first phase, we will establish efficient collaboration and develop all features of the experiment in a precursor experiment capitalizing on an existing solenoid at the Paul Scherrer Institute (PSI). The next five years can be broken down into six major milestones:

**M1** We will demonstrate the injection of muons off-axis into the solenoid. For this purpose we are designing a flow-through cryostat to cool two superconducting shields below their critical temperature. One of the magnetic shields will be made of sheets of Nb-Ti wrapped around a copper tube, while the other magnetic shield will consist of a commercial high-temperature superconductor coiled around another copper tube in a helix. We will then investigate the effectiveness of these two shields by measuring their shielding factors and injection efficiency of muons from piE1_2 into the solenoid. The injection efficiency will be determined by measuring the fraction of muons passing through the injection tube inside the superconducting shields and through the solenoid to the far side.

**M2** To store muons in a stable orbit within the solenoid, we will apply a quadrupole magnetic pulse triggered by a muon entrance trigger mounted downstream of the injection tube. By measuring the time of flight of muons to the center of the solenoid, we will benchmark our Monte Carlo simulations and fine-tune the parameters of the magnetic kicker.

**M3** The quadrupole pulse will generate eddy currents within all conducting surfaces. We will measure the amplitude of the magnetic pulse and the induced eddy currents to correctly account for damping and offset fields. Dedicated correction coils based on magnetic field measurements and fine-tuning of the pulse circuit inductance will allow us to mitigate potential systematic effects.

**M4** By combining the entrance trigger and the magnetic kicker, we will demonstrate the storage of muons inside the solenoid. We will optimize the magnetic kicker timing by measuring the number of muons passing through the solenoid. In a second step we will use the positron detector mounted around the nominal storage orbit to observe muon decays and measure the $g-2$ precession.

**M5** We will apply a radial electric field by charging the central cylindrical electrode at high voltage. By measuring the $(g-2)$-frequency as a function of the electric field, we can adjust the voltage to meet the frozen-spin condition.

**M6** Demonstration of the frozen-spin technique and start of data collection for a new muon EDM result.

This will crosscheck results on the muEDM with a resolution of about a few $1 \times 10^{-21}\,e\cdot$cm expected in the next five years by the FNAL (g-2) the J-PARC (g-2)/muEDM collaborations [9, 10], probing unexplored territory. The experience gained in this initial phase will permit the construction of a new instrument, which will further increase the sensitivity to a muEDM to at least $6 \times 10^{-23}\,e\cdot$cm.

## II.  THE COLLABORATION

In 2022 the collaboration met for the first time in person in Pisa, Italy. Motivated by the successful application for an ERC consolidator grant, groups from England, Germany, Italy, and Switzerland are joining forces for the first and second phase of the experiment. The collaboration is still in an early stage and open to new members. A small theory group is supporting the collaboration studying muon EDM relevant beyond standard model scenarios in effective field theories and concrete models relevant to the muon EDM.

A formal collaboration framework agreement is being prepared and will be signed in early 2023 at the next collaboration meeting.

### A.  University of Bern

Dr. Martin Hoferichter is supporting the theory team of the collaboration.

### B.  CERN

One staff scientist with experience in beam dynamics, beam manipulations and beam injection supports collaboration in optimizing the muon transport beam lines and injection in view of the quality of the muon beam and the efficiency of injection.

CERN plans to contribute to the analysis of the muon beam quality and of the injection of the muon beam in the experimental device. This would entail improvements aimed at increasing the overall efficiency of the injection process, which could be obtained by manipulating the injected beams to reduce their dimensions using non-linear magnets in the transfer lines or tapered capillaries. These studies would be carried out by M. Giovannozzi supervising and hosting students supported by the muEDM collaboration or other sources.

### C.  University of Dortmund

Prof. Dr. Gudrun Hiller supports the theory team of the collaboration.

### D.  Cockcroft Institute

The Cockcroft Institute (Universities of Manchester and Lancaster) has an involvement in the FNAL muon g-2 and Mu2e experiments. CI worked on the collimators for mu2e, and on beam tracking/injection for g-2. For muEDM (as part of the UK effort) CI is interested in delivering the positron tracker DAQ for Phase-I and Phase-II (working with Manchester HEP group), in increasing the overall efficiency of the beam injection and beam modeling. If STFC funding is secured we would be able to provide physicist (faculty, postdoc, student) effort.

### E.  University of Liverpool

The group at the University of Liverpool is actively involved in the FNAL Muon g-2 and Mu2e experiments and in the Mu3e experiment at PSI. The group designed and build the low-mass tracking system for the Muon g-2, delivers HPGe Stopping Target Monitor for Mu2e and is currently involved in the construction of the outer layers of the Mu3e pixel tracker.

For muEDM (as part of the UK effort), the group is planning to contribute to the development and, subject to funding applications, to the construction of the positron tracker for Phase-I and Phase-II. The University of Liverpool particle physics group has a strong track record on the design and construction of silicon tracking detectors. The group operates extensive and well equipped clean room facilities and w mechanical workshop for technology development and detector integration. The group host one of the UK's GRIDPP computing sites and has expertise in detector simulation and the development of track reconstruction algorithms. With other UK groups, Liverpool developing a funding proposal to STFC to support the UK participation in the muEDM project. Prof. Dr. Thomas Teubner is supporting the theory team of the collaboration.

### F.    University College London

Two staff scientists, Prof. Dr. Gavin Hesketh and Prof. Dr. Rebecca Chislett, potentially an electronic engineer, and possibly a fraction of a post doc will contribute to muEDM. The group has expertise on DAQ, clock systems, and low/high voltage supply. As part of a UK effort, UCL delivered the DAQ for the low-mass trackers at FNAL Muon g-2 and the clock system for Mu3e. We currently play a leading role in the muon EDM search at Muon g-2, as well as in developments in tracking algorithms, calibrations, and efficiency optimizations at Muon g-2 and Mu3e. For muEDM, UCL (as part of the UK effort) are interested in delivering the positron tracker DAQ for Phase-I and Phase-II; and developing reconstruction and physics analysis software.

### G.    University of Mainz - Kernphysik

The group at the institute of nuclear physics at JGU Mainz is currently building the data acquisition and filter farm for the Mu3e experiment at PSI and the pixel tracker for the P2 experiment in Mainz. The group also has extensive experience in detector simulation and the development of track reconstruction algorithms, both for on-line and off-line applications. MuEDM ideally complements the group portfolio in low energy precision tests of the Standard Model of particle physics.

The group plans to contribute to the muEDM data acquisition system and to the development of track reconstruction algorithms. If a monolithic pixel detector becomes part of the muEDM setup (Phase-II), the group would also like to contribute to that. At the institute of nuclear physics, mechanical, electronics, vacuum and accelerator workshops are available. In addition there is the detector laboratory of the cluster of excellence PRISMA+ which provides a diverse infrastructure for detector and electronics development, construction and tests as well as expert staff. In terms of computing, Mainz operates the MOGON II and currently builds the MOGON III supercomputers. The group plans to submit a funding proposal to DFG for a PhD student to work exclusively in muEDM, supported and supervised by the senior members of the group.

### H.    University of Manchester

The University of Manchester group has an involvement in the FNAL muon g-2 and Mu2e experiments and the participation in muEDM will be led by Prof. Mark Lancaster and Dr. Alex Keshavarzi. On g-2 the group has led the tracking group and SM theory prediction for muon g-2 and made major contributions to the DAQ. On Mu2e it is providing the DAQ for the HPGe Stopping Target detector. Manchester has a strong track record in silicon tracking having recently provided more than half of the LHCb Velo detector and is providing the detector support structures, cooling and services for the ATLAS endcap pixel detector. The group also hosts one of the largest Tier-2 grid computing sites and this could potentially be utilized by muEDM. For muEDM (as part of the UK effort) Manchester is interested in delivering the positron tracker DAQ for Phase-I and Phase-II and in increasing the overall efficiency of the beam injection working with the Cockcroft Institute as well as utilizing the silicon expertise in the group to define and ultimately build the Phase-2 silicon tracker. If STFC funding is secured we would be able to provide electronic and mechanical engineers in addition to physicist (faculty, postdoc, student) effort.

### I.    Universidad Nacionale Autónoma de México

One research professor, Dr. Frederic Trillaud, working in applied superconductivity with expertise in multiphysics numerical modeling of low temperature and high temperature superconductors and experience in instrumentation and characterization of superconducting systems supports the collaboration in the design of the muEDM superconducting magnet and analysis of its performance compared to its specifications. Part of the activity is the development of a numerical tool for the optimization of the superconducting magnet for trapping and freezing muons and the participation in the design of the superconducting magnetic shields for the injection channel to guide muons inside the superconducting magnet. For the superconducting solenoid magnet, the goal is to find the optimal magnet configuration looking for compactness at a minimum number of solenoids under the requirements of field quality. For the shields, the task revolves around a proof of principle using High temperature superconductors via modeling in close collaboration with colleagues from

the magnet section of the PSI. Depending on fund availability, Dr. Frederic Trillaud could participate in the experimental characterization of the shields. Some support from students is expected with local funding if available. Additional local and joint funding (for instance, Switzerland seed funds) is being explored to cover full or partial travel expenses, laboratory visits, and to invest in high performance computers and licenses of commercial software.

## J.    Technical University Munich

Prof. Dr. Bastian Märkisch will contribute to the muEDM project and is available to supervise and support PhD and undergraduate students. The Munich group has expertise in conventional (PERKEO III) and superconducting magnet systems (PERC) for precision measurements of decay correlations in neutron beta decay. The group intends to contribute to the magnetic field characterization, optimization and monitoring as well as the design of the Phase-II magnet. The mechanical workshops at the department will support the project. We seek to extend the already available funding for investment and one PhD position to work on magnetic fields for low energy precision measurements by a DFG proposal.

## K.    INFN Pisa and Rome, University of Pisa and "Sapienza" University of Rome

The INFN groups in Pisa and Rome are active in the MEG experiment at PSI and pursue R&D activities for particle detectors in precision experiments and rare event searches. The Pisa group has a deep expertise in the development of position, energy and time sensitive detectors based on gas, scintillating materials and photon detectors, including mechanics, electronics and DAQ. The Rome group is active in the development of gaseous detectors exploiting different technologies, from wires to micro-pattern structures, including the design, construction and management of detector services (gas system, high voltage, etc.). Both groups have extensive experience in detector simulation, event reconstruction and physics analysis.

The groups plan to contribute to the development of muon entrance detectors for trigger and beam characterization down to the storage orbit. We also intend to contribute to the positron tracking system, taking care of the construction of a time and position sensitive detector based on scintillating fibers coupled to silicon photosensors. Our expertise will also be beneficial in contributing to simulations and analysis tasks. The academic staff at University of Pisa and "Sapienza" University of Rome will support and supervise master and PhD students.

We intend to submit a proposal to INFN in Spring 2023, asking for scientific and financial support over the entire duration of the muEDM project, and seek competitive national grants with our Universities' support. If these proposals are approved, INFN and University infrastructures (workshops, laboratories, etc.) and technical staff will also be available.

## L.    Shanghai Jiao Tong University

The Muon Physics group at the Tsung-Dao Lee Institute of Shanghai Jiao Tong University is actively involved in the Fermilab Muon $g-2$ experiment, and the participation in the muEDM Collaboration will be led by Prof. Dr. Kim Siang Khaw. Our group is involved in the data reconstruction and data analysis for the anomalous precession frequency in the $g-2$ experiment, a search for the muon EDM using calorimeter information, and machine learning approaches for a fast muon $g-2$ simulation. For muEDM experiment, our group has contributed to the initial GEANT4 simulation of the frozen-spin technique and recently a prototype of the muon entrance detector based on scintillators and SiPMs. We are interested in contributing to the scintillator-based detector technology (plastic scintillators from GNKD, Beijing and ELJEN, USA, SiPMs from NDL, Beijing, customized electronics circuits and 3D printing) and/or simulation (GEANT4 and G4BEAMLINE) and data analysis (ROOT) tasks of the collaboration. We had successfully obtained funding from the National Natural Science Foundation of China (NSFC) from 2021 to 2022 and we will continue to apply for another round of funding from 2024 to 2025 and beyond. We will commit at least two FTE Master/PhD students towards the realization of Phase-I muEDM.

## M.   Paul Scherrer Institute

The laboratory of particle physics (LTP) of the PSI has an excellent track record on difficult high precision experiments using ultra cold neutrons (UCN), muons, and pions of the secondary beam lines of the high intensity proton accelerator. The spokesperson and initiator of the project has received an ERC consolidator grant in 2022 for the muon EDM experiment at PSI. Together with a project grant awarded by SNF, a total of three post-docs and three PhD students are hired for the project in the next years. The post-docs have a background in detector physics, $(g-2)$ analysis at FNAL, and 3D muon injection $(g-2)$ at JPARC. Further, several permanent staff members from the muon, high energy, and detector groups of LTP are contributing at a lower percentage to the project, building on their expertise and knowledge of PSI's secondary beam lines and complex detector designs. In addition, the project is supported by the cryogenic magnets and the pulsed magnets groups of the division for large infrastructure (GFA) at PSI. Their knowledge and expertise support the design, testing, and construction of the superconducting tube and the pulsed coil of the experiment. At a later stage they are interested in designing and procuring the dedicated solenoid based on high temperature super conductors for the Phase-II experiment. The workshops and groups for mechanical, electronics, and vacuum technology will support the project similarly as they have done for other LTP based research.

## N.   ETH Zürich

The group at ETH Zürich is heavily involved in several muon and neutron experiments at PSI. In the muon EDM project Prof. Dr. Klaus Kirch will be available for the academic supervision of PhD students employed by PSI. He will also continue the academic supervision of Master and Bachelor students contributing to the project. At the institute of particle physics and astrophysics, mechanical and electronics workshops are available for the muon EDM project.

## O.   University Zürich

Dr. Andreas Crivellin, also at PSI, is supporting the theory team of the collaboration. Prof. Dr. Lea Caminada is head of the PSI high energy group and has significantly contributed with her group to design and realization of the CMS central silicon pixel tracker. Together with the PSI high energy group she is interested in contributing to the development of a HV-MAPS based positron tracker for Phase-II. She will guarantee academic supervision for students working on the silicon pixel based positron detector.

## III. INTRODUCTION AND MOTIVATION

Symmetries [11], and their breaking [12–14], played an essential role in the formulation of today's Standard Model (SM) of Particle Physics. In addition to the local gauge symmetries describing the fundamental interactions of matter, i.e., the weak, strong, and electromagnetic force, the SM possesses several (approximate) global symmetries. Among them is the symmetry of combined charge-conjugation and parity-inversion (CP), which is broken only by weak interactions through the phase of the Cabibbo-Kobayashi-Maskawa matrix [15], parameterized in a basis-independent manner by the Jarlskog determinant [16]. As the impact of this phase on observables is suppressed by the masses of the electroweak gauge bosons, the effect is small. In fact, although this phase is close to maximal [17], the resulting values of EDMs that can be accessed in an experiment are far too small [18, 19] for detection anytime soon. However, CP violation in the SM is known to be insufficient to explain the observed matter-antimatter asymmetry.

Therefore, observables measuring CP violation are very sensitive probes of Beyond Standard Model (BSM) physics. In particular, EDMs of fundamental particles violate time-reversal and, invoking the CPT-theorem [5], also CP symmetry, making them excellent BSM probes (see, e.g., Ref. [20] for a review). Already 70 years ago, E.M. Purcell, N.F. Ramsey and their student J.H. Smith [21] published a search for an EDM of the neutron. Only a year later, the first search for a muon EDM was completed [22]. Since then, many searches around the world have been concluded with increasing sensitivity on neutrons, atoms, and molecules [23, 24]; however, all have so far found only null results. Furthermore, while no new particles were found at the LHC yet [25, 26], most interesting hints for BSM physics appeared in several precision measurements, in particular those involving muons (see, e.g., Refs. [27–29] for recent overviews). These hints for new physics suggest a flavor structure beyond minimal flavor violation (MFV) in the lepton sector [30].

In fact, within MFV, as often implemented within the Minimal Supersymmetric Standard Model (MSSM), a simple scaling by the ratio $m_\mu/m_e$ is predicted [31–34], so that the electron EDM, $d_e \leq 1.1 \times 10^{-29} \, e \cdot$cm (95% C.L.) [35, 36] would place severe limits on its muon counterpart. However, MFV is, to some extent, an ad hoc symmetry, mainly invented to allow light particle spectra within the MSSM to reduce the degree of fine-tuning in the Higgs sector, while respecting at the same time flavor constraints, and is challenged by the current BSM hints in the flavor sector. Therefore, this relation does not hold in theories with a flavor structure beyond the MFV paradigm, thus allowing, in general, for a sizable muon EDM. Furthermore, if one takes into account the new-physics effect suggested by the comparison of the measurement and the SM prediction for $g-2$ of the muon [37, 38], one can see in a model-independent effective-field-theory approach—in which the imaginary (real) part of the respective Wilson coefficient is related to the electric dipole (anomalous magnetic) moment of the muon, respectively—that a phase of order one predicts a sizable EDM [39, 40], see Fig. 1, within reach of a dedicated experiment.

Such an experiment will test this intrinsic connection of the muon EDM with $g-2$ of the muon in a conclusive manner; in fact, the direct limit of the muon EDM $d_\mu < 1.5 \times 10^{-19} \, e \cdot$cm (CL 90%) [8] is the only EDM of a fundamental particle probed directly on the bare particle. Indirect limits derived from $d_e$ via CP-odd insertions in three-loop diagrams [40–42] slightly improve the current direct limit and provide another target for a dedicated search.

From a model-building perspective, a key point is that $\mu \to e\gamma$ transitions need to be avoided, but this is possible by disentangling the muon from the electron sector via a symmetry, such as a $L_\mu - L_\tau$ symmetry [43–45], which, even after breaking, protects the electron EDM and $g-2$ from BSM contributions [46]. Furthermore, it is possible to obtain a significant effect in muon $g-2$ and EDM without incurring significant fine-tuning related to the muon Yukawa coupling [47], while the observable consequences of scenarios with large EDMs in $h \to \mu\mu$ and $Z \to \mu\mu$ could be investigated in future colliders [48]. Finally, from an EFT perspective [40, 49, 50], it is clear that the muon EDM is not constrained by other observables and that its measurement is the only way of determining the imaginary part of the associated Wilson coefficient.
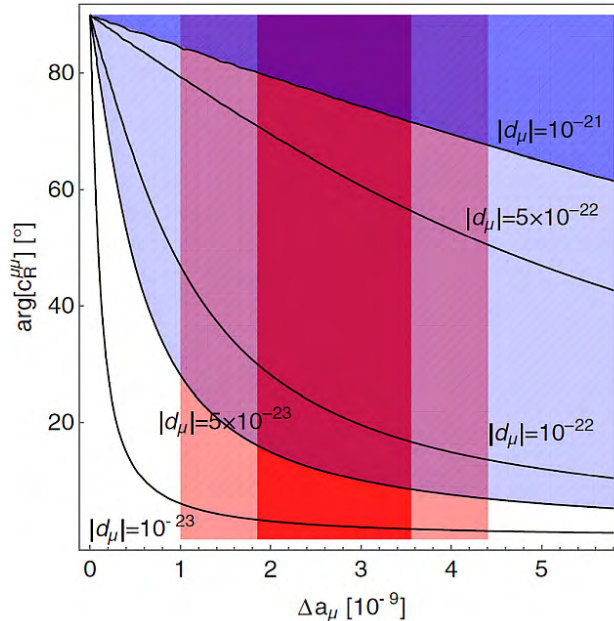
Figure 1: Contours of $d_\mu$ as a function of the anomalous magnetic moment $\Delta a_\mu$ and the phase of the associated Wilson coefficient [40].

## IV. THE FROZEN-SPIN TECHNIQUE

### A. Spin motion of muons with an EDM in electromagnetic fields

The spin dynamics of a muon at rest in a magnetic field $\vec{B}$ is described by $\mathrm{d}\vec{s}/\mathrm{d}t = \vec{\mu} \times \vec{B} = \vec{\omega}_\mathrm{L} \times \vec{s}$ where $\vec{\mu} = ge/(2m)\vec{s}$ is the magnetic dipole moment with $|\vec{s}| = \hbar/2$ and $\vec{\omega}_\mathrm{L} = -2\mu\vec{B}/\hbar$ the Larmor precession frequency. Similarly, a hypothetical EDM $\vec{d} = \eta e/(2mc)\vec{s}$ results in a spin precession of the muon $\vec{\omega}_d = -2d\vec{E}/\hbar$ in an electric field $\vec{E}$.

The first search for a muon EDM, the second EDM result in history, resulted in an upper limit of $2.9 \times 10^{-15}\, e{\cdot}\mathrm{cm}$ (95% C.L.) [22] and was published in 1958. Half a century later, the current best upper limit of $d_\mu < 1.8 \times 10^{-19}\, e{\cdot}\mathrm{cm}$ (95% C.L.) [8] was deduced using the spin precession data from the $(g-2)$ storage ring experiment E821 at BNL [51].

For further discussion of the spin dynamics of a moving muon with momentum $\vec{p}$, $\vec{\beta} = \vec{v}/c$ and $\gamma = (1-\beta^2)^{-1/2}$ in magnetic, $\vec{B}$, and electric, $\vec{E}$, fields, it is useful to change to the unit polarization three vector, namely $\vec{\Pi} = \vec{s}/|\vec{s}|$. Then the change in polarization with time is given by

$$\frac{\mathrm{d}\vec{\Pi}}{\mathrm{d}t} = \vec{\Omega}_0 \times \vec{\Pi}, \tag{1}$$

where

$$\vec{\Omega}_0 = -\frac{e}{m\gamma}\left[ (1 + \gamma a)\,\vec{B} - \frac{a\gamma^2}{(\gamma+1)}\left( \vec{\beta} \cdot \vec{B} \right)\vec{\beta} - \gamma\left( a + \frac{1}{\gamma+1} \right)\frac{\vec{\beta} \times \vec{E}}{c} \right] \tag{2}$$

is the Thomas precession [52], when replacing the anomalous moment of the muon $a$ [51] with $(g-2)/2$ and the parameter $\lambda$ in [52] by $ge/(2mc)$.

In the case that no electric field is applied parallel to the momentum, the acceleration of the muon is purely transverse to its motion

$$\frac{\mathrm{d}\vec{\beta}}{\mathrm{d}t} = \frac{e}{\gamma mc}\left( \vec{E} + \vec{\beta} c \times \vec{B} \right), \tag{3}$$

which is equivalent to

$$\frac{\mathrm{d}\vec{\beta}}{\mathrm{d}t} = \vec{\Omega}_c \times \vec{\beta}, \tag{4}$$

where

$$\vec{\Omega}_c = -\frac{e}{m\gamma}\left(\vec{B} - \frac{\gamma^2}{\gamma^2 - 1}\frac{\vec{\beta} \times \vec{E}}{c}\right) \tag{5}$$

is the cyclotron frequency.

The relative spin precession $\vec{\Omega}$ of a muon in a storage ring with an electric field $\vec{E}$ and a magnetic field $\vec{B}$ is then given by the following:

$$\vec{\Omega} = \vec{\Omega}_0 - \vec{\Omega}_c = \frac{q}{m}\left[a\vec{B} - \frac{a\gamma}{(\gamma + 1)}\left(\vec{\beta} \cdot \vec{B}\right)\vec{\beta} - \left(a + \frac{1}{1 - \gamma^2}\right)\frac{\vec{\beta} \times \vec{E}}{c}\right], \tag{6}$$

which is the well-known Thomas-BMT equation [52, 53] when replacing $q = -e$. The presence of the EDM adds a second term

$$\begin{aligned}\vec{\Omega} = &\frac{q}{m}\left[a\vec{B} - \frac{a\gamma}{(\gamma + 1)}\left(\vec{\beta} \cdot \vec{B}\right)\vec{\beta} - \left(a + \frac{1}{1 - \gamma^2}\right)\frac{\vec{\beta} \times \vec{E}}{c}\right] \\ &+ \frac{\eta q}{2m}\left[\vec{\beta} \times \vec{B} + \frac{\vec{E}}{c} - \frac{\gamma c}{(\gamma + 1)}\left(\vec{\beta} \cdot \vec{E}\right)\vec{\beta}\right].\end{aligned} \tag{7}$$

The first line of Eq. (7) is the anomalous precession frequency $\omega_a$, the difference between the Larmor precession and the cyclotron precession. The second line is the precession $\omega_e$ due to the EDM coupling to the relativistic electric field of the muon moving in the magnetic field $\vec{B}$, oriented perpendicular to $\vec{B}$.

If momentum, magnetic field, and electric field form an orthogonal basis, the scalar products of momentum with the fields, $\vec{\beta} \cdot \vec{B} = \vec{\beta} \cdot \vec{E} = 0$, drop out. A special configuration was chosen for the E821 experiment, namely muons with a so-called "magic" momentum of $p_{\text{magic}} = m/\sqrt{a} = 3.09\,\text{GeV}/c$ were used, simplifying Eq. (7) on the reference orbit to

$$\vec{\Omega} = \frac{q}{m}\left[a\vec{B} + \frac{\eta}{2}\left(\vec{\beta} \times \vec{B} + \frac{\vec{E}}{c}\right)\right], \tag{8}$$

thus making the anomalous precession frequency independent of the electric fields needed for steering the beam. In the presence of a muon EDM, the precession plane is tilted out of the orbital plane defined by the movement of the muon in this "magic" configuration. Therefore, a longitudinal precession ($\vec{\omega}_e \perp \vec{B}$) with an amplitude proportional to the EDM and a frequency $\vec{\omega}_e$, shifted in phase by $\pi/2$ with respect to the transverse anomalous precession, would become observable. Another effect of an EDM is the increase of the observed precession frequency

$$\Omega = \sqrt{\omega_a^2 + \omega_e^2}. \tag{9}$$

## B. The frozen-spin technique

The experimental setup proposed for this dedicated search for a muon EDM is based on the ideas and concepts discussed in [6, 7]. The salient feature of the proposed search for this hypothetical muon EDM is the cancelation of the effects from the anomalous moment by meticulously choosing a radial electric field and thus fully exploiting the large electric field $\vec{E}^* = \gamma c\vec{\beta} \times \vec{B} \approx 1\,\text{GV/m}$ in the rest frame of the muon, to achieve a perpendicular precession ($\vec{\omega}_e \perp \vec{B}$) only. Here, as in the remainder of this document, the fields in the rest frame of the particle will be indicated by an $*$ while in all other cases fields are assumed to be in the laboratory frame.

The anomalous precession term in Eq. (7) can be set to zero by applying an electric field such that

$$a\vec{B} = \left(a - \frac{1}{\gamma^2 - 1}\right)\frac{\vec{\beta} \times \vec{E}}{c}. \tag{10}$$

In the idealized case of $\vec{\beta} \cdot \vec{B} = \vec{\beta} \cdot \vec{E} = 0$, and $\vec{B} \cdot \vec{E} = 0$ we find a required field strength of $E_{\mathrm{f}} \approx aBc\beta\gamma^2$. By selecting the exact field condition of Eq. (10), the cyclotron precession frequency is modified such that the relative angle between the momentum vector and the spin remains unchanged if $\eta = 0$, and hence it is "frozen". In the presence of an electric dipole moment, the change in polarization is described by

$$\frac{\mathrm{d}\vec{\Pi}}{\mathrm{d}t} = \vec{\omega}_e \times \vec{\Pi}, \tag{11}$$

where

$$\vec{\omega}_e = \frac{\eta q}{2m}\left[\vec{\beta} \times \vec{B} + \frac{\vec{E}_{\mathrm{f}}}{c}\right]$$

$$= \frac{2d_\mu}{\hbar}\left(\vec{\beta}c \times \vec{B} + \vec{E}_{\mathrm{f}}\right) \tag{12}$$

is the precession frequency due to the muon EDM. For the idealized case, see above, this results in a longitudinal build-up of the polarization

$$|\vec{\Pi}(t)| = P(t) = P_0 \sin\left(\omega_e t\right) \tag{13}$$

$$\approx P_0 \omega_e t$$

$$\approx 2P_0 \frac{d_\mu}{\hbar}\frac{E_{\mathrm{f}}}{a\gamma^2}t. \tag{14}$$

From the slope

$$\frac{\mathrm{d}P}{\mathrm{d}d_\mu} = \frac{2P_0 E_{\mathrm{f}} t}{a\hbar\gamma^2} \tag{15}$$

multiplied by the mean analysis power of the final polarization, $A$, we calculate the sensitivity as

$$\sigma(d_\mu) = \frac{a\hbar\gamma}{2P_0 E_{\mathrm{f}}\sqrt{N}\tau_\mu A} \tag{16}$$

for a search for the muon EDM by replacing $t$ with the mean free laboratory lifetime of the muon in the detector $\gamma\tau_\mu$ and scaling by $1/\sqrt{N}$ for the Poisson statistics of $N$ observed muons.

## V. STATISTICAL SENSITIVITY

The frozen-spin technique benefits from a continuous build-up of the phase $\omega_e t$ and results in a high statistical sensitivity, see Eq. (16). Two scenarios are considered at PSI. In the first phase, we will use surface muons with $p \approx 28\,\mathrm{MeV/c}$ from $\pi$E1, while in the final setup we aim to benefit from the high muon flux and the higher muon momentum of $p = 125\,\mathrm{MeV/c}$ at $\mu$E1.

The initial polarization $P_0 \approx 0.95$ of a beam of muons from backward decaying free pions was measured for a momentum of $125\,\mathrm{MeV}/c$ muons on the $\mu$E1 beam line, see Sec. X A. At $\pi$E1 the polarization is typically above 95%, regularly measured in $\mu$SR experiments. For the mean decay asymmetry, we take the average value of the positron spectrum as $A = 0.3$. In a magnetic field of 3 T this results in an EDM sensitivity for a single muon of $\sigma(d_\mu) \approx 2\times10^{-16}\,e\cdot\mathrm{cm}$ and $\sigma(d_\mu) \approx 5\times10^{-17}\,e\cdot\mathrm{cm}$, for $\pi$E1 and $\mu$E1 respectively, which in turn results in an electric field for the frozen-spin condition of $E_\mathrm{f} = 0.3\,\mathrm{MV/m}$ and $E_\mathrm{f} = 1.9\,\mathrm{MV/m}$, respectively.

In both phases, we will inject the muons off-axis along the solenoid field directions. For a high injection rate, the muons need to pass through a dedicated collimation channel, which also includes a magnetic shield made of superconductors, as the acceptance phase space would be extremely small without the magnetic shield due to the magnetic mirror effect. The muons then spiral along the magnetic field to the center of the solenoid, where a quadrupole magnetic kick within the weakly-focusing field region will twist the muon momentum onto a stable storage orbit. This longitudinal injection, also known as vertical injection, was first described in Ref. [54] and benefits from the advantage that the injection channel is far from the magnetically sensitive muon storage region and from a long delay, of the order of about 100 ns, between detecting a suitable muon using an entrance detector and the application of the magnetic kick. Table I summarizes all necessary factors for the statistical sensitivity in both phases.

The statistical sensitivity could be further improved by increasing the muon momentum to $p = 140\,\mathrm{MeV/c}$ and recovering a muon flux greater than $2 \times 10^8\,\mathrm{s}^{-1}$, which was measured in the 1990s.

|  | $\pi$**E1** | $\mu$**E1** |
|---|---|---|
| Muon flux ($\mu^+/s$) | $4 \times 10^6$ | $1.2 \times 10^8$ |
| Channel transmission | 0.03 | 0.005 |
| Injection efficiency | 0.017 | 0.60 |
| Muon storage rate (1/s) | $2 \times 10^3$ | $360 \times 10^3$ |
| Gamma factor $\gamma$ | 1.04 | 1.56 |
| $e^+$ detection rate (1/s) | 500 | $90 \times 10^3$ |
| **Detections per 200 days** | $8.64 \times 10^9$ | $1.5 \times 10^{12}$ |
| Mean decay asymmetry $A$ | 0.3 | 0.3 |
| Initial polarization $P_0$ | 0.95 | 0.95 |
| **Sensitivity in one year** ($e\cdot$cm) | $<3 \times 10^{-21}$ | $< 6 \times 10^{-23}$ |

Table I: Annual statistical sensitivity of the muon EDM measurement of phase I and II.

## VI.  SYSTEMATIC EFFECTS

The main aim of the frozen-spin technique is to select an electric field such as to cancel the effects of the anomalous magnetic moment and to ensure that any residual precession is due to the EDM. However, in a real storage ring the anomalous precession cannot be perfectly canceled, and EDM-like precession can be induced by coupling of the magnetic dipole moment (MDM) to the electromagnetic (EM) fields of the experimental setup, which would be an example of a real spin precession systematic effect. The presence of systematic effects can also lead to an apparent precession of the spin even in the absence of such effects, for example, due to changes in the sensitivity or acceptance of the detector system on the time scale of the measurement. In this section we will outline possible effects that lead to a real or apparent precession of the spin, but that are not related to the EDM.

To evaluate systematic effects related to the EM fields in the experiment, it is necessary to study the relativistic spin motion in electric $\vec{E}$ and magnetic $\vec{B}$ fields described by the Thomas-BMT Eq. (7).

The coordinate system used throughout this work is such that it follows the reference particle orbit (similar to [55, 56]) and is sketched in Figure 2.

Using Eq. (7) and assuming that $\vec{\beta} \cdot \vec{E} = 0$ and $\vec{\beta} \cdot \vec{B} = 0$ the angle of spin precession around the radial axis due to a non-zero EDM is:

$$\Theta(t) = \left(\vec{\Omega}_{\text{EDM}}\right)_x t = \frac{\eta}{2}\frac{e}{m_0}\beta_z B_y t, \tag{17}$$

where $t$ is the time elapsed between the injection of the muon into the longitudinal magnetic field and its decay.

The relationship between the dimensionless parameter $\eta$ that characterizes the spin precession and the EDM $d_\mu$ is given by:

$$d_\mu = \frac{e\hbar}{4m_0 c}\eta. \tag{18}$$

Combining Eqs. (17) and (18) gives an expression for the rate of change of the angle of rotation of the spin $\dot{\Theta}$ as a function of the EDM $d$:

$$\dot{\Theta} = \frac{2c}{\hbar}\beta_z B_y d_\mu. \tag{19}$$

For the precursor and final experiments $\beta_z = 0.26$ and $0.77$, respectively, and $B_y = 3$ T, and therefore the angular velocity for an EDM equal to the statistical sensitivity is:

$$\dot{\Theta} = 21.15 \text{ rad/s, for } d_\mu = 3 \times 10^{-21}\ e \cdot \text{cm and} \tag{20}$$

$$\dot{\Theta} = 1.26 \text{ rad/s, for } d_\mu = 6 \times 10^{-23}\ e \cdot \text{cm.} \tag{21}$$

In the following sections, we require that the observed angular velocity of the spin precession due to systematic effects be less than the experimental sensitivities shown in Eqs. (20) and (21).
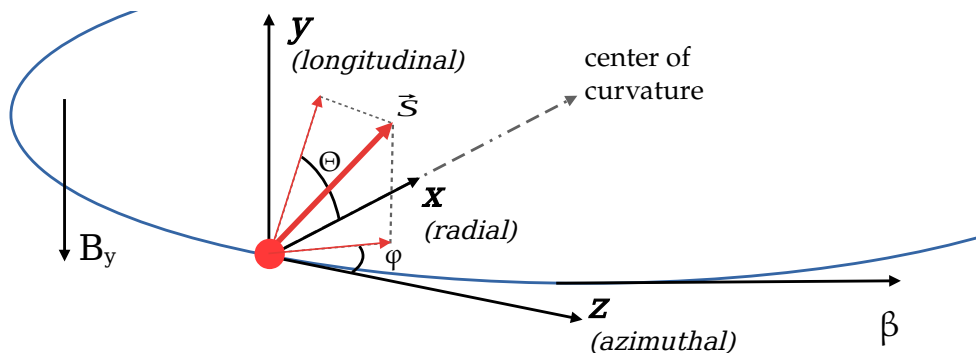


Figure 2: The local reference coordinate system used to derive the motion of the spin in the EM fields of the experiment. The vector $z$ follows the momentum of the muon and $y$ always points along the longitudinal direction defined by the main solenoid magnetic field $B_y$.

## A. Sources of real spin precession

As a starting point of the analysis of real spin precession, we will describe analytically the motion of the spin due to the combined effect of ideal approximations of the magnetic field of the solenoid, the weakly-focusing field, and the electric field used in the frozen-spin method. The magnetic field of the solenoid is approximated as a uniform magnetic field oriented along the $y$ axis. The weakly-focusing field is described by the approximated field generated by a circular coil. The electric field is assumed to be a radial field generated from the potential difference between two infinite coaxial cylindrical electrodes. Some possible and most important imperfections of these fields and their effect on the spin precession are discussed below.

### 1. Spin precession along the radial axis

Assuming that the particles follow a trajectory with constant radius $\rho$, the radial magnetic field $B_x(y)$ of a cylindrical coil with $N$ turns and radius $R$ along that trajectory can be approximated by [57]:

$$B_x(y) = \frac{3}{2}\mu_0 N I R^2 \frac{\rho y}{\left(R^2 + y^2\right)^{\frac{5}{2}}}, \tag{22}$$

where $I$ is the current that passes through the coil and $\mu_0$ is the magnetic permittivity of the vacuum. Expanding (22) into a Taylor series, one obtains:

$$B_x(y) = \Phi_0 \rho y - \frac{5}{2}\frac{\Phi_0}{R^2}\rho y^3 + \mathcal{O}(y^5), \text{ where } \Phi_0 = \frac{3}{2}\frac{\mu_0 N I}{R^3}. \tag{23}$$

The longitudinal position of a particle with charge $e$, mass $m_0$, and velocity $c\vec{\beta}$ is given by the solution of:

$$\ddot{y} = \frac{1}{\gamma m_0}\left(e E_y + c\beta_z B_x(y)\right), \tag{24}$$

where we assume a constant non-zero longitudinal component of the electric field. Limiting Eq. (23) to the linear term in the series, the solution of the differential equation is the harmonic oscillator:

$$y(t) = y_0 \cos(\omega_\beta t + \varphi) + \frac{1}{\Phi_0 \rho}\frac{E_y}{c\beta_z}, \tag{25}$$

$$\text{where } \omega_\beta = \sqrt{\Phi_0 \frac{ec\beta_z}{\gamma m_0}\rho} \tag{26}$$

is the angular velocity of the vertical betatron oscillations (VBO). For the precursor experiment $\beta = 0.258$ and $\gamma = 1.03$, therefore, the period $T = 2\pi/\omega_\beta$ of the VBO is approximately $600\,\text{ns}$.

The precession of the spin due to the coupling of the MDM with the radial magnetic field due to the weakly-focusing field is:

$$\left(\vec{\Omega}_{\text{MDM}}^{\text{WF}}\right)_x = -\frac{ea}{m_0}B_x(y(t)) = -\frac{ea}{m_0}\left[\Phi_0 \cos(\omega_\beta t + \phi_0)\rho y_0 - \frac{1}{c\beta_z}E_y\right]. \tag{27}$$

The other source of radial precession that has to be considered is the radial magnetic field in the reference frame of the muon due to the non-zero longitudinal electric field in the laboratory reference frame. Using the Thomas-BMT equation and taking only the radial component of the spin precession due to the electric field, one obtains the following

$$\left(\vec{\Omega}_{\text{MDM}}^{E_y}\right)_x = -\frac{e}{m_0 c}\left(a - \frac{1}{\gamma^2 - 1}\right)\beta_z E_y. \tag{28}$$

Combining Eqs. (27) and (28), and including a term for an arbitrary radial magnetic field $B_x$, for the total angular velocity of the radial precession due to the MDM around the $x$ axis, one obtains:

$$\left(\vec{\Omega}_{\text{MDM}}\right)_x = -\frac{ea}{m_0}\left[\frac{1}{c}\left(1 - \frac{1}{a(\gamma^2 - 1)} - \frac{1}{\beta_z^2}\right)\beta_z E_y + \Phi_0 \cos(\omega_\beta t + \phi_0)\rho y_0 + B_x\right]. \tag{29}$$

We are interested in the average angular velocity over many muon orbits. In this case, the average due to
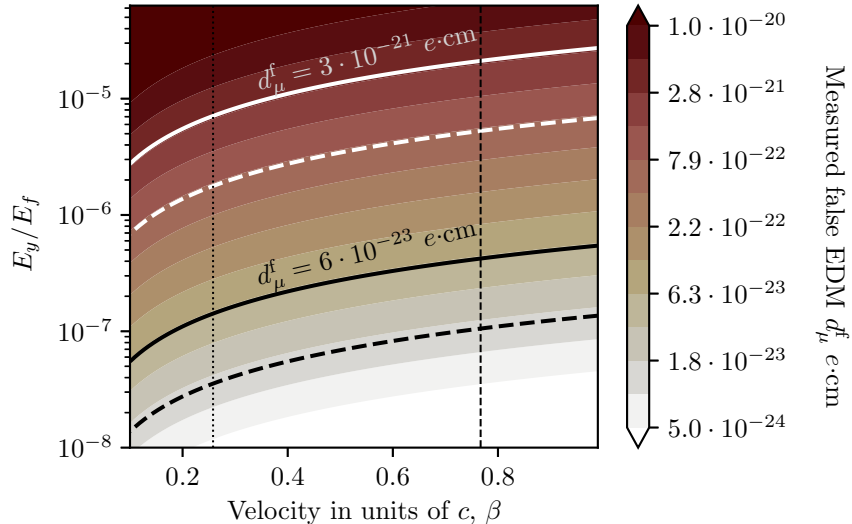
Figure 3: The measured false EDM due to non-zero average electric field in the vertical direction. The solid horizontal line shows the target sensitivity for the true EDM and the dashed horizontal line is one quarter of that value. The vertical dotted line is at $\beta = 0.258$ as for the precursor experiment and the vertical dashed line is at $\beta = 0.767$ as for the final experiment.

the betatron oscillations is zero, as $\langle \cos x \rangle = 0$. The azimuthal velocity $\beta_z$ and the longitudinal electric field $E_y$ are not correlated, thus the average of their product is the product of their averages:

$$\langle (\vec{\Omega}_{\text{MDM}})_x \rangle = -\frac{ea}{m_0 c} \left\langle \left( 1 - \frac{1}{a(\gamma^2 - 1)} - \frac{1}{\beta_z^2} \right) \beta_z \right\rangle \langle E_y \rangle + \frac{ea}{m_0} \langle B_x \rangle. \tag{30}$$

Note that $E_y$ and $B_x$ need not be static uniform fields. What determines the average angular velocity is their averaged value over the muon orbits.

*a. Systematic effects related to the non-zero average longitudinal E-field*

Considering the E-field, one can analyze two different cases: one in which there is only a clockwise (CW) or counterclockwise (CCW) injection scheme, and a scheme in which CW and CCW injection is alternated. In the former case, the relevant average azimuthal velocity will be the average of the velocity of the muons used for the experiment. For the precursor phase $\beta = 0.258$ and for the final experiment $\beta = 0.767$. This situation leads to strict limits on the magnitude of the longitudinal component of the E-field, shown in Fig. 3.

These limits can be significantly improved by alternating between CW and CCW injections. The azimuthal velocity will change sign between the two and the average over all muon orbits will be zero if the mean absolute velocity is the same for CW and CCW injections. Under the condition that there is no correlation between $E_y$ and $\beta_z$, the limit on the difference between the average azimuthal velocities can be derived. The false EDM signal as a function of this difference and the magnitude of the average longitudinal electric field is shown in Fig. 4a for the precursor experiment and in Fig. 4b for the final experiment. This shows that for a 0.5% target level of control on the average momentum between CW and CCW injections (140 keV at 28 MeV/$c$) the average longitudinal E-field component in the storage ring region must be kept below $3 \times 10^{-4}$. For a similar momentum resolution in the final phase (125 keV at 125 MeV/$c$) the limit is $7 \times 10^{-5}$. A discussion on the E-field uniformity with regard to the systematic effects is given in Sec. VI A 3.

*b. Systematic effects related to the presence of time-variable radial B-field*

Alternating the injection directions does not cancel the systematic effects related to radial B-fields. However, the presence of a constant radial B-field will just shift the position of the average orbit and will not introduce a systematic effect. This is not the case for time-varying fields, as the average orbit will move with time and
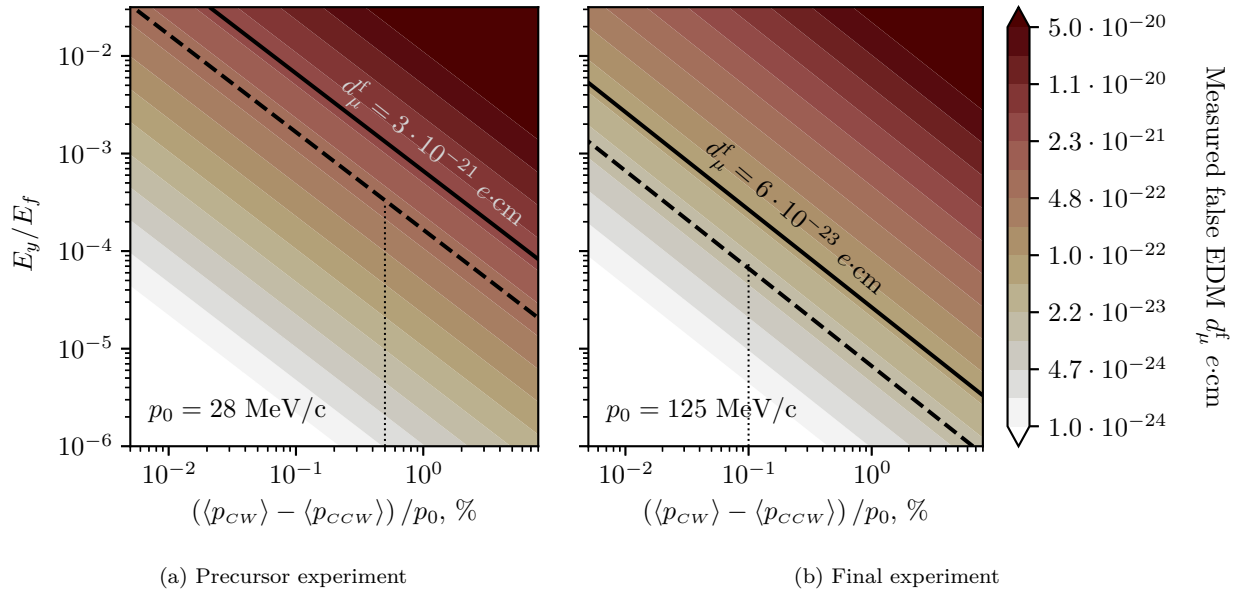
(a) Precursor experiment

(b) Final experiment

Figure 4: Limit on the difference of the average momentum between CW and CCW injection for the precursor and final experiments. The dashed lines show the level of control on the average momentum that is targeted, 0.5% and 0.1%, respectively.

the induced spin precession will not have a zero average. Such time-varying radial B-fields can be expected due to residual radial magnetic fields from the magnetic kick used to store the muons in a stable orbit (see Sec. VII E).

We assume that the residual radial magnetic field due to the magnetic kick reduces exponentially with time:

$$B_x(t) = k B_x^{(\mathrm{peak})} e^{-t/\tau_B}, \tag{31}$$

where $\tau_B$ is the decay constant of the magnetic pulse, $B_x^{(\mathrm{peak})}$ is the magnetic field intensity at the peak of the magnetic kick and $k \in [0,1]$ is a coefficient that characterizes the magnetic field intensity at the start of the exponential decay. Note that the residual field will also contain high-frequency oscillations. Their average over the measurement time of several microseconds tends to zero and so does the average spin rotation caused by them. The geometric phase accumulated from high-frequency B-field oscillations is covered in Sec. VI B.

For a half-sine magnetic pulse with a half-period of the sine wave $T_k$ the peak magnetic field intensity is:

$$B_x^{(\mathrm{peak})} = \frac{\pi}{2} \frac{p_y}{e\beta c^2 T_k}, \tag{32}$$

where $p_y$ is the momentum of the particle in the $y$ direction when entering the weakly-focusing field area. It is related to the muon momentum $\vec{p}$ and the longitudinal pitch angle $\alpha_\mathrm{L}$ as $p_y = |\vec{p}|\alpha_\mathrm{L}$. The longitudinal pitch angle is the angle by which the kicker must rotate the muon momentum to store the muon in the weakly-focusing field.

Combining Eqs. (29) and (31), the angular velocity of the spin precession due to the residual magnetic field is then:

$$\Omega_x(t) = -\frac{ea}{m_0} \frac{\pi}{2} \frac{|\vec{p}|\alpha_\mathrm{L}}{T_k \beta c^2} k e^{-t/\tau_B}. \tag{33}$$

Assuming some values for $k$ and $T_k$ one can calculate the false EDM signal that would be observed at a given point in time as a function of the longitudinal pitch angle. For $k = 10\%$ and $T_k = 100$ ns at $t = \tau_\mu$ the false EDM signal $d_\mu^\mathrm{f}$ as a function of the time constant $\tau_B$ and the longitudinal pitch angle $\alpha_\mathrm{L}$ is shown in Figs. 5a and 5b.

The calculation shows that the systematic effect is only weakly dependent on the longitudinal pitch angle, and thus on the magnetic pulse strength, while the decay dominates. To avoid a significant contribution
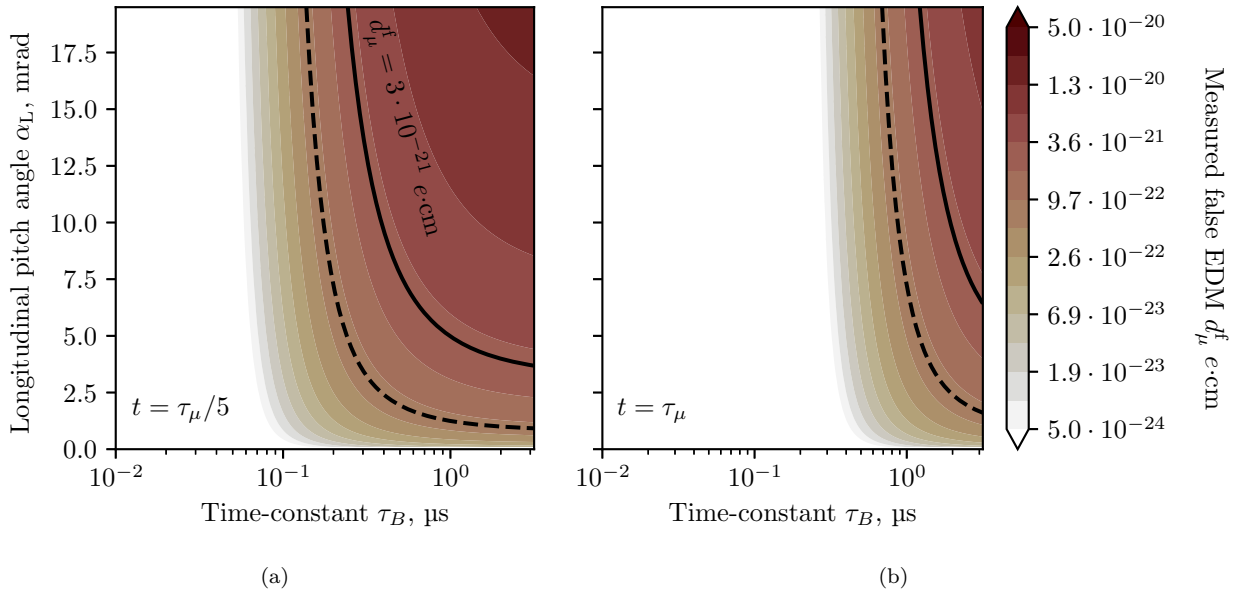
Figure 5: Measured false EDM due to an exponentially decaying residual radial magnetic field.
(a) Systematic effect at time $t = 450\,\mathrm{ns}$ and (b) at time $t = 2197\,\mathrm{ns}$, after one muon lifetime. The black line represents the target sensitivity level of $d_\mu = 3.0 \times 10^{-20}\,e\cdot\mathrm{cm}$ and the dashed line is one quarter of that value. The figures show a snapshot of the limit at two different moments in time.
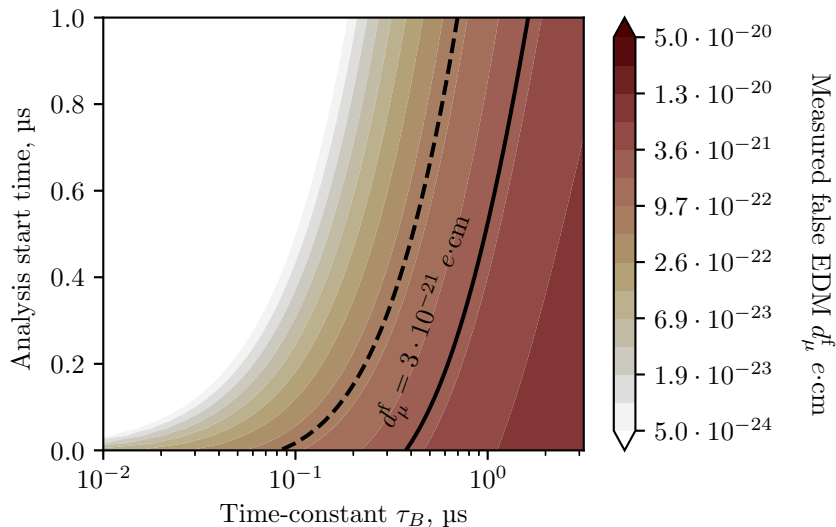


Figure 6: Phase accumulation due to exponentially decaying radial magnetic field from the analysis start time to infinity. The longitudinal pitch angle is 10 mrad.

to the measured EDM, the time constant $\tau_B$ of the pulse decay must be kept below 50 ns. The decay time constant of the kicker circuit currently under consideration (see section VII E) satisfies this constraint.

Integrating Eq. 33 from the start of the analysis time to infinity and weighing by the muon decay gives the total phase accumulated by the spin due to the residual tail from the magnetic kick. This is compared to the expected phase accumulation due to EDM with a given value and the results are shown in Fig. 6. The longitudinal pitch angle is fixed at 10 mrad, which is close to the expected one.

### 2. Azimuthal spin precession

When the muons circulate in the storage ring, they oscillate around an equilibrium orbit. Because of this oscillation, the momentum of the particle is not at all times perpendicular to the longitudinal magnetic field, leading to a non-zero projection of the magnetic field along its trajectory. This field is proportional to the angle between the muon momentum and the magnetic field $\delta = \angle(\vec{\beta}, \vec{B})$. In turn, $\cos\delta = p_y/p_z$ and $p_y$ oscillate as $p_y = p_{y_0}\sin\omega_\beta t$. Thus:

$$B_z(t) = B_y\cos\delta \approx \frac{p_{y_0}}{p_z}\sin\omega_\beta t B_y. \tag{34}$$

The momentum $p_{y_0}$ is the momentum in the $y$ direction when the muon is on the equilibrium orbit. It can be calculated as follows

$$p_{y_0} = ec\beta\Phi_0\rho y_0 \int_0^{\frac{\pi}{2\omega_\beta}} \cos\omega_\beta t\, dt = ec\beta\Phi_0\rho y_0 \frac{1}{\omega_\beta}. \tag{35}$$

In the ideal case $\vec{\beta} = |\beta|z$ and $\vec{E} = |E|x$, but as the muons oscillate in the weakly-focusing field, there will be a non-zero $y$ component of the velocity, thus:

$$\beta_y = (p_{y_0}/p_z)\,\beta_z\sin\omega_\beta t. \tag{36}$$

If the radial electric field $E_x$ is correctly set to the value $E_{\rm f}$ required by the frozen-spin technique, then there will be no oscillations around the $z$ axis, excluding the second-order $\beta \cdot \vec{B}$ term in (7). At this value for the electric field, it will counteract the precession induced by the coupling of the MDM to the longitudinal field of the solenoid. However, if $E_x \neq E_{\rm f}$ there will be imperfect cancellation of the $g-2$ precession around $z$ that is proportional to the excess electric field $\Delta E = E_x - E_{\rm f}$ to which the muon is subjected:

$$\left(\vec{\Omega}_{\rm MDM}^{\Delta E}\right)_z = -\frac{e}{m_0 c}\left(a - \frac{1}{\gamma^2 - 1}\right)\beta_y E_{\rm ex}. \tag{37}$$

Taking into account Eq. (34), the angular velocity of the spin precession along the $z$ axis due to the $\vec{\beta} \cdot \vec{B}$ term in the Thomas-BMT equation is:

$$\left(\vec{\Omega}_{\rm MDM}^{\beta\cdot B}\right)_z = \frac{ea}{m_0}\left(\frac{\gamma-1}{\gamma}\right)B_z(t). \tag{38}$$

Combining Eqs. (38) and (37) gives the total angular velocity of the precession due to the MDM around the $z$ axis:

$$\left(\vec{\Omega}_{\rm MDM}\right)_z = -\frac{e}{m_0}\frac{p_{y_0}}{p_z}\sin\omega_\beta t\left[\left(a - \frac{1}{\gamma^2-1}\right)\frac{\beta_z}{c}\Delta E - a\left(\frac{\gamma-1}{\gamma}\right)B_y\right]. \tag{39}$$

### 3. Electric field misalignment

The value of $E_x$ may not be constant throughout the orbit of the muon if the central axes of the magnetic and electric fields are displaced or inclined with respect to each other. To obtain the components of the electric field with respect to the central axis of the solenoid, first consider a purely radial electric field created by perfect coaxial cylindrical electrodes with radii $A$ and $B$. In the reference frame $(x', y', z')$ of the electrodes, where $z'$ is parallel to the central axis of the electrodes, the field is given by:

$$\vec{E}'(\vec{r}) = \frac{V}{\log\frac{B}{A}}\begin{pmatrix} x'/r^2 \\ y'/r^2 \\ 0 \end{pmatrix}, \tag{40}$$

where $r^2 = (x')^2 + (y')^2$. However, the central axis of the electrode may be displaced and rotated with respect to the reference frame defined by the central axis of the solenoid. The electric field $\vec{E}$ in the reference frame of the solenoid can be obtained by transforming $\vec{E}'$ as:

$$\vec{E} = R_y(\delta)\vec{E}'(R_y^{-1}(\delta)\vec{r} + \vec{r}_0), \tag{41}$$

where $\vec{r}_0 = (x'_0, y'_0, 0)$ is the displacement between the two fields. $R_y(\delta)$ is the rotation around the $y'$ axis at an angle $\delta$, where $\delta$ is the angle between the central axis of the cylindrical electrodes and the central axis of the longitudinal magnetic field. Note here that due to the rotational symmetry of the fields, we can always choose the reference frame so that arbitrary displacements can be represented in this way. The electric field in the reference frame defined by the longitudinal magnetic field is then:

$$\vec{E}(\vec{r}) = V_0 \begin{pmatrix} \frac{\xi}{\rho^2} \cos\delta \\ \frac{\upsilon}{\rho^2} \\ -\frac{\xi}{\rho^2} \sin\delta \end{pmatrix} \tag{42}$$

where $V_0 = V / \log(B/A)$, $\upsilon = y' + y'_0$, $\xi = x'_0 + x' \cos\delta - z' \sin\delta$ and $\rho^2 = \xi^2 + \upsilon^2$.

The average of the radial electric field over the circular orbit of the muon can be obtained if $E'$ is represented in cylindrical coordinates $(\rho, \phi, \zeta)$ as:

$$E_\rho = \langle E(\rho, \zeta) \rangle_\phi = \frac{1}{2\pi} \int_0^{2\pi} E(\rho, \phi, \zeta) d\phi, \tag{43}$$

where $\rho$ is the radius of the orbit of the muon as a function of the magnetic field and the momentum of the particle, and $\zeta$ is parallel to $y$.

The radial electric field the muon experiences in its reference frame is approximated as:

$$E_x = E_\rho + \frac{1}{2}\left(E_{\rho,\max} - E_{\rho,\min}\right)\cos(\omega_c t + b_0), \tag{44}$$

where $\omega_c = -eB_y/\gamma m_0$ is the cyclotron angular velocity, $E_{\max}$ and $E_{\min}$ are the maximal and minimal values of the electric field in one muon orbit and $b_0$ is the initial phase of the muon position along the orbit.

Note that Eq. (43) is valid only in the case of a circular orbit. In this case, it can be shown numerically that:

$$\langle E(\rho, \zeta) \rangle = \langle E'(\rho, \zeta) \rangle, \tag{45}$$

which means that the rotation of the anode or cathode with respect to the muon orbit does not influence the average frozen-spin condition and, more importantly, does not change the net E-field component in the $y$ direction. As the centripetal force due to the B-field is $\approx 10^3$ higher than that due to the E-field and the expected misalignments between the center of the orbit and the center of the inner electrode are small, the circular orbit approximation holds well.

Equations (42) and (45) are valid under the assumption of an infinitely long coaxial structure. For this to be a valid assumption, the electrode structure must be long enough that fringe fields do not penetrate to the central part where the muon orbit lies. There are two other major effects that could generate a net $E_y$ field that would not be averaged out in a circular orbit:

- Non-uniformity of the radius of the cylindrical structure of the anode or cathode.

- Imbalance in the charge distribution of the cathode or anode with respect to the plane of the average orbit.

- Fringe fields due to the finite coaxial structure length penetrating to the region of interest.

Simulations, using finite element methods (see Figure 7), show that with a 500 mm long anode and a separation of 20 mm between anode and cathode there is an about 300 mm wide region with a negligible longitudinal electric field, less than 0.1 ppm. This indicates that electrodes as short as 250 mm could be used to provide the purely radial electric field needed for the frozen-spin technique.

To set a limit for the radial nonuniformity of the cylindrical electrodes we assume the simple case where the radius of the anode varies linearly from $R$ to $R + \Delta_R$ in a region of length $L$. For a small $\Delta_R$ the electric field in the $y$ direction is:

$$E_y \approx E_f \frac{\Delta_R}{L} \approx E_f \alpha_R, \tag{46}$$

where $\alpha_R = \Delta_R/L$. To achieve the $E_y/E_f \leq 3 \times 10^{-4}$ limit of Phase I, see Figure 4a, the angle $\alpha_R$ must be less than 300 μrad. In the case of Phase II $\alpha_R \leq 7$ μrad. The maximum permitted linear change of the anode radius, $\Delta_R$, is 40 μm and 7 μm respectively, for an anode of length $L = 100$ mm.
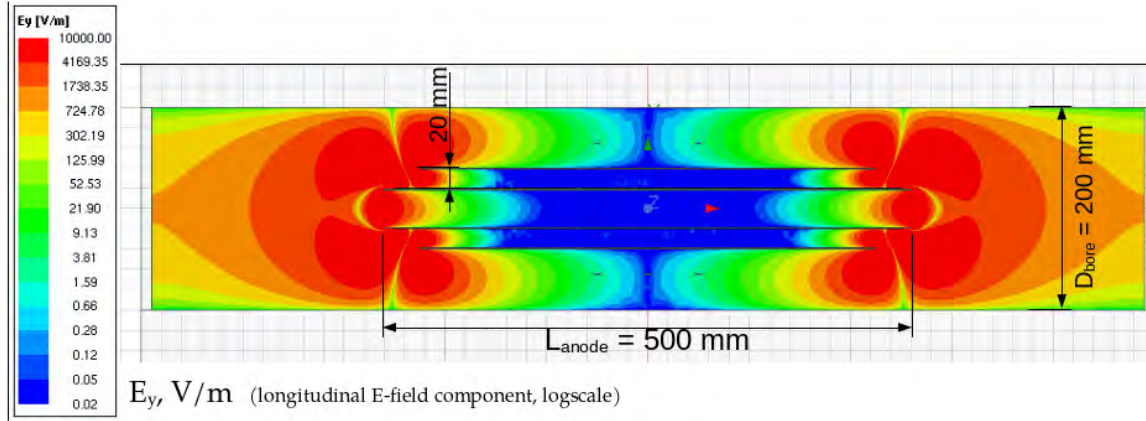
Figure 7: Longitudinal E-field component for a 500 mm long coaxial electrode structure simulated using ANSYS finite element simulations. The color scale is logarithmic and the values are in units V/m. The radial component $E_\mathrm{f}$ is 270 kV/m. The potential difference between the anode and cathode is 6.2 kV.

### 4. Longitudinal spin precession

The initial orientation of the spin $\vec{S} = (S_x, S_y, S_z)$ in spherical coordinates is:

$$\phi_0 = \arctan\left(\frac{S_x}{S_z}\right), \quad \Theta_0 = \arctan\left(\frac{\sqrt{S_x^2 + S_z^2}}{S_y}\right) - \frac{\pi}{2}. \tag{47}$$

If there is an imperfect cancellation of the $g - 2$ precession, then there will be a rotation of the spin around the longitudinal $y$ axis. Thus, the angular velocity of the spin precession around $x$ and $z$ will be a projection of (39) and (29) along $y$:

$$|\vec{\Omega}_\mathrm{MDM} \cdot y| = \left(\vec{\Omega}_\mathrm{MDM}\right)_x \cos(\omega_y t + \phi_0) + \left(\vec{\Omega}_\mathrm{MDM}\right)_z \sin(\omega_y t + \phi_0), \tag{48}$$

where $\omega_y$ is the angular velocity of the precession around $y$ due to the $g - 2$ precession and is:

$$\omega_y = \frac{ea}{m_0} \frac{E_\mathrm{ex}}{E_\mathrm{f}} B_y. \tag{49}$$

In practice, $E_\mathrm{ex}$ will oscillate, see Eq. (44), with the cyclotron frequency due to the changing distance between the muon and the E-field center. The longitudinal B-field $B_y$ will oscillate with the VBO frequency due to the changing longitudinal component of the weakly focusing field, proportional to Eq. (22)). In a well-tuned frozen-spin experiment, $\omega_y$ is much smaller than $\omega_\beta$ and $\omega_\mathrm{c}$, and the rotation of the spin around $y$ can be approximated with constant angular velocity using the average values of $E_\mathrm{ex}$ and $B_y$. The total longitudinal rotation of the spin $\Theta$ is:

$$\Theta(t) = \int_0^t |\Omega_\mathrm{MDM} \cdot y| dt \tag{50}$$

### 5. Comparison with Geant4 spin tracking

To verify the analytical equations, a model of the experiment was developed using the GEANT4 Monte Carlo simulation toolkit [58]. The EM fields of the experiment can be either calculated analytically or interpolated from field maps. The field maps are generated by ANSYS Maxwell FEM software. The simulation has three major EM field components:

1. The main solenoid magnetic field – constant value along $y$ or field map supplied by FEM simulations.

2. Radial electric field given by Eq. (42) with the option to add a constant or uniform component in the longitudinal direction or FEM simulated field map.

3. Weakly-focusing field modeled in ANSYS as a single circular coil with $R = 65$ mm.

Muons start with zero momentum in the $y$ direction, since this is the initial condition for a stored muon. The simulation tracks the spin orientation in the reference frame of the muon and records it as a function of time. It can also track the direction with respect to a reference frame defined by the experimental setup, e.g., the solenoid.

A comparison between the analytical equations derived and the GEANT4 spin tracking is shown in Fig. 8. In the comparison a fine field map (0.2 mm step size) of the weakly focused field was used. All other EM fields are calculated analytically. The stepper used is the DormandPrinceRK78 routine [58] with 0.26 mm step size. The stepping size was chosen so as to avoid effects due to resonances between the stepper and field map grids. The initial coordinates of the muon at the moment of storage were arbitrarily chosen (values specified in Figure 8 caption) for the purpose of the illustration. The electric field was set to such a value as to have imperfect cancellation of the $(g-2)$ precession. The anode coaxial E-field is tilted with respect to the longitudinal axis by $\delta = 0.01°$ in order to highlight the cyclotron oscillations.

The comparison shows very good agreement between the analytical equations and the GEANT4 spin tracking. The approximate equation for the description of the weakly-focusing field, Eq. (23), provides good estimates of the field strength and the VBO frequency. The difference between analytical and numerical approaches is less than 5 µrad sustained over 12 µs of simulation time, demonstrating the good agreement between the two also when using realistic field maps generated by FEM in Geant4.
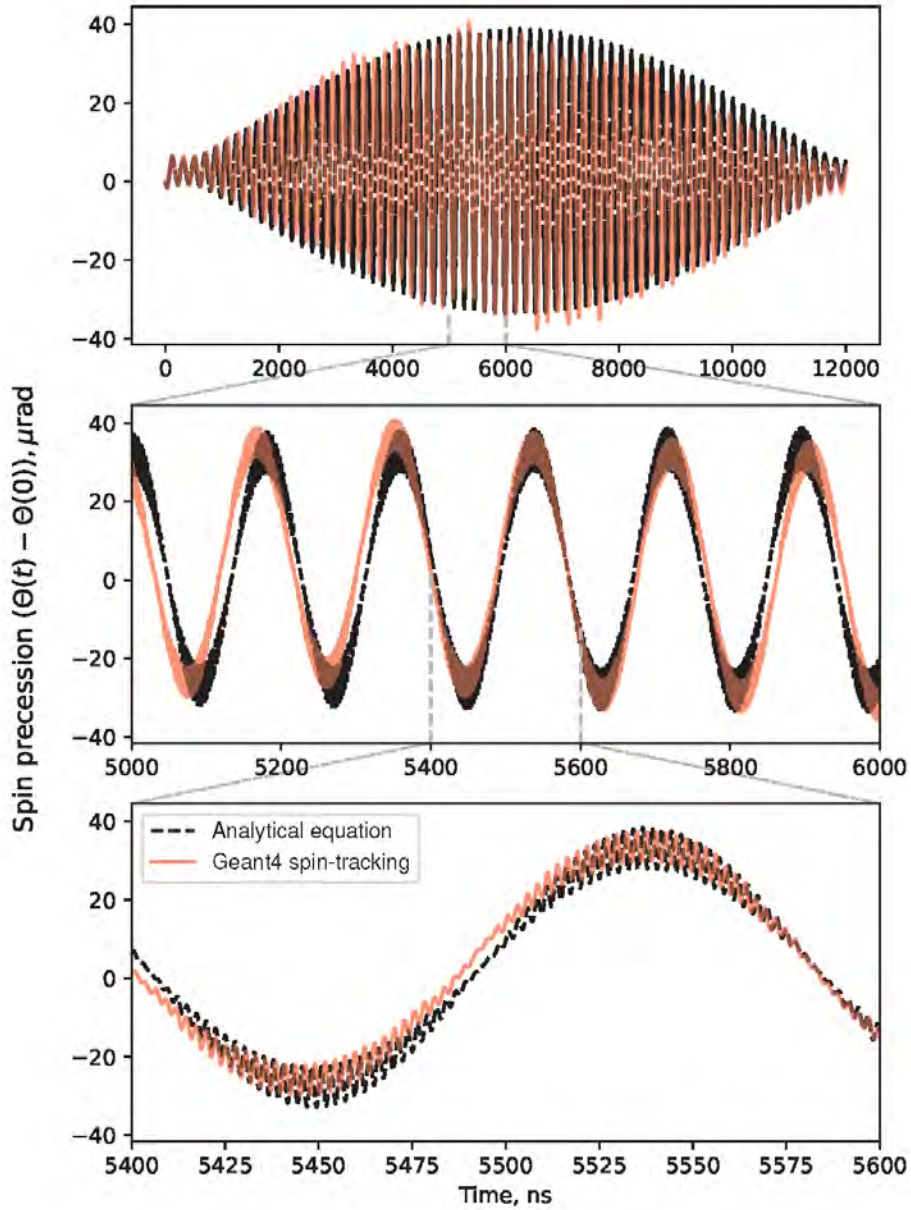
Figure 8: Comparison between the analytical Eqs. (50) and the GEANT4 spin tracking simulation. The initial parameters are arbitrarily set to $\vec{S}_0 = (-0.89, 0.00, -0.46)$, $\vec{p}_0 = (0.84, 0.00, 0.55) \times 26.8\,\text{MeV}/c$ and $\vec{r}_0 = (-16.95, 5.00, 22.10)\,\text{mm}$. The ideal momentum for which the electric field is set to the frozen-spin condition is $p_0^{\text{ideal}} = 28.0\,\text{MeV}/c$. The three plots show different timescales of the spin motion – uncompensated $(g-2)$ precession, betatron oscillations, and cyclotron oscillations.

## B.  Spin precession due to geometric phases

The geometric phase, also known as Berry's phase, is a phase difference acquired over the course of a cycle in parameter space when the system evolves adiabatically [59]. Such cycles in the parameter space can occur due to the periodic oscillations of stored muons in the non-uniform electric and magnetic fields of the experiment. In classical parallel transport, the phase accumulation is equal to the solid angle subtended by the path of the particle on the unit sphere in magnetic-field space. For quantum parallel transport in fermions, the geometric phase is half of that [60].

Let us assume that there are two oscillations around the perpendicular axes $x$ and $y$ in the form:

$$\theta_x(t) = \frac{1}{\omega_x}\Omega_x \sin(\omega_x t), \text{ and } \theta_y(t) = \frac{1}{\omega_y}\Omega_y \sin(\omega_y t + \beta_0), \tag{51}$$

where $\omega_x$ and $\omega_y$ are the angular frequencies of the oscillations, $\Omega_x$ and $\Omega_y$ are the peak angular velocities of the spin precession around the respective axis, and $\beta_0$ is the difference in their phases. The maximum angular velocity of the spin precession is equal to $ea/m_0 B$ for B-fields and to $ea/(m_0 c)((\gamma^2-1)^{-1} - a)\vec{\beta}\times\vec{E}$ for E-fields. In the case of small oscillations, the surface of the unit sphere can be approximated with a plane and the enclosed solid angle can be approximated with the area enclosed by the curves. The area under parametric curves can be calculated using Green's theorem:

$$\alpha(t) = \frac{1}{2}\int(\theta_x\theta_y' - \theta_y\theta_x')dt \tag{52}$$

Calculating the integral in the case where $\omega_x \neq \omega_y$ one obtains:

$$\alpha(t;\omega_x,\omega_y,\beta_0) = \frac{1}{2}\frac{\Omega_x\Omega_y}{\omega_x\omega_y}\int(\omega_y\cos(\omega_y t + \beta_0)\sin(\omega_x t) - \omega_x\cos(\omega_x t)\sin(\omega_y t + \beta_0))\,dt =$$

$$= \frac{1}{4}\frac{\Omega_x\Omega_y}{\omega_x\omega_y}\left[\frac{\omega_x-\omega_y}{\omega_x+\omega_y}\cos((\omega_x+\omega_y)t+\beta_0) - \frac{\omega_x+\omega_y}{\omega_x-\omega_y}\cos((\omega_y-\omega_x)t+\beta_0)\right]. \tag{53}$$

In the case of resonant oscillations (having the same angular frequency $\omega = \omega_x = \omega_y$) the solution is:

$$\alpha(t;\omega,\beta_0) = \frac{1}{2}\frac{\Omega_x\Omega_y}{\omega^2}\int(\omega\cos(\omega t + \beta_0)\sin(\omega t) - \omega\cos(\omega t)\sin(\omega t + \beta_0))\,dt = -\frac{1}{2\omega}\Omega_x\Omega_y t\sin(\beta_0). \tag{54}$$

These equations allow one to calculate the phase accumulation as a function of time in the case of two periodic oscillations along the perpendicular axes. It can be seen that the geometric phase becomes larger with decreasing differences between the frequencies of the two oscillations. In the case of equal frequencies the phase accumulation is linear with time and is proportional to the product of the peak angular velocities of the spin precession around the two axes. The geometric phase is zero when the two oscillations are in phase ($\beta_0 = 0$) and is maximal when they are out of phase ($\beta_0 = \pi/2$).

*a. Resonant oscillations*

Two periodic oscillations along the perpendicular axes with equal angular frequencies can occur due to the cyclotron motion of muons inside the E-field used for the frozen-spin technique. Consider the case described in Eq. (41), where there is an angle between the central axes of the coaxial electrode system and the longitudinal magnetic field, and the center of the muon orbit is displaced by $\vec{r}_0$ with respect to the electric field center. Equation (45) shows that in this case the net $(g-2)$ precession over a turn would be zero. The net precession due to the longitudinal E-field component that is seen in the muon reference frame would also be zero. Nevertheless, the spin will cause small oscillations around the longitudinal and radial axes with the cyclotron angular frequency $\omega_c$. A geometric phase will be observed if the displacement of the orbit $\vec{r}_0$ is such that both oscillations are out of phase.

To calculate the resulting geometric phase accumulation, we use (54), where $\omega = \omega_c$. $\Omega_x$ and $\Omega_y$ are the maximum spin precession angular velocity due to the oscillations in the longitudinal and radial E-field components. Using the Thomas-BMT equation and Eq. (42) they can be approximated as:

$$\Omega_x = -\frac{ea}{m_0 c}\beta_z\frac{\max(\Delta E) - \min(\Delta E)}{2} \text{ and } \Omega_y = -\frac{ea}{m_0 c}\left(1 - \frac{1}{a(\gamma^2-1)}\right)\beta_z\frac{\max(E_y) - \min(E_y)}{2}. \tag{55}$$

To verify (54) and (55) the GEANT4 simulation of the experiment was set with exaggerated parameters to highlight the phase accumulation effect. The coaxial electrodes are tilted at 15 mrad and the center of the muon orbit is displaced by 5 mm. The radial E-field is lower than required for the frozen-spin condition to allow for a residual $(g-2)$ precession. The phase between the two oscillations is set to the worst-case scenario $\pi/2$. The comparison between the equations and the spin tracking simulation is shown in Fig. 9a. For the purpose of the comparison, we assume classical parallel transport, since the simulation software is not capable of simulating quantum behavior. The phase accumulation in reality will be half of the value obtained.
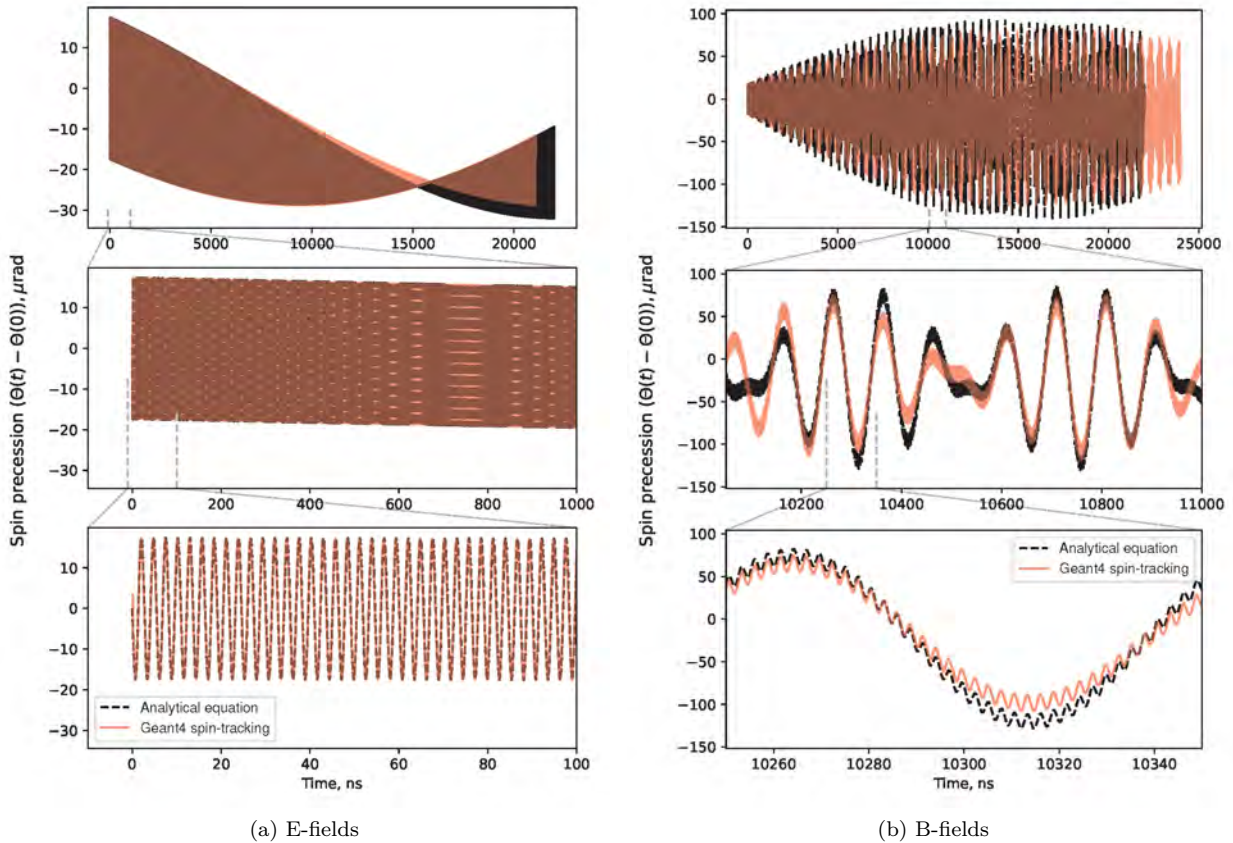
(a) E-fields

(b) B-fields

Figure 9: Accumulation of Berry's phase due to oscillations of the spin around perpendicular axes. Figure (a) shows the case of equal oscillation frequencies around the two axes. Figure (b) shows the Berry phase for the superposition of oscillations with different frequencies.

### b. Off-resonance oscillations

In order to validate Eq. (53) the same simulation conditions as the previous comparison were used, but with an additional oscillating radial B-field. In reality such radial oscillations can be induced by a residual B-field from the magnetic kick. The B-field in the comparison consists of two sine waves with different amplitudes and initial phases and angular velocities at ±5% of the cyclotron angular velocity (2.3 rad/ns). The results of the comparison are presented in Fig. 9b. A very good agreement between the theoretical prediction and spin tracking is observed on the scale of microseconds ($g-2$ precession) and nanoseconds (cyclotron oscillations). The overall behavior of the geometrical phase is captured by the analytical equations, but there are small differences in the predicted and observed beating patterns. These could be due to the quantization of the B-field oscillations and particle motion in the simulation, which introduces additional high-frequency noise.

### 1. Limits due to geometrical phases

Here we will consider possible sources of geometrical phase accumulation in the experiment and compare them to the limits on the EDM-induced spin precession angular velocity (equations (20) and (21)).

### a. Resonance between radial and longitudinal E-fields

Assuming a 1 mrad angle and 2 mm displacement between the central axes of the coaxial electrodes and the average muon orbit, the geometrical phase accumulation will be 0.12 rad/s, or 0.6% of the spin precession due to an EDM equal to the statistical sensitivity of the precursor experiment. For the final experiment, this amounts to 0.04 rad/s or 3.0% of the expected signal. The effect is reduced in the final experimental conditions because we will use higher-momentum muons, which will have a larger radius of gyration and thus will experience a more uniform radial E-field from the coaxial electrodes.

*b.  Longitudinal and radial betatron oscillations*
The muons will undergo longitudinal betatron oscillations according to Eq. (25). As a result, the spin will oscillate around the radial axis with angular frequency $\omega_\beta$. As $\nabla \cdot B = 0$ the spin will also oscillate around the longitudinal axis (radial betatron oscillations). These two oscillations have exactly the same frequencies and phases. The result derived in (54) shows that there will be no accumulation of geometric phase in this case because $\beta_0 = 0$. To confirm this behavior, we have performed GEANT4 simulations with varying strengths of the weakly-focusing field and for all cases no phase accumulation was observed.

*c.  Beating from cyclotron and betatron oscillations*
In order to avoid the accumulation of Berry's phase due to the coupling of betatron and cyclotron oscillations, they must have sufficiently different periods. The period of the beating pattern will be $T = 2\pi/(\omega_c - \omega_\beta)$, see Eq. (53). The cyclotron frequency will be of the order of 2.5 rad/ns and the betatron frequency of the order of 0.01 rad/ns, leading to a beating period of about 2.6 rad/ns. Compared to the few microseconds of measurement time, this effect does not present an issue.

*d.  General calculations of geometrical phases*  The outlined method for the calculation of geometrical phases can be generalized to arbitrary motions of the spin due to E-fields and B-fields. The complex motion can be analyzed in terms of its Fourier decomposition. This can be done by mapping the fields in the region of the storage ring as well as the trajectory of the muons. Then we will calculate the Fourier transform on the fields to which the particle is subjected along the three axes of rotation. The field mapping will be done with a sufficient spatial resolution to ensure that frequencies on the order of the cyclotron frequency are well described. The obtained amplitudes will then be used with Eq. (53) to calculate the geometric phase of the pair of frequencies as a function of time. Summing over all frequency pairs gives the total geometric phase.

## C.  Sources of apparent spin precession

If the muon spin has a component in the longitudinal direction, then the probability for up $p_\mathrm{u}$ and down $p_\mathrm{d}$ ejected decay positrons will differ and an asymmetry $A$ will be observed:

$$A(t) = \frac{p_\mathrm{u} - p_\mathrm{d}}{p_\mathrm{u} + p_\mathrm{d}} = \sin\Theta(t)\alpha P \approx \Theta(t)\,\alpha P, \tag{56}$$

where $\alpha$ is the parity-violating decay asymmetry averaged over the positron energy and $P$ is the initial polarization. Equation (56) is valid when $\Theta(t) \ll 1$, which is the case of EDM-induced spin precession.

Using Eqs. (17) and (56), the rate of change of asymmetry $\dot{A}$ is:

$$\dot{A} = \frac{\eta}{2}\frac{e}{m_0}\beta_z B_y \alpha P. \tag{57}$$

We require that the measured asymmetry $\dot{A}_\mathrm{m}$ due to spurious EDM mimicking effects is $\dot{A}_\mathrm{m} \ll \dot{A}$. The number of detected positrons in the upstream detector half $N_\mathrm{u}$ is given by:

$$N_\mathrm{u} = \Omega_\mathrm{u}\varepsilon_\mathrm{u}p_\mathrm{u}D, \tag{58}$$

where $D$ is the total number of decayed muons, $\varepsilon_\mathrm{u}$ is the detection efficiency for positrons averaged over their energy spectrum and $\Omega_\mathrm{u}$ is the solid angle coverage of the upstream detector. Both $\Omega_\mathrm{u}$ and $\varepsilon_\mathrm{u}$, can be summarized with a single parameter $\kappa_\mathrm{u} = \Omega_\mathrm{u}\varepsilon_\mathrm{u}$ expressing the effective detection efficiency of the upstream detector. A similar equation can be given for the downstream detector half and so:

$$N_u = \kappa_\mathrm{u}p_\mathrm{u}D \text{ and } N_\mathrm{d} = \kappa_\mathrm{d}p_\mathrm{d}D. \tag{59}$$

From the point of view of the experiment, substituting Eq. (59) into Eq. (56), the measured asymmetry $A_\mathrm{m}$ is given by:

$$A_\mathrm{m} = \frac{1}{D}\left(\frac{N_\mathrm{u}}{\kappa_\mathrm{u}} - \frac{N_\mathrm{d}}{\kappa_\mathrm{d}}\right). \tag{60}$$

If the effective detection efficiencies $\kappa$ are constant in time, no systematic effect appears, but any time dependence, e.g., by a disturbance of the detector electronics through the pulsed kicker field, leads to a systematic bias. A worst-case scenario assumption is that the kicker field disturbs the detection efficiency
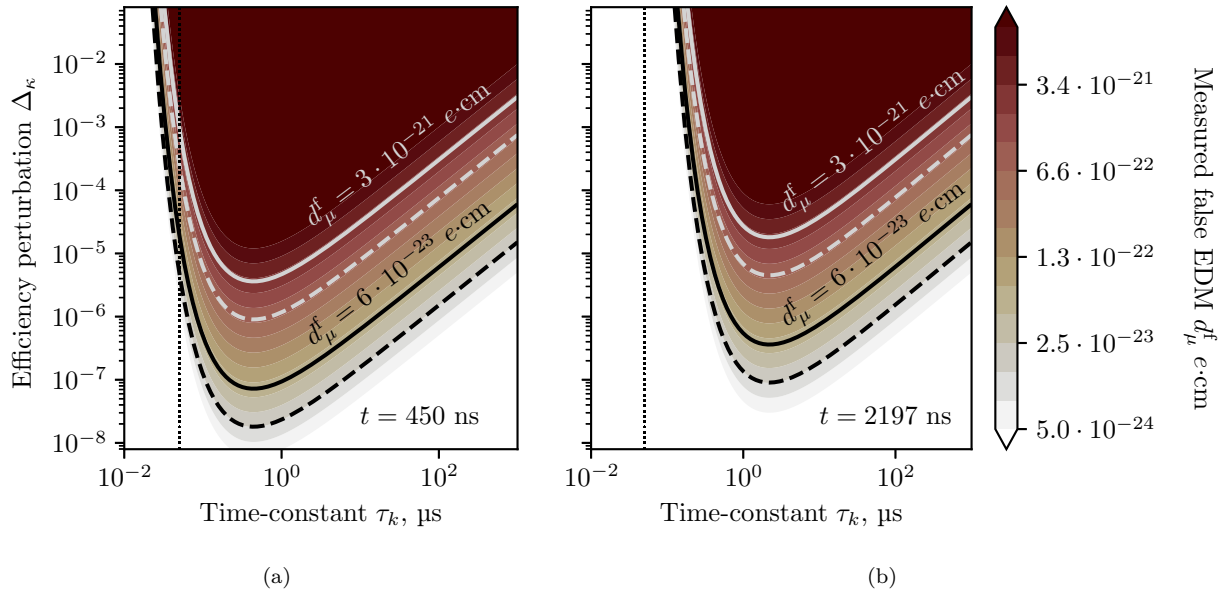
Figure 10: The measured false EDM due to an exponentially decaying, time-varying detection efficiency, for (a) $t = 450\,\text{ns}$ and (b) $t = 2197\,\text{ns}$, one muon lifetime. The solid lines represent the target sensitivity level of the precursor and final experiments and the dashed lines are one quarter of that value. The vertical dashed line at $\tau_\kappa = 0.05\,\text{µs}$ indicates the expected decay time of the magnetic kick.

in both the upstream and downstream part of the detector in opposite directions and its effect reduces exponentially with time. The disturbance can be modeled as:

$$\kappa_{\text{u}} = \kappa_{u0} - \Delta_\kappa e^{-t/\tau_k} \text{ and } \kappa_{\text{d}} = \kappa_{d0} + \Delta_\kappa e^{-t/\tau_k}, \tag{61}$$

where $\kappa_{u0}$ and $\kappa_{d0}$ are some equilibrium detection efficiencies, $\Delta_\kappa$ is the perturbation in the efficiency due to the kicker field and $\tau_k$ is the decay-time constant.

To quantify the false EDM signal that can be caused by time-dependent efficiency parameters, let us assume that there is no true EDM signal and that the upstream and downstream emission probabilities are equal $p_{\text{u}} = p_{\text{d}}$ leading to $D_{\text{u}} = D_{\text{d}} = D/2$. Then the observed asymmetry is:

$$A_{\text{m}} = \kappa_{\text{u}} - \kappa_{\text{d}} = \kappa_{u0} - \Delta_\kappa e^{-t/\tau_k} - \kappa_{d0} - \Delta_\kappa e^{-t/\tau_k}. \tag{62}$$

The measured EDM signal is given by the time derivative of the asymmetry; thus:

$$\dot{A}_{\text{m}} = \frac{2}{\tau_k} \Delta_\kappa e^{-t/\tau_k}. \tag{63}$$

From Eq. (63) we can observe that the systematic effect decreases exponentially with time $t$. The effect is exacerbated if $\tau_k$ is on the order of magnitude of the experimental measurement time $t$ which is several muon lifetimes. Bounds on $\tau_k$ and $\Delta_\kappa$ can be derived by requesting that the measured false asymmetry $\dot{A}_{\text{m}}$ be lower than the theoretical prediction $\dot{A}$ from Eq. (57) for a given $\eta$.

### D. Summary of systematic effects

In summary, we have derived analytical equations that describe the precession due to MDM in the EM fields of the experiment and validated these, using GEANT4 Monte Carlo simulations using realistic field maps. Very good agreement has been observed, and the analytical equations describe the spin motion well at short, medium, and long timescales. The most significant systematic effects in this category are due to non-zero average azimuthal and radial B-fields and a longitudinal E-field component. The latter can be largely canceled with alternating CW/CCW injection of muons into the experiment.

We have a preliminary understanding of the geometrical phases that can be accumulated due to oscillations

| Systematic effect | Constraints | Phase I | | Phase II | |
|---|---|---|---|---|---|
| | | Expected value | Syst. (×10⁻²¹ e·cm) | Expected value | Syst. (×10⁻²³ e·cm) |
| Cone shaped electrodes (longitudinal E-field) | Up-down asymmetry in the electrode shape | $\Delta_R < 30$ µm | 0.75 | $\Delta_R < 7$ µm | 1.5 |
| Electrode local smoothness (longitudinal E-field) | Local longitudinal electrode smoothness | $\delta_R < 3$ µm | 0.75 | $\delta_R < 0.7$ µm | 1.5 |
| Residual B-field from kick | Decay time of kicker field | $< 50$ ns | $< 10^{-2}$ | $< 50$ ns | 0.5 |
| Net current flowing muon orbit area | Wiring of electronics inside the orbit | $< 10$ mA | $< 10^{-2}$ | $< 10$ mA | 0.3 |
| Early-to-late detection efficiency change | Shielding and cooling of detectors | – | | – | |
| Resonant geometrical phase accumulation | Misalignment of central axes | Pitch $< 1$ mrad Offset $< 2$ mm | $2 \times 10^{-2}$ | Pitch $< 1$ mrad Offset $< 2$ mm | 0.15 |
| TOTAL | | | 1.1 | | 2.2 |

Table II: Summary of systematic effects for both phases of the experiment. The determination of the effects related to early-to-late detection efficiency changes will be completed before the end of 2023.

of the spin in a non-uniform EM field. The analysis shows that the only significant sources of systematic effects are due to resonances between oscillations around two perpendicular axes and only if the relative phase between the two is different from zero. One such effect comes from the cyclotron motion within the electric field, if the field is tilted and displaced relative to the central axis of the muon orbit. Geometrical phase accumulation due to oscillations with very different periods, e.g., cyclotron and betatron oscillations, has a negligible influence.

Another class of systematic effects that are addressed, result from early-to-late changes in the EDM detector system such as gain, acceptance, and noise thresholds. These are summarized as detection efficiency, and the false EDM signal that would be observed in a worst-case scenario is deduced.

A summary of all the significant systematic effects that are considered now is shown in Table II.

## E.   Next steps

The presented study on systematic effects in the experiment already provides bounds on several key design parameters. It also serves as a basis for further analysis on other possible effects.

In the coming year, we will focus on understanding better the impact of time-dependent electromagnetic fields on experiment accuracy and deduce the stability of the power converters needed to drive them. This will include the analysis of the dynamic and geometric phase accumulation. The goal is to set limits on the stability, using an Allan variance, and the noise of the driving electronics as a function of frequency.

We will also examine the impact of spatial non-uniformity of electromagnetic fields and derive limits on the acceptable variance of the magnetic field in the mid-plane and at the injection point for changes from CW to CCW injection.

These studies will be extended to a non-monochromatic momentum distribution and the derived systematic effects will translate into a maximum permissible momentum spread.

We will continue our analysis of systematic effects due to changes in detector acceptance and efficiency. That will include studies on effects related to thermal stability of the electronics, robustness of thresholds and energy cut-offs, accidental coincidences and others.
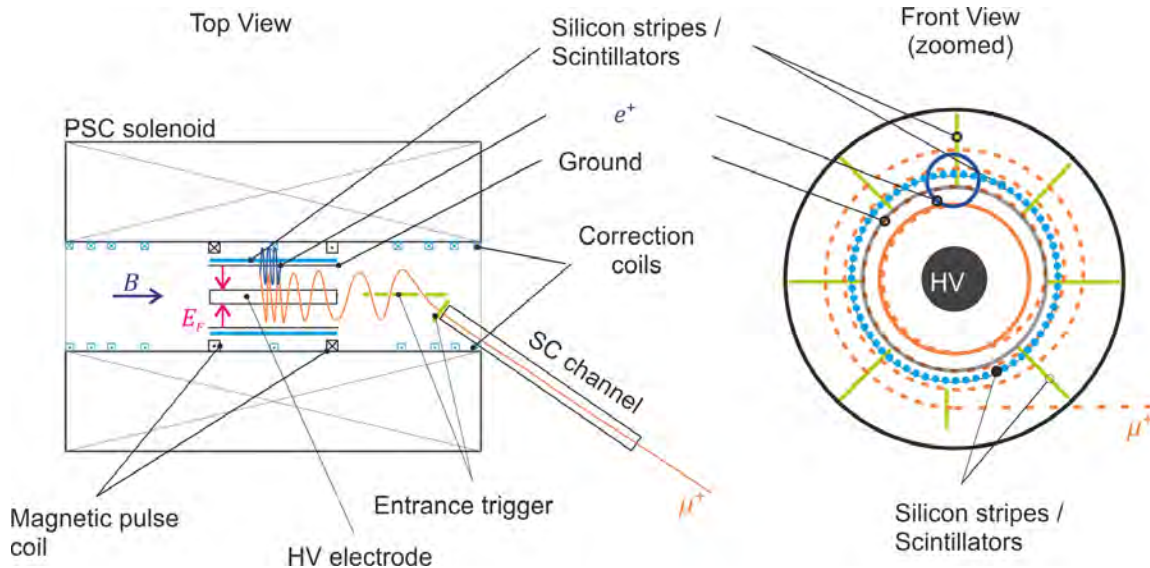
Figure 11: Overview of phase I experiment.

## VII. INSTRUMENT CONCEPT AND DESIGN

In the first phase, we will use an existing solenoid with a field of $3\,$T to demonstrate all the techniques necessary to perform a search for the muon EDM using the frozen-spin technique. A conceptional sketch is shown in Fig. 11.

Muons with momentum of $p \approx 28\,$MeV/c from pion decay at rest with a polarization better than $95\,\%$ will be injected into a collimation tube of ID$=15\,$mm and length $\ell \approx 800\,$mm inside a magnetic shield. While the collimation is the first step to select the incident phase space so as to match it to the tiny acceptance phase space, the magnetic shield (SC-channel) is essential to transport the muons from the low-field region at the exit of the beam to the high-field region inside the solenoid.

A set of correction coils inside the superconducting solenoid will reduce the field gradient between the injection region at the exit of the collimation tube and the storage region in the center of the solenoid to increase the acceptance phase space. A coil at the center of the solenoid will produce a weakly-focusing field required to store the muons for the measurement.

A thin entrance scintillator in anticoincidence with a set of active apertures, also made of scintillators, generates an entrance signal for muons within the acceptance phase space to trigger a magnetic pulse in the center of the solenoid. The $100\,$ns quadrupole magnetic pulse (pulse coil) turns the remaining longitudinal momentum, i.e. along the solenoid field, of the incident muon into the transverse direction.

The muon is stored on a stable orbit of radius $R = 31.4\,$mm within the weakly-focusing field. A radial electric field of $E_f = 3\,$kV/cm is applied in the storage orbit region between two coaxial electrodes to establish the frozen-spin condition. A combination of silicon strip and scintillating fiber ribbon track the decay positron to measure the $g-2$ frequency and longitudinal asymmetry.

The measurement of the $g-2$ frequency, $\omega_a$, will serve as a sensitive magnetic-field probe. Further, we will tune the E-field for the frozen-spin condition by measuring $\omega_a$ as a function of the applied electric field and interpolating to $\omega_a(E) = 0$.

### A. Muons from $\pi$E1

To demonstrate the frozen-spin technique, we plan to use $\pi$E1_2. For this purpose, we measured the muon-beam rate and characterized the transverse phase space of the muon beam with a momentum of $p = 28\,$MeV/c.

The $\pi$E1 beamline is a high-intensity pion and muon beamline with beam momenta ranging from $10\,$MeV/c to $500\,$MeV/c and a momentum resolution of better than $0.8\,\%$. The beam is extracted from target E in

| | Twiss parameters and emittance | |
|---|---|---|
| Horizontal phase space | $\alpha_x$ | -0.21 |
| | $\beta_x$ / m | 0.28 |
| | $\gamma_x$ / m$^{-1}$ | 3.69 |
| | $\epsilon_x$ / $\pi$ mm mrad | 198 |
| Vertical phase space | $\alpha_x$ | -0.21 |
| | $\beta_x$ / m | 0.28 |
| | $\gamma_x$ / m$^{-1}$ | 3.69 |
| | $\epsilon_x$ / $\pi$ mm mrad | 171 |

Table III: Twiss parameters of the $\pi$E1_2 beamline at 1444.25 mm downstream of the final quadrupole QSN56 and transverse beam emittance for the normal setting of the transfer line.

the forward direction at 8° with respect to the proton beam axis[4]. Figure 12 shows the layout of the beamline relative to target E. The beamline is used for both particle physics and $\mu$SR experiments. The magnet ASK51 is used to steer the beam to the experimental area $\pi$E1_2 (right side in Fig. 12) where the experiment of phase I will be mounted.

A Wien filter, also known as a separator, mounted between QSL54 and QSE51 will be used to select a muon beam with very low contamination from positrons or pions. The FS54 slit system is used to minimize the momentum bite further.

A scintillating fiber (SciFi) beam monitoring detector [61] mounted 1444.25 mm downstream of the quadrupole QSN56 (see Fig. 12), was used to measure the muon-beam rate and the transverse beam size. The transverse phase space was explored by employing a quadrupole-scan technique, which uses the quadratic relationship between the magnetic-field strength of the final focusing quadrupole in the beam line upstream of the beam monitoring detector and the transverse beam size to extract the phase-space parameters, namely Twiss parameters and emittance. Note that such a technique relies on independent knowledge of the dispersion function for each strength value of the quadrupole used for the scan in order to disentangle the betatronic from the dispersive part of the measured beam size.

The measurements were performed for a positive muon beam momentum at 28 MeV/c with two different beam tunes, the so-called "normal" beam tune and "inverted" beam tune. Both beam tunes were tested to maximize the muon beam intensity and minimize the transverse beam size at the beam focus. The "inverted" beam tune uses inverted currents for the last two quadrupole triplets of the $\pi$E1_2 beamline (QSN51 + QSN52 + QSN53 and QSN54 + QSN55 + QSN56) with respect to the "normal" beam tune. A full discussion of the measurements can be found in the thesis of M. Sakurai [62]. We will use the normal beam tune for our measurements as it provides higher flux and smaller vertical emittance.

We measured the transverse beam profiles simultaneously in $x$- and $y$-directions by integrating the count rate of each fiber over 10 s using the SciFi detector, see Fig. 13. The flux of $R = 4.5 \times 10^6 \, \mu^+$/s at a proton current of 1.6 mA was calculated by integrating over all fibers in each direction and taking the average.

Since the entire setup was placed in vacuum, the horizontal and vertical beam widths were determined directly by fitting a Gaussian to the time-averaged profiles and the $1-\sigma$ value of the distribution was used as true beam width. Figure 14 shows the extracted horizontal and vertical phase space ellipses. We obtain a horizontal emittance of $198 \, \pi$ mm $\cdot$ mrad $(1\sigma)$ and the vertical emittance of $171 \, \pi$ mm $\cdot$ mrad $(1\sigma)$. The Twiss parameters of this beam tune are summarized in Tab. III, and were used to generate an ensemble of Monte Carlo events, see Fig. 26 used as input for the simulation of the experiment. The polarization $P_0 > 0.95$ is known from other experiments and from $\mu$SR measurements at the beamline[5].

Figure 15 shows the last two quadrupoles of the muon delivery beamline, including a new dedicated dipole magnet to adjust the horizontal injection angle.

## B. Characterization of the muon trajectory

Having a well-known and reproducible muon trajectory plays a critical role in this experiment. First, achieving a high efficiency to trap muons at the center of the solenoid requires precise positioning of the

---
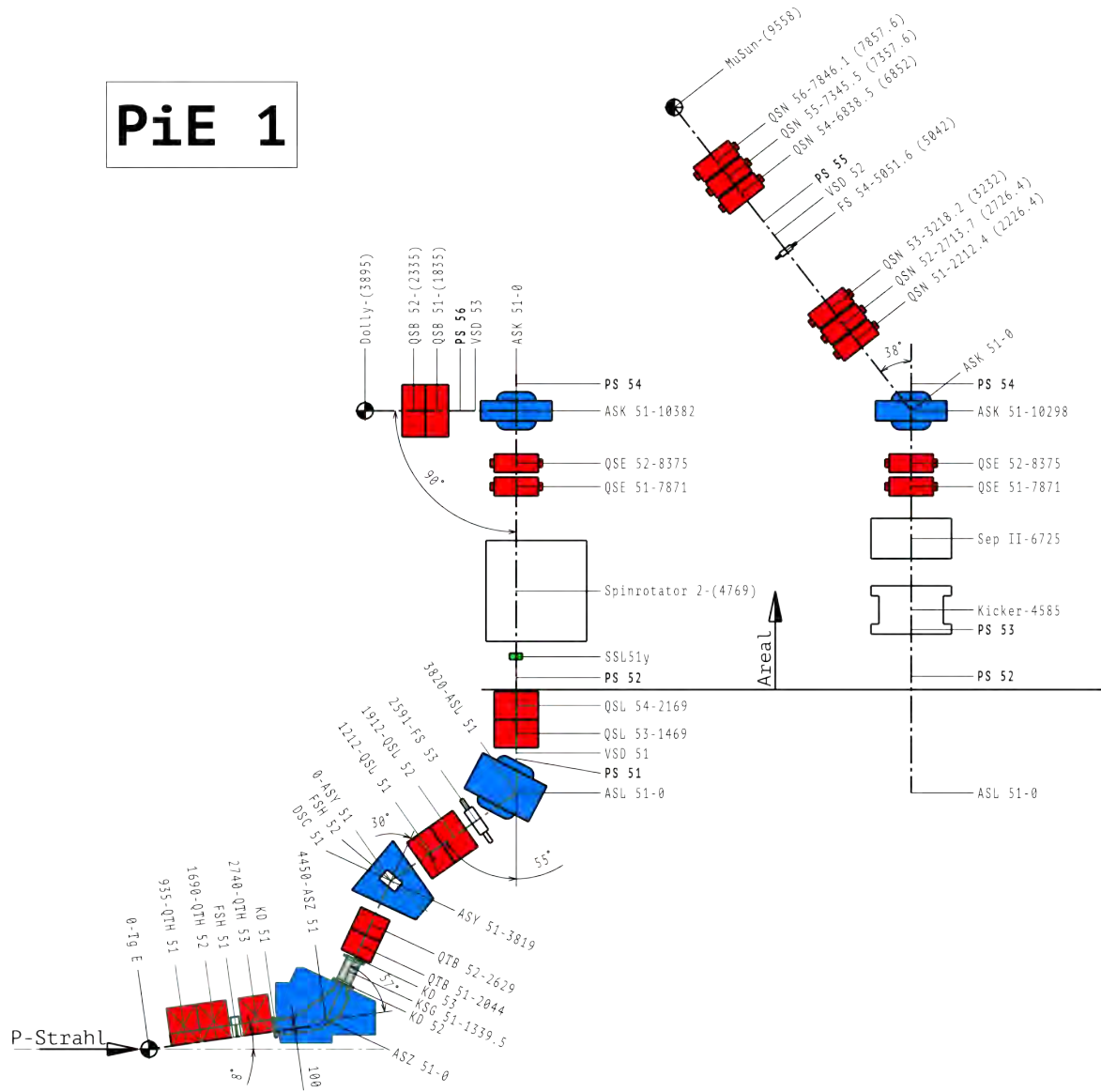
[4] https://www.psi.ch/en/sbl/pie1-beamline
[5] https://www.psi.ch/en/smus/dolly

Figure 12: Top view of the πE1 beamline. Two major beamline setups are shown. In both cases the beamline up to QSL54 are identical. The first three quadrupoles QTH51-53 and the dipole ASZ51 are used to extract the secondary beam from target E. The dipole ASY51 with the slit FSH51 defines the beam momentum and initial spread. The dipole ASL51 deviates the beam into the experimental zone. The quadrupoles QTB51/52 and QSL51-54 are set up as focusing-defocusing pairs and used for beam transport. The quadrupole pair QSE51/52 focuses the beam into the dipole ASK51, which is used to select one of the two following options. (Option 1) The setup on the left above the line indicating the concrete wall of the area is used for $\mu$SR measurements. (Option-2) The setup shown on the right is also known as πE1_2 and transports the beam to particle physics experiments mounted typically after the last quadrupole triplet QSN54-56. The separator and kicker downstream of QSL54 are optional. We have measured the transverse phase space 1444.25 mm downstream of the quadrupole QSN56 at position 9552 mm downstream of target E (πE1_2).

latter with respect to the beam. Moreover, the trigger system can work properly only if muons enter the solenoid along a trajectory as close as possible to the nominal one. Finally, cancellation of systematic uncertainties comparing the asymmetries measured with clockwise and anticlockwise injection requires a very small momentum difference in the two running modes, below 0.5%, as shown in Sec. VI.

These constraints call for the development of a set of detectors that should be able to track the muon trajectory just downstream of injection into the solenoid. A practical use of such detectors could be to
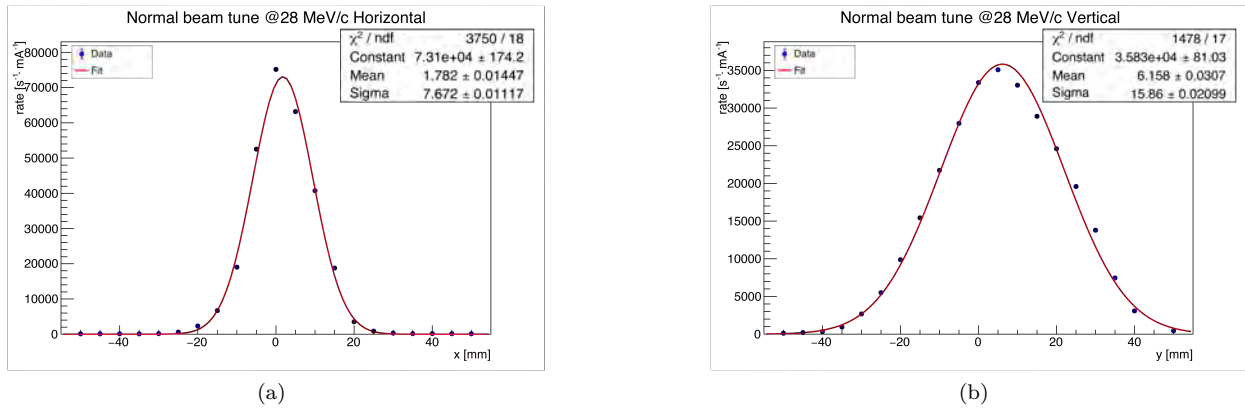
Figure 13: Measured horizontal (a) and vertical (b) muon beam distribution at 28 MeV/c for πE1_2
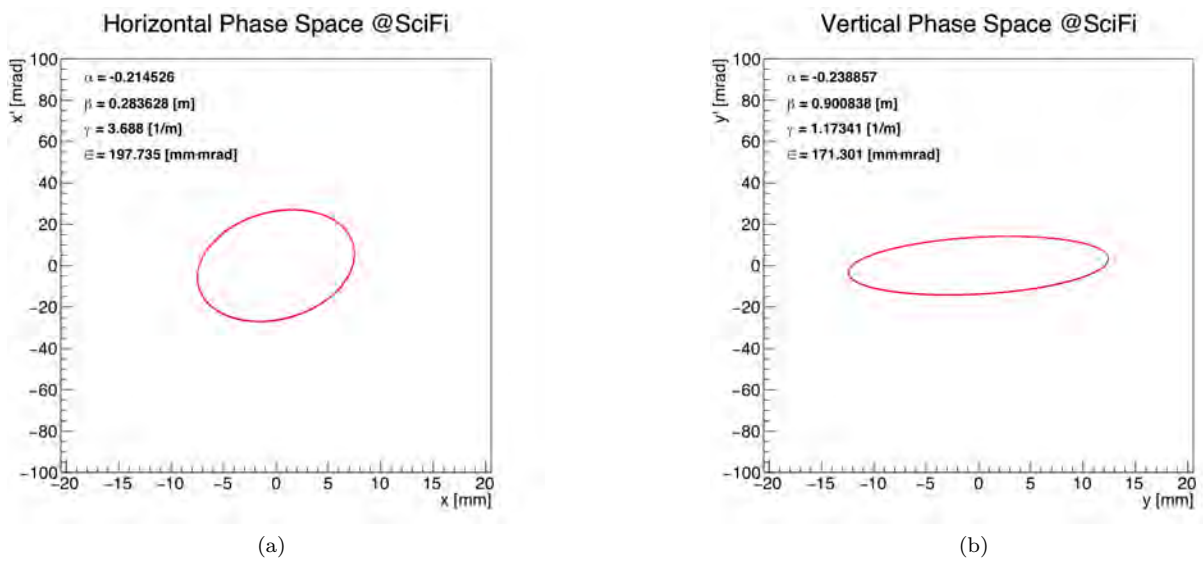


Figure 14: Measured horizontal (a) and vertical (b) phase space Twiss parameters for 28 MeV/c muons for πE1_2
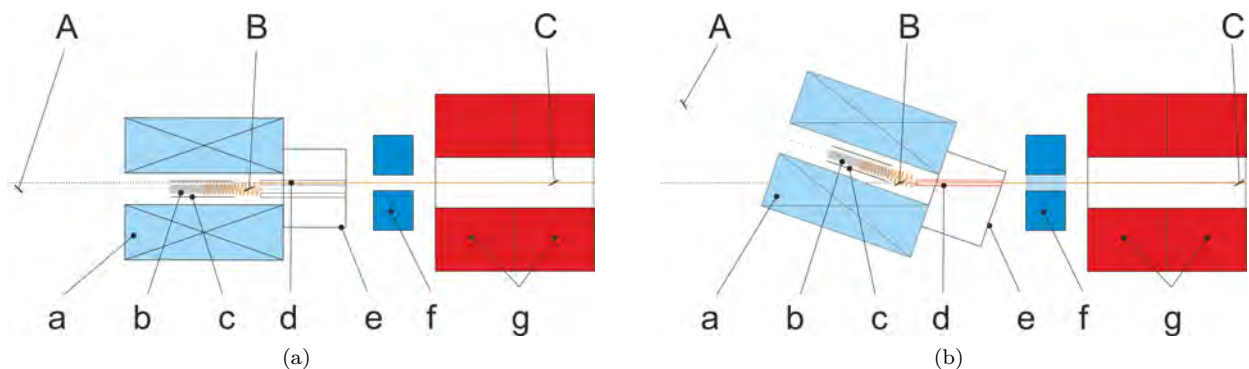


Figure 15: View of the last section of the injection beamline: side view (left) and top view (right) along the line A-B-C. From left to right: (a) SC solenoid, (b) inner high-voltage electrode, (c) outer ground electrode, (d) magnetically shielded injection channel, (e) vacuum tube, (f) horizontal dipole, (g) quadrupoles QSN55 and QSN56. (Orange) nominal muon trajectory, (blacked dashed) beam axis, (dark gray dotted) SC solenoid axis.

control the positioning of the solenoid with respect to the beam and to characterize the performance of the trigger system every time the experiment is moved to alternate clockwise and anticlockwise injection. More generally, a measurement of the beam trajectories and envelopes inside the solenoid will be essential to evaluate the related systematic uncertainties.

To meet the requirements of the experiment, the longitudinal injection angle, which is critical to trapping the muon, and the muon momentum should be measured with resolutions not much worse than a few mrad and 0.5%, respectively. Indeed, although the average trajectory could be measured much more precisely by averaging over many muons, these resolutions are needed for a good characterization of the envelope. For muons at 28 MeV/$c$, these measurements will be greatly affected by the interaction with the detector material (multiple Coulomb scattering and energy loss), and therefore extremely light detectors should be used, gaseous detectors being the most natural choice.

It is not necessary that these detectors are permanently installed inside the magnet: they can be positioned in the beam commissioning periods and then removed for the EDM measurement. Nevertheless, an event-by-event measurement of the muon trajectories would be extremely beneficial in suppressing systematic effects in the final phase of the experiment, and the experience gathered with these detectors in the first phase would be the basis for future developments in this direction.

We considered two different setups, the first optimized for the measurement of the injection angle and the second for the momentum. Indeed, both detectors will be able to measure all kinematic quantities together, with some resolution. Detailed simulations will be performed to understand if using just one of them could be enough to reach all the goals of the muon tracking system.

### 1. Measurement of the injection angle

The measurement of the longitudinal injection angle is the most affected by the beam-matter interaction because of multiple Coulomb scattering (MS). A gaseous detector with an extremely light gas mixture and an extremely thin, vacuum-tight entrance window is necessary and, even with the lightest gas mixture one can reasonably foresee, the angular information would be spoiled after a few centimeter. With such a short lever arm, a single-hit resolution of $O(100\,\mu\mathrm{m})$ is necessary to reach $O(1\,\mathrm{mrad})$ angular resolution.

The optimal solution for this application is a Time Projection Chamber (TPC) with the high granularity readout provided by GridPix [63].

GridPix is a gaseous detector made of a conductive mesh implanted 50 μm above a Timepix chip [64]. A voltage difference between the mesh and the chip produces an avalanche when drift electrons reach the mesh, so that the GridPix behaves like a sort of microscopic Micromegas. The charge is read out by the Timepix pixels, and the combination of the thin multiplication gap and a micrometer-level alignment of mesh holes and pixels lets each drift electron fire only a single pixel, so that one obtains one hit per ionization electron, with a spatial resolution only limited by the pixel size (50 μm) and the diffusion in the drift region.

Due to the tight geometrical constraints in the first phase experiment, a geometry with a radial drift field has to be deployed: muons ionize the gas between two coaxial electrodes at different voltage, producing electrons that drift toward the inner one, where a few GridPix detectors are installed. A sketch of a possible geometry is shown in Fig. 16. The muon enters the TPC through a very thin, vacuum-tight window, curls within the chamber, and then exits through another similar window. Simple calculations show that, at 28 MeV/$c$, the MS in the entrance window is likely to give the dominant contribution to angular resolution. A 100 nm Silicon Nitride window, as used in x-ray spectroscopy applications, would give a 2 mrad contribution, comparable to what can be achieved in terms of tracking resolution or MS within the chamber, resulting in a total resolution of about 4 mrad. Unfortunately, these windows can only bear 1 bar gas pressure against vacuum if their size is smaller than $2 \times 2$ mm$^2$. We will investigate the possibility of operating a GridPix TPC with a gas pressure well below the atmospheric one, to reach at least $10 \times 10$ mm$^2$. As an alternative and easier solution for larger windows, the vacuum tightness of 2 μm aluminized Mylar in this range of sizes will be investigated, although in this case the material budget would be equivalent to about 500 nm of silicon nitride, which would allow an area of $8 \times 8$ mm$^2$. Therefore, the best compromise between window size and angular resolution has to be found.

Very light gas mixtures can be used in this TPC to minimize the contribution of material effects to the tracking resolution. For this purpose, the GridPix have been extensively tested during beam times in 2022 with helium-based mixtures (see App. B) and additional laboratory tests will be performed at low pressure in 2023. In this respect, it has to also be noted that the high specific ionization of muons at 28 MeV/$c$ will produce enough ionization electrons to make the single-hit resolution a subleading contribution to the angular resolution, even at low pressure.

In the final experiment, the higher momentum (125 MeV/$c$) would strongly reduce the MS contribution, making it easier to reach $O(1\,\mathrm{mrad})$ resolution.
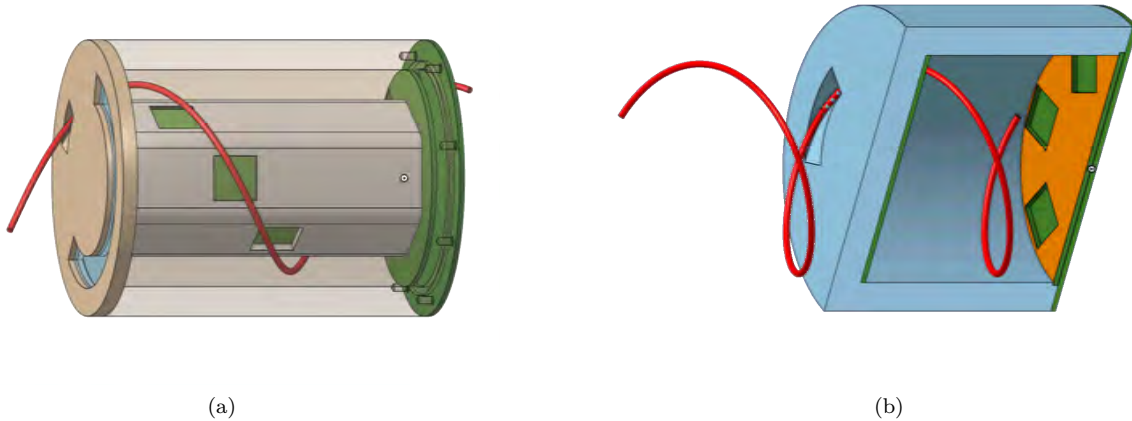
Figure 16: Sketches of possible geometries for the TPCs to measure the muon injection angle (a) and momentum (b, section view). The green squares in the electrodes correspond to the position of the GridPix sensors. The red helix represents a hypothetical muon trajectory.

### 2. *Measurement of the muon momentum*

The muon momentum can be precisely measured by a conventional longitudinal TPC placed right after the GridPix-TPC or installed as a standalone detector. The muons will enter through a thin window, on the cathode side. In this case, the thickness of the window is less problematic because energy loss fluctuations can be kept well below the target resolution of 0.5% even with a relatively thick foil. The geometry of the chamber will be tuned so that the muon will make at least one full turn inside the active volume, before exiting from the anode side, in order to maximize the sensitivity to the curvature radius. Ionization electrons will drift along the longitudinal axis, and will be collected by a gas multiplication and readout structure, possibly again a set of GridPix sensors. Single-hit resolution will be dominated again by diffusion. With an appropriate mixture, the diffusion coefficient can be kept well below $500\,\mu m/\sqrt{cm}$, so that the required resolution on a 30 mm curvature radius can be ensured by the high number of hits that is expected even with the lightest gas mixtures. A sketch of a possible configuration is also shown in Fig. 16.

### C. The uniform magnetic field

In 2022, we measured the magnetic fields of two suitable superconducting (SC) solenoid magnets. The "phase space conversion" (PSC) magnet, shown in Fig. 17a, with an inner bore diameter of 200 mm and a length of 1000 mm. The coil is made of multi filament NbTi and the magnetic field can be raised to 5 T and operated in persistent mode, i.e. the SC coil can be disconnected from the current supply once the desired field strength is reached. The alternative is the Ben magnet, shown in Fig. 17b, with a bore diameter of 300 mm and length of 650 mm, which can be raised to 4 T without persistent mode. Both solenoids consist of a principal solenoid coil and two correction coils made of a low-temperature superconductor. Table IV shows a summary of the main features of the two magnets.

In this proposal, all concepts are tailored to the PSC magnet as the muon group has ample experience with its operation, and the magnetic field has long been well known.

The magnetic field of the second magnet, also known as the Ben magnet, was not known over the volume of the bore until we measured it in autumn 2022. The obvious advantage of the Ben magnet is its larger bore diameter, which simplifies the installation of the injection and detection scheme and increases the positron acceptance. However, this advantage is offset by the requirement to add a vacuum chamber inside the bore, as the magnet housing does not permit setting the bore directly under vacuum. Furthermore, the shorter length also results in a shorter available duration between the generation of the muon entrance trigger and the magnetic pulse. In addition, we required up to 100 L of liquid helium per day during operation, which included two slow field ramps.

Figure 18 shows contour plots of the magnetic fields of the PSC and the Ben solenoid. The fields were calculated by fitting the magnetic field generated by a solenoid coil with a correction coil pair to the measured data. The injection spiral enters from negative $z$ values with a decreasing radius from about 41 mm to 32 mm of the final muon storage orbit. The dashed white line indicates the field profile at $r = 32$ mm while the
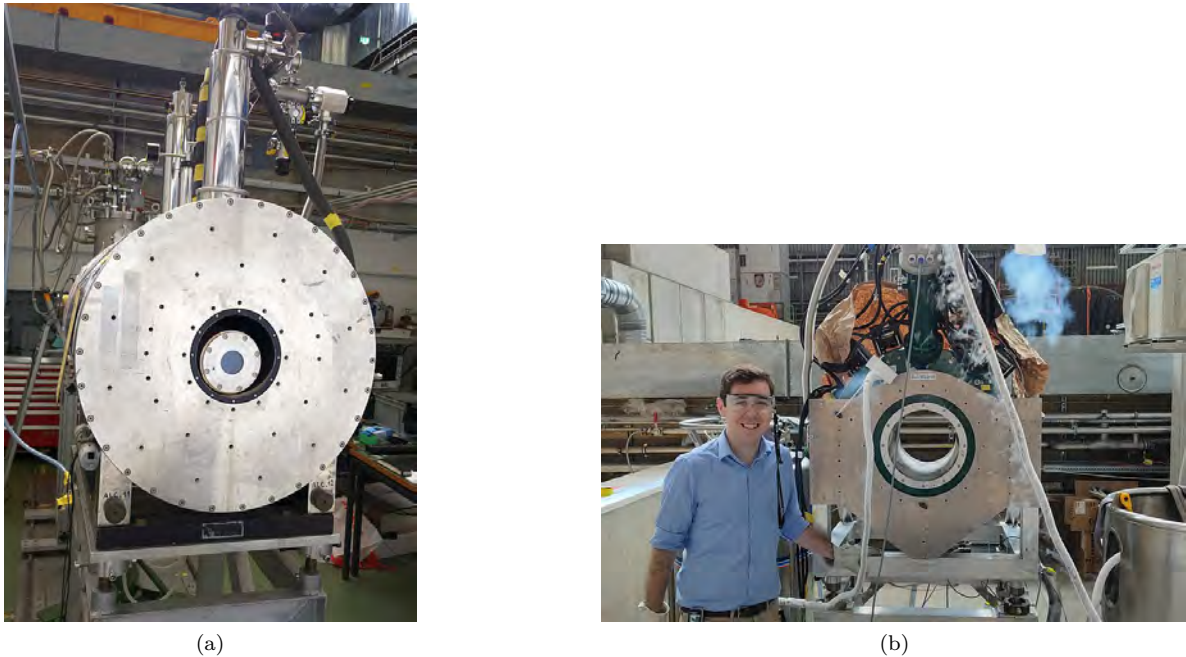
(a)            (b)

Figure 17: The PSC solenoid (a), here with an experimental insert inside the bore for muCool tests, and the Ben solenoid (b) are considered to host the experimental setup.

|  | PSC | Ben |
|---|---|---|
| Max B-Field /T | 5 | 4 |
| Persistent mode | yes | no |
| Solenoid length /mm | 1000 | 650 |
| Bore diameter /mm | 200 | 300 |
| Time trigger to pulse /ns | 145 | na |

Table IV: Table of main parameters characterizing the two available superconducting solenoids.

solid line is along the solenoid axis. Figure 19a shows the field profile along $z$ for the PSC and Ben magnet. Although the field of the Ben magnet smoothly falls as $|z|$ increases, the PSC magnet clearly shows a second local maximum around $\pm 250$ mm. For a highly efficient injection, we require a monotonically increasing magnetic field towards the center of the magnet. For muon storage on a stable orbit, we need a symmetric weakly-focusing field around $z = 0$, which results in a local minimum, generated by a local coil.

Figure 19b shows the magnetic-field amplitude along the line where the injection tube will be placed inside the PSC solenoid. Although the field in the first 15 cm is well below 1 T, we will use in this region a superconductor magnetic shield with a shielding factor greater than 200 [65], see Sec. VII D, to avoid any hysteresis effect close to the magnet bore. At distances greater than 15 cm we will consider using an iron tube with a wall thickness of a few millimeters as a magnetic shield, since it would not require cooling and yet still provide a sufficient shielding factor greater than 200 [66].

At the time of writing we are preparing a first baseline simulation for the injection of muons into the Ben solenoid. This will provide a good first estimate of the time required between the trigger and the magnetic pulse. In the case that this is similar to the PSC value, it is likely that the Ben solenoid is more favorable for the muon EDM test bed, given the larger bore diameter and the smoother magnetic field. Nevertheless, an additional vacuum tube inside the bore as well as further investigations into the large helium consumption will be required.

### D. Offaxis injection into the solenoid

Muons from the exit of the $\pi$E1 beam line need to be transported in a magnetic field-free region as far as possible into the strong magnetic field of the storage solenoid. As a first step we will demonstrate the
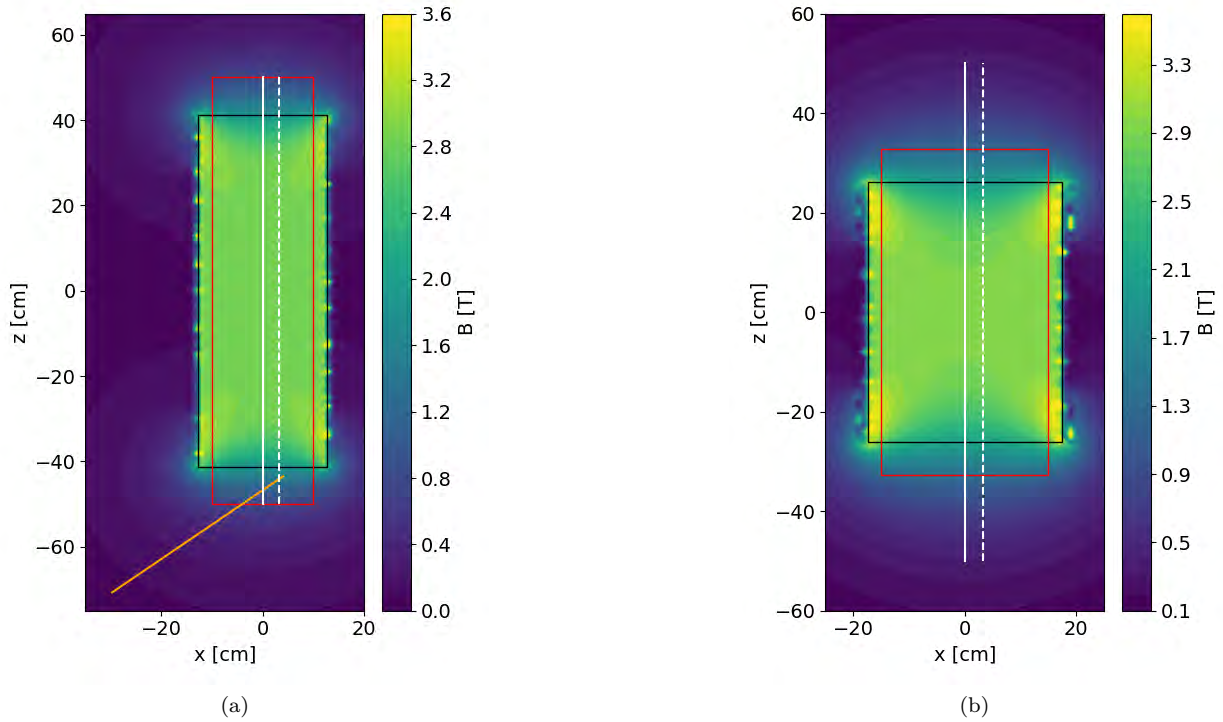
Figure 18: Contour plots of the magnetic field component $B_z$ of PSC (a) and Ben (b) solenoid magnets. The bores are indicated as red rectangles. The magnetic field along the solid and dashed white lines is shown in Fig. 19a. The field along the orange line, indicating the position of the injection tube, is shown in Fig. 19b.
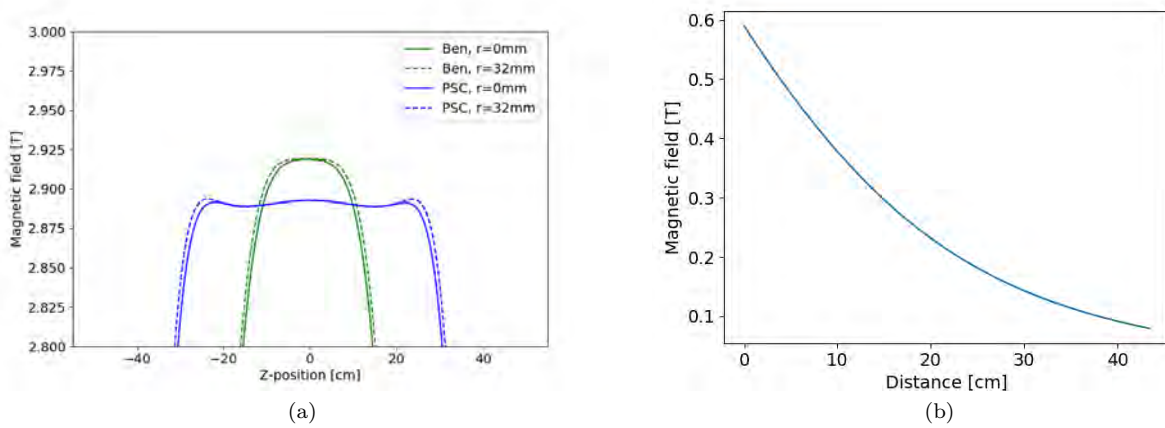


Figure 19: (a) Magnitude of the magnetic field component $B_z$ for $x = 0$ (solid) and $x = 32\,\mathrm{mm}$ (dashed) for PSC (blue) and Ben (green) solenoid. (b) Magnitude, $|B|$, of the magnetic field along the injection tube without magnetic shield.

off-axis injection into the solenoid through a collimation channel inside a magnetic shield by measuring the time of flight between an entrance detector at the end of the injection channel and a detector at the center and the far side of the solenoid.
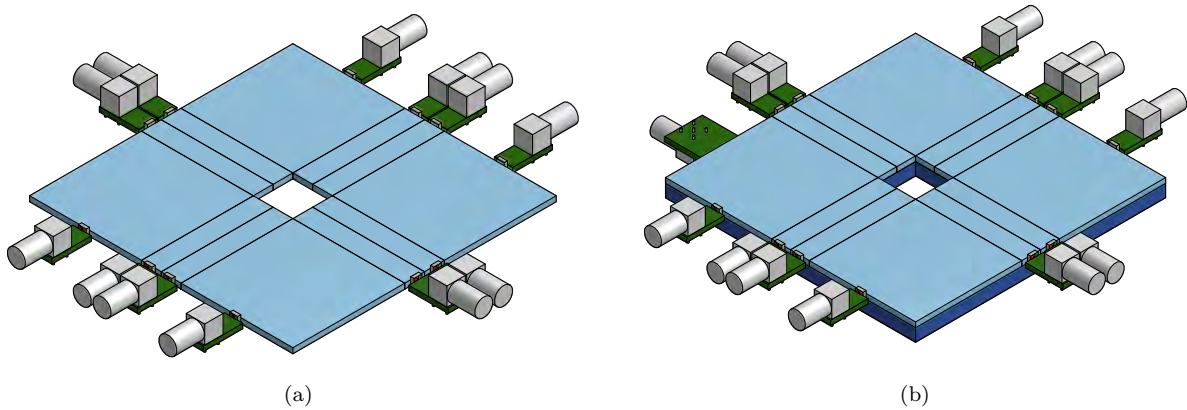
Figure 20: A sketch of the two possible realizations of the muon entrance monitor. (a) A single layer of ~ 2 mm thick scintillators adding up to twelve channels. (b) Additional thicker (~ 5 mm) 1-channel layer is placed behind the thinner 12-channel layer to improve muon vs. positron discrimination.
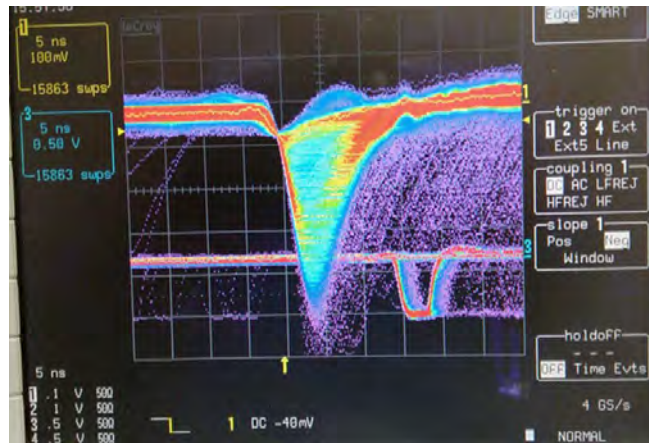


Figure 21: An image demonstrating the discrimination power between muons and positrons. A 2 mm thick plastic scintillator is placed in the beam containing particles with the momentum of 28 MeV/c. Positrons, being minimum-ionizing particles, deposit much less energy than muons, resulting in lower-amplitude pulses.

### 1. Muon entrance monitor

The muon beam must be precisely focused on the opening of the injection tube. Figure 20 shows a drawing of the two possible realizations of the muon entrance monitor. The center of the beam passes through the central hole the size of the injection tube (~15 mm diameter, corresponding to approximately $2\sigma$ around the center of the beam), while the tails of the beam are measured using scintillators coupled to silicon photo-multipliers (SiPM)s. The scintillator segments will monitor muon intensity and position. By rotating the entire detector around the tube axis, the count rates of up/down, left/right can be calibrated. Once calibrated, the beam position can be centered by tuning $N_{\text{up}} - N_{\text{down}}$ and $N_{\text{left}} - N_{\text{right}}$ to zero.

Since the beam also contains positrons, the entrance monitor should have the capability of muon-versus-positron discrimination. A plastic scintillator of 1-2 mm thickness (Fig. 20a) will fully absorb the surface muons, while positrons, as minimum-ionizing particles, will deposit only a small fraction of their energy. Figure 21 shows an example of pulses produced by muons and positrons in a 2 mm thick scintillator. To further improve the identification of a possible positron contamination, a thicker (up to ~5 mm) scintillator layer (Fig. 20b) could be added to the entrance monitor, in which the positrons will deposit enough energy for the pulse height to be well above the noise levels.
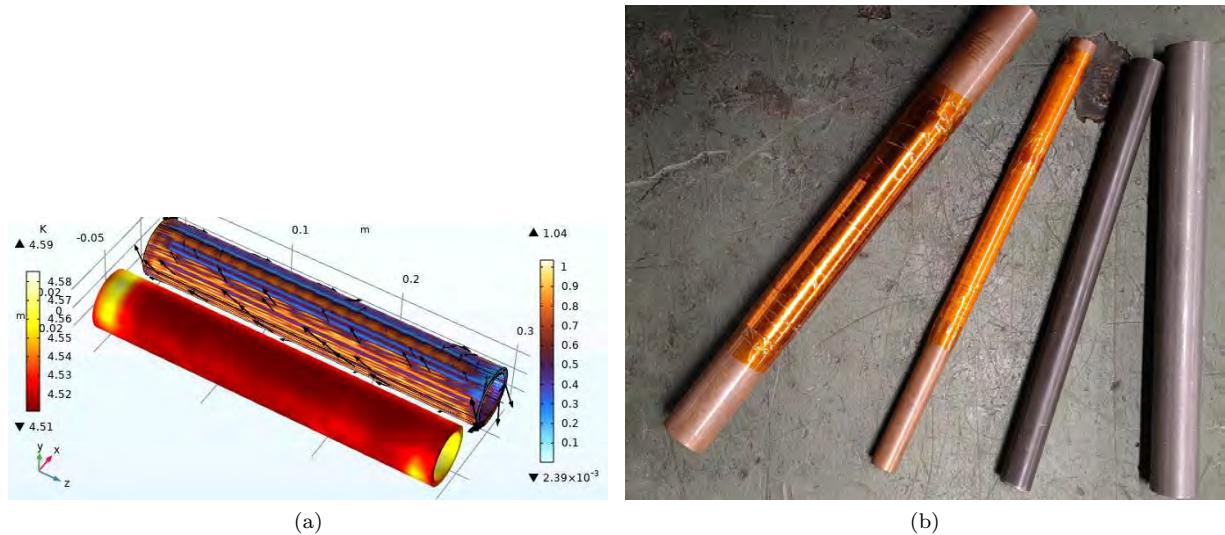
Figure 22: (a) Finite element calculation of an injection tube made of a superconducting sheet. (b) First prototype magnetic shields for the injection channel. On the left, two versions made of high temperature superconducting tape wound onto a copper tube. On the right, two standard iron tubes that might be used in the region with fields below 1 T.

## 2. *Injection channel and superconducting magnetic shield*

In the fringe field of the solenoid magnet, far from the bore to reduce hysteresis, we will use a thick iron tube as a magnetic shield. Above 0.3 T, closer to the storage region, a superconductor (SC) shield will be deployed. More than 50 years ago, Firth et al. demonstrated this technique for a 1.75 T bubble chamber at CERN [67] and is today used, for example, in the BNL / FNAL (g-2) experiment [68]. The principal idea is that once the superconducting shield is cooled below the critical temperature $T_c$, ramping of the outside field will induce persistent currents inside the superconductor to counteract the outside field. Hence, the field inside the SC shield will remain as low as before the magnet was ramped. This effect persists if the shield is sufficiently thick and the mean lifetime of the shielding current is long enough. Once the field starts to penetrate, the outside field needs to be ramped down and the superconducting shield can be reset by warming up above the critical temperature.

We will test Nb-Ti/Nb/Cu sheets, from the Wigner Research Center in Budapest, wound and clamped around a copper tube of ID=15 mm, and a design based on high-temperature superconducting (HTS) ribbons/tapes wound helically onto a copper tube of the same diameter. Similar tests [65, 69] showed promising results for the Nb-Ti/Nb/Cu sheets, while the HTS ribbon design did not adequately protect against the outside field. We will investigate whether different mounting techniques and more layers of helical wound HTS[6] [70], with a critical temperature $T_c \approx 88$ K result in a sufficient shielding factor. This would be favorable because only the liquid nitrogen temperature will be required if the final experiment's magnet also deploys HTS coils.

We are currently preparing finite element models of superconducting shields, for illustration, see Fig. 22a, to benchmark single-layer models against physical prototypes, see Fig. 22b.

For the HTS shields, we are setting up a test facility using a liquid nitrogen bath and a Helmholtz coil. We will measure the shielding factor by taking the magnetic-field ratio inside the tubes when the coil is ramped to the maximum field at room temperature and 70 K. In parallel, we will also build a prototype made of Nb-Ti/Nb/Cu sheets borrowed from CERN.

The superconducting tubes need to be cooled to below the critical temperature. To make sure that both versions will work, we will use a flow-through cryostat, e.g. ST-400 from Janis or a similar model from Cryovac, that cools the tube to liquid helium temperatures. A total cooling power below 15 mW is required to cool both injection tubes, the upper (for clockwise injection) and the lower (for counter clockwise injection), to 4.2 K. The evaporated cold helium will be used to cool the 70 K thermal-radiation shield surrounding the
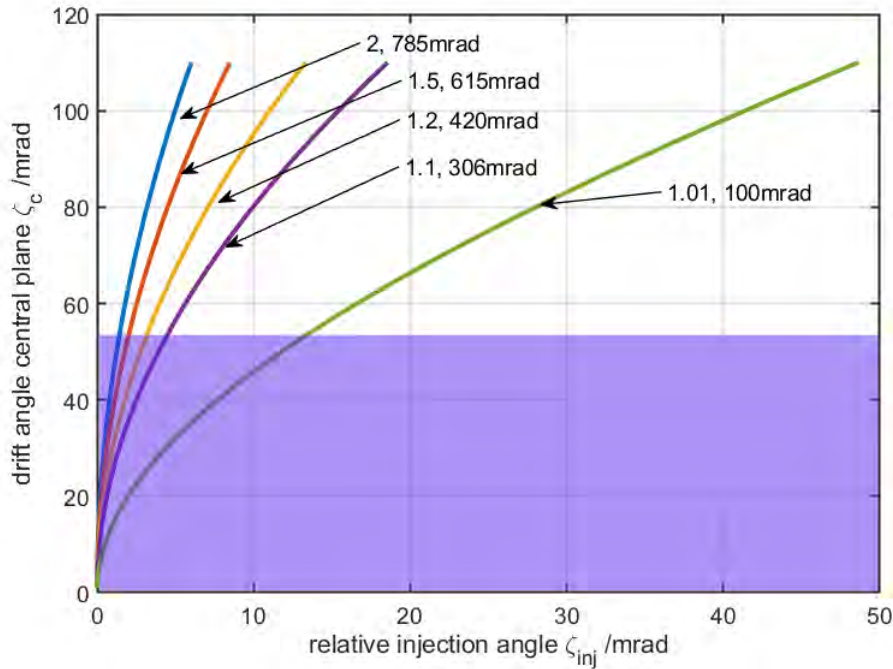
---

[6] S-Innovations 2G HTS wire 12-20Ag-5Cu-38H

Figure 23: Injection angle offset $\Delta\zeta_{\text{inj}}$ versus drift angle $\zeta_c$ in the center of the magnet. Each data pair indicates the ratio $B_c/B_{\text{inj}}$, and the nominal injection angle $\zeta_{\text{inj}}$, which results in $\zeta_c = 0$. Note that a nominal injection angle $\zeta_{\text{inj}} = 0$ is a lateral injection.

SC shield. The cryostat will be mounted at the entrance of the PSC solenoid. Then both injection tubes will be mounted to the cold finger of the flow-through cryostat, and the shielding factor inside the fringe field of the solenoid will be measured.

### 3. Position and inclination of the injection channel

The magnetic field and the resulting trajectory of a muon are intrinsically linked. It will require many iterations to identify the optimal magnetic-field configuration that permits efficient injection and achieves a stable and well-defined central orbit within the storage region where the frozen-spin condition is satisfied. The following considerations and mechanical constraints define the position where the magnetically-shielded channel ends inside the solenoid bore and the entrance trigger is placed.

1. Magnetic adiabatic collimation increases an initial beam divergence $\Delta\zeta_{\text{inj}}$ in the injection area (with magnetic field $B_{\text{inj}}$) to

$$\Delta\zeta_c = \arccos\left(\sqrt{\frac{B_{\text{inj}}}{B_c}}\cos(\Delta\zeta_{\text{inj}})^2\right), \tag{64}$$

where $\Delta\zeta_c$ is the divergence in the center of the solenoid with magnetic field $B_c$, see also Fig. 23.

2. The injection channel is inclined by an angle $\theta = \pi/2 - \zeta_{\text{inj}}$ with respect to the axis of the solenoid bore. This angle depends on the $z$-position along the injection helix and defines the maximal insertion of the channel into the solenoid, given the mechanical constraints.

3. The larger the distance of the injection region from the storage region and the more uniform the field, the longer will be the time available to trigger and generate the magnetic pulse.

Figure 24 shows the simulation result of an optimal injection trajectory for a magnetic field based on the magnetic measurements discussed in Sec. VII C and optimized by placing additional coils in the simulation to increase uniformity for large $z$ and create a weakly-focusing field at the center of the solenoid. The angle,
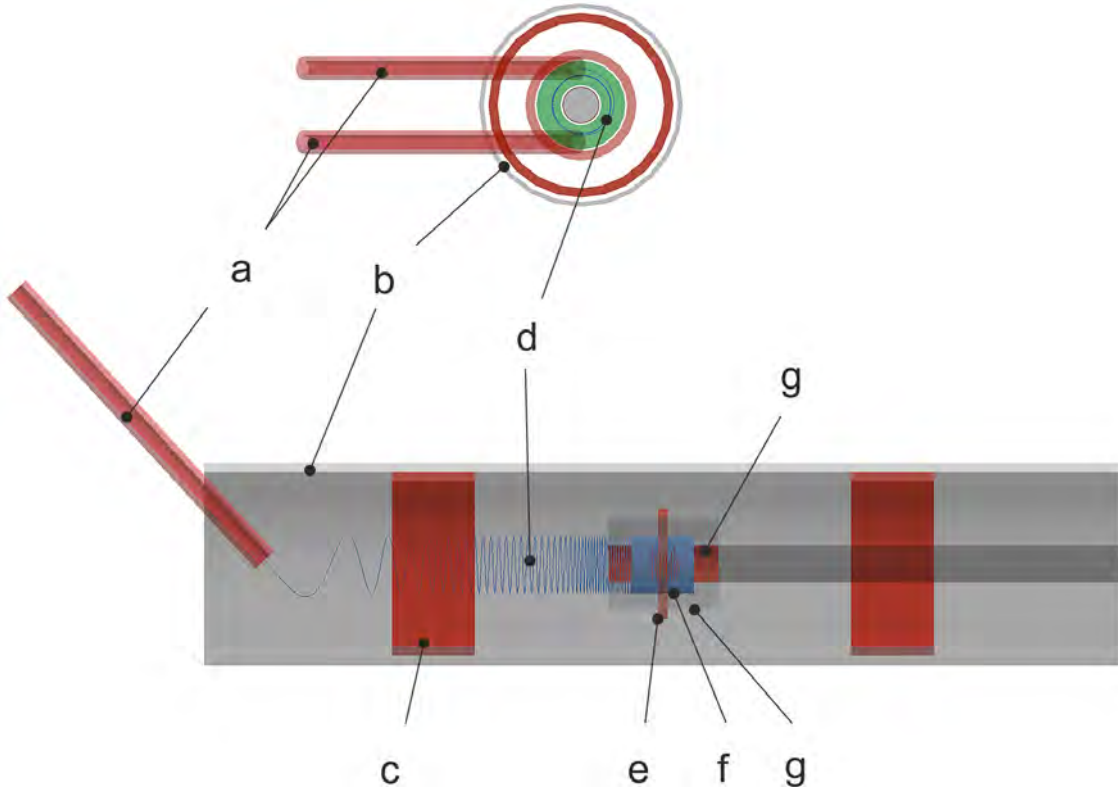
Figure 24: Rendered image of the simulated injection into the PSC solenoid of muons. Top: view from the front. Bottom: view from above. (a) Injection tube, (b) solenoid bore (not showing the coil etc, (c) correction coil, (d) injection helix, (e) weakly-focusing coil, (f) stored muon trajectory, (g) ground (outer cylinder) and high-voltage (inner cylinder). To change from clockwise to counterclockwise injection and storage, we will reverse the polarity of all magnetic fields and increase/lower the vertical position of the experiment by approximately 80 mm.

$\theta$, between the solenoid axis and the injection channel is 47.51° for the case without an electric field. In the case where the electric field is ramped for the frozen-spin measurement, the optimal injection angle reduces to 47.48°. Neglecting this small difference of 524 μrad would already result in a reflection of the injected muon. Fortunately, the remaining beam divergence after the injection tube is large enough that a successful injection for any electric field from $-E_f$ to $E_f$ is possible without adjusting $\theta$ by rotating the solenoid. To adjust $\theta$ and optimize the injection we will use a combination of a rotational mount for the solenoid and a dipole magnet, see Fig. 15, at the exit of the beamline. The vertical displacement of about 82 mm will be accomplished by a linear actuator.

As a final test of the injection channel, we will mount the two prototype tubes inside the cryostat attached to the PSC magnet at $\pi$E1, and measure the tube transmission and injection efficiency using a set of scintillating detectors along the solenoid. The time of flight from the entrance detector after the collimation tube to the detector in the central plane of the solenoid will give us an exact timing for the next step, the magnetic kick to store the muon on the central orbit.

### 4. Muon entrance trigger

The first simulations of the Phase I experiment indicate that only about 1.7% of the muons that have passed the injection channel can be stored in a stable orbit in the center of the solenoid. A Monte Carlo-based optimization of the second phase muon EDM experiment has shown that the injection efficiency can be dramatically increased by tuning the multivariate parameter space of injection, see Sec. VII D 5. At the time of writing, we are setting up a Monte Carlo simulation and a surrogate model based on polynomial chaos expansion in a genetic algorithm to optimize the injection parameters for Phase I. In any case, an entrance trigger is required to generate the magnetic kick in the center of the solenoid, see Sec. VII E, at the right moment when the muon passes the weakly-focusing field region. An entrance detector made of a thin
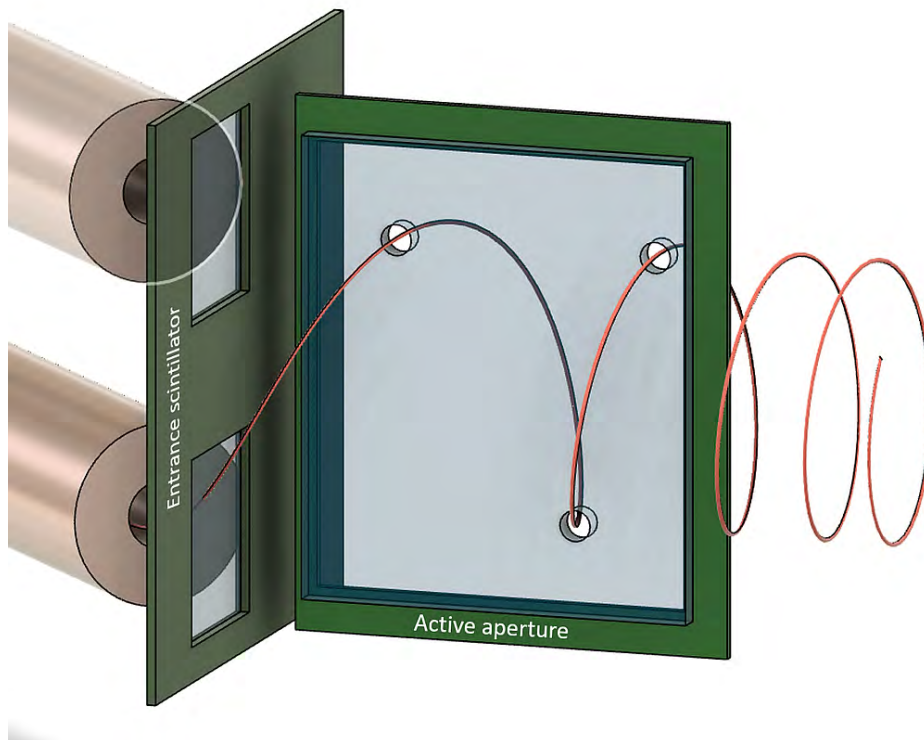
Figure 25: CAD sketch of the entrance trigger. On the left, the muons exit the collimation tube shielded by a SC shield. The strong magnetic field immediately bends the muons onto a spiral trajectory. First, they pass through a thin 100 μm BC400 entrance scintillator. A thick second scintillator forms an active aperture, with holes at positions along the reference muon trajectory, which stops and detects muons which are outside the acceptance phase space. A trigger for the magnetic pulse, see Sec. VII E, will only be generated in the case of an anticoincidence between the entrance scintillator and the active aperture.

scintillator tile (100 μm) in combination with a perpendicular thick scintillator (5 mm), which has openings around the nominal reference trajectory of the muon, will be used to create a trigger for the short magnetic pulse to deflect the trajectory of the muon into a stable orbit. Figure 25 shows the CAD of the entrance trigger with the injection trajectory. This trigger concept reduces the required pulse rate of the kicker power supply from about 30 kHz to 1 kHz.

### 5. Simulation of the injection

As a starting point for a machine learning optimization of the multivariate injection problem, we have set up a simulation in G4BEAMLINE. We simulate each of the injection steps separately, using the measured transverse phase space of $\pi$E1 as the initial input, see Fig. 26, and every simulation output is the subsequent input to the next simulation.

The first simulation step is the transmission through the injection channel of diameter $d_{\text{inj}}$. Manual optimization, which simulates the transmission of tubes with different diameters, indicates that $d_{\text{inj}} = 15$ mm is a good compromise in the selection and transmission of phase space. Figure 27 shows the phase space after the collimation tube with a total transmission of 3%.

In the next simulation step, we inject $1 \times 10^6$ muons, generated by using the transmission phase space of the collimator, into the manually-tuned magnetic field. After 107 ns a magnetic pulse is applied, using inverse currents in a split-coil pair with $r_{\text{KC}} = 55$ mm and separated by 100 mm. The current profile, shown in Fig. 28, was generated using the electronic scheme shown in Fig. 29. A total of 1.7% of the muons that have passed the collimation channel can be stored in the weakly-focusing field region.
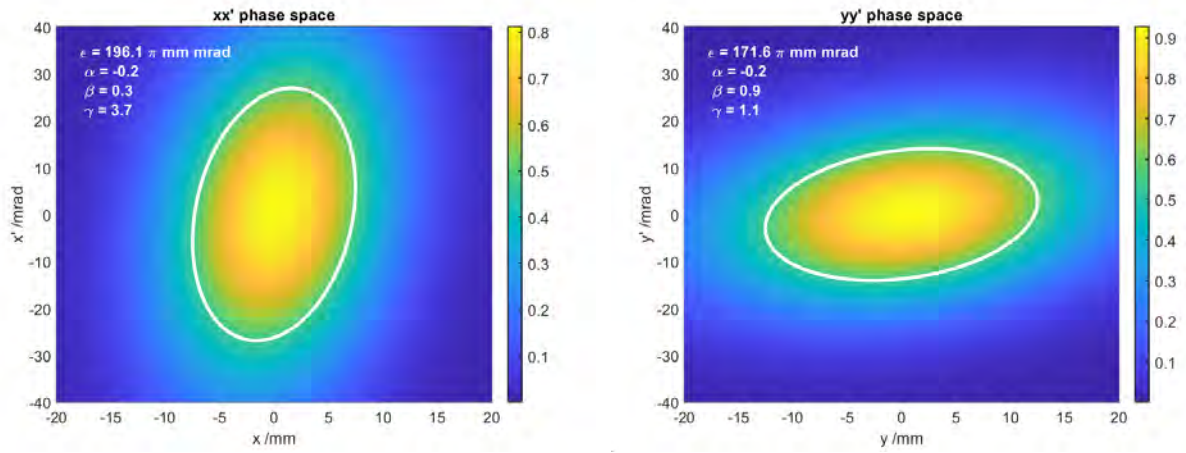
Figure 26: The Monte Carlo-generated $x$ and $y$-phase space of $\pi$E1 was used as input with the $5 \times 10^6$ events for a simulation of transmission through the collimation channel.
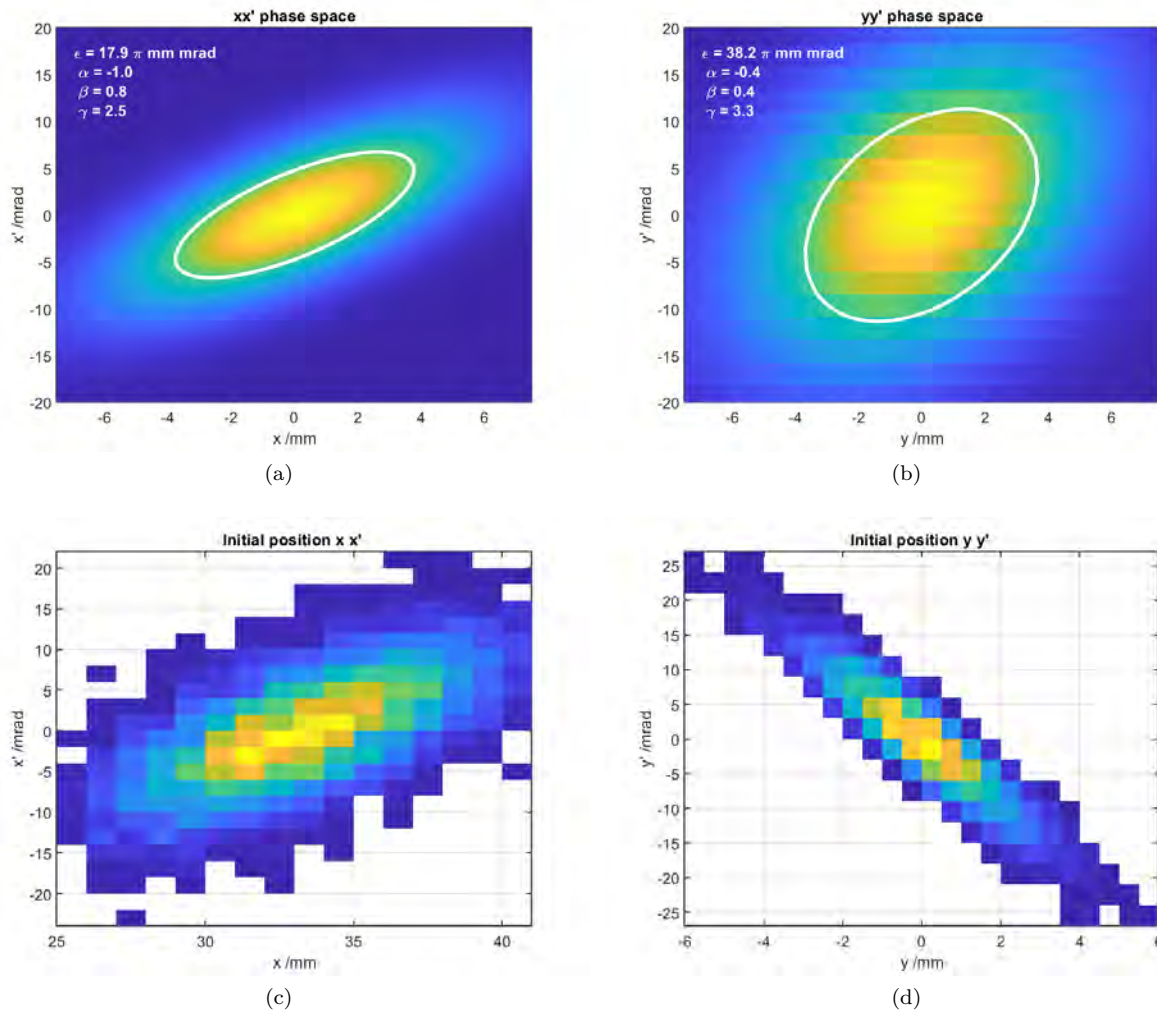


Figure 27: (a-b) Monte Carlo-simulated $x$- and $y$-phase space after transmission through a collimation tube with $d_{\mathrm{inj}} = 15\,\mathrm{mm}$ with a total transmission of 3%. (c-d) Fraction of the phase space shown in (a-b) that is stored in the central plane 240 ns after creation. Only 1.7% of the muons that reach the exit of the collimation channel can be stored.

**E. The magnetic pulse**

Once a muon has passed through the collimation channel, it will be detected by an entrance detector made of a thin scintillator tile. Muon trajectories within the phase space suitable for trapping in the solenoid will be selected by the anticoincidence of this entrance signal with a series of active apertures, as described in Sec. VII D 4. This trigger signal will initiate a magnetic pulse to trap the muon in the storage region given by the weakly-focusing field. The magnetic pulse is a quadrupole field produced using a pair of circular coils with counterpropagating currents, also known as anti-Helmholtz configuration.

The pulsed magnetic field must be of sufficient amplitude to cancel the muon's longitudinal momentum. Critically, the time delay between the trigger and the pulse must be sufficiently short to apply the pulse before the muon reaches the center of the solenoid.

Therefore, the injection angle, which defines the longitudinal component of momentum (Sec. VII D), as well as the length of the magnet bore (Sec. VII C), defines the constraint on the maximum time delay or pulse latency. Simulation studies indicate that pulse latency must be no longer than 120 ns to 150 ns. This requires strict minimization of all time delays in the system in order to relax the demand for the internal delay of the high voltage (HV) switch used in the pulse generator, which represents the most ambitious R&D effort towards achieving the required pulse latency.
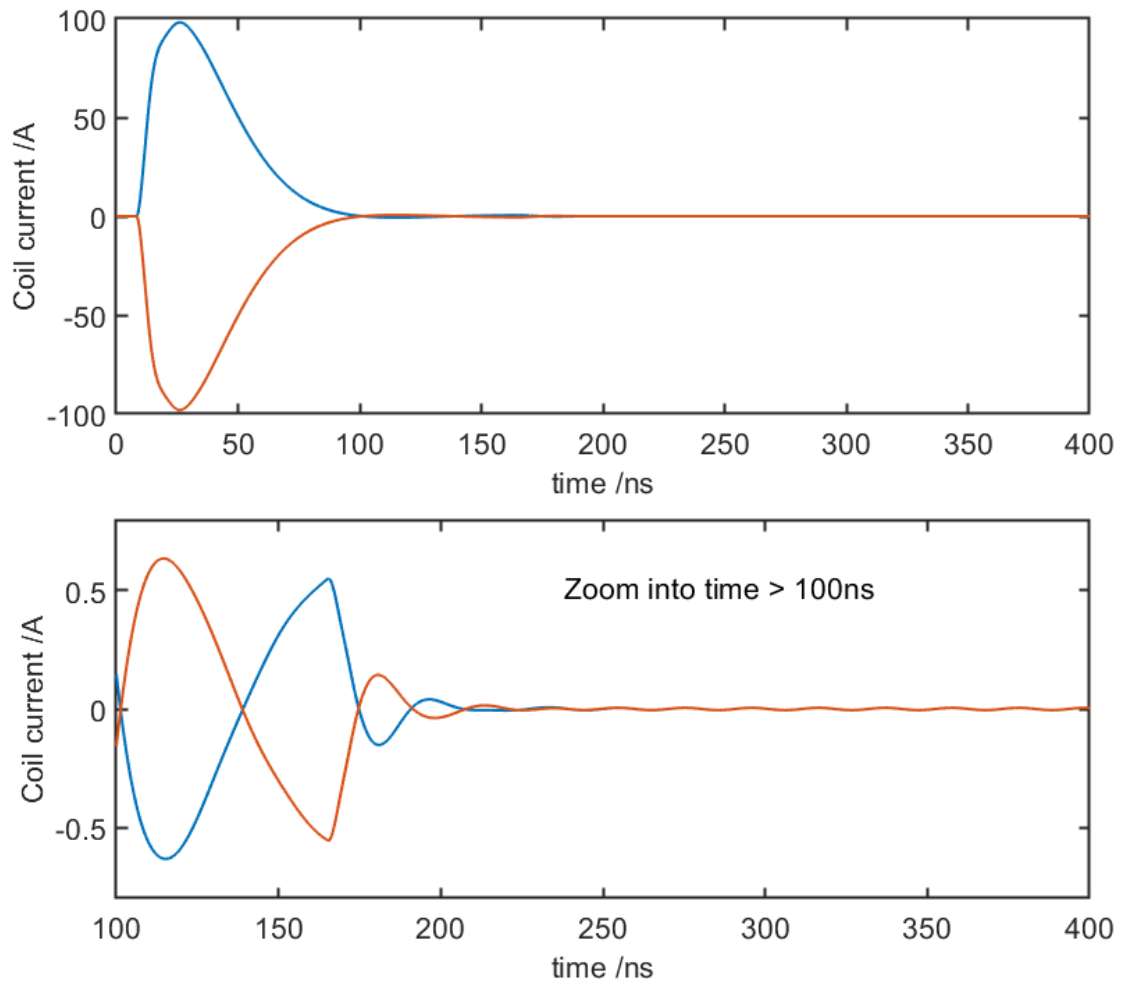


Figure 28: Currents in each of the two coils, L3 and L5 in Fig. 29, generating the quadrupolar magnetic pulse to deflect the muons into a stable orbit. The upper panel shows the full duration of 400 ns, while the lower panel shows a zoom in to the region with $t > 100$ ns. At time zero, the capacity C1 is fully charged with a high voltage of 7 kV. The fast switch, consisting of S1 and S2, closes at $t = 10$ ns and opens again at 160 ns. Closing and opening times are assumed linear transitions from 0 to 1 in 10 ns, while the switch remained fully open for 150 ns.
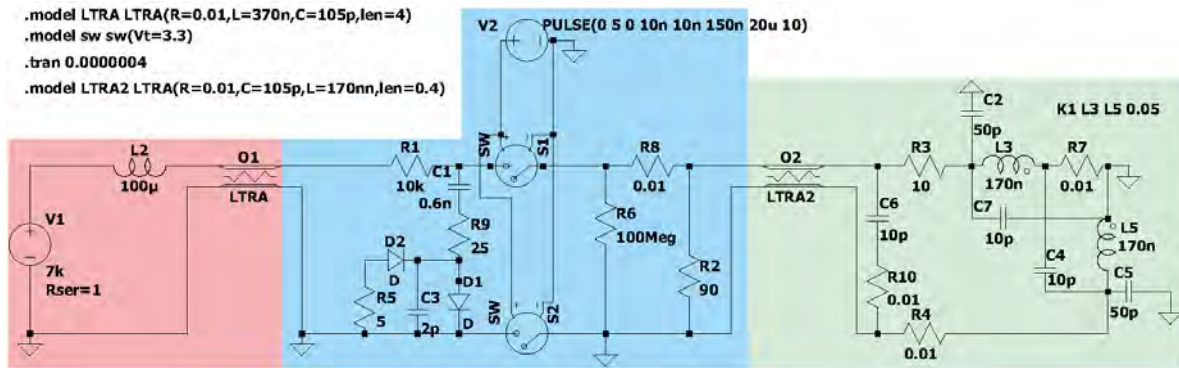
Figure 29: Electronic circuit for the generation of a short magnetic quadrupole pulse inside the solenoid. The circuit performance can be simulated using the LTSpice software to understand the characteristics of the current pulse supplied to the coils, shown as inductors labeled L3 and L5. The trigger signal is indicated by the voltage V2 and the mutual inductance is specified by the coupling K1 between L3 and L5. The parameters of the two transmission lines are specified by the two lossy transmission (LTRA) line models.
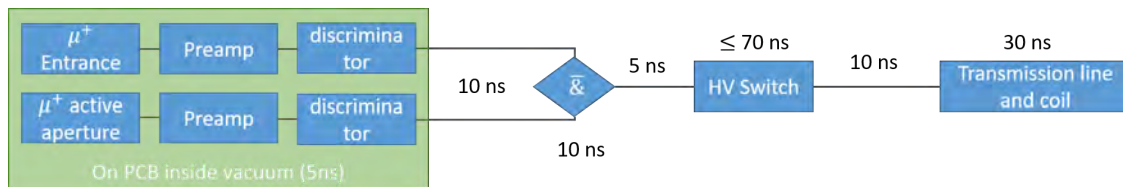


Figure 30: Schematic layout of the electronic chain to supply the current pulse to the trapping coils. Contributions to pulse latency in nanoseconds are labeled along with each component, including the estimated cable delays present. The trigger scalars from the scintillating entrance and aperture detectors will be generated on a PCB in vacuum, while coincidence logic will be done out of vacuum. The HV switch controlling the pulse generator will also be mounted out of vacuum but as close to the feedthrough as is practically feasible. A final contribution arises from the transmission line to the center of the solenoid where the coils are situated.

The electronic chain illustrated schematically in Fig. 30 outlines the various contributions to the total pulse latency that must be controlled. The scalars from the scintillating entrance and aperture detectors will be generated on a PCB in vacuum, within ~ 5 ns, and sent via coaxial cable and feedthrough to the coincidence logic unit outside, adding a delay of 10 ns. The coincidence logic requires approximately 10 ns [7], before the signal will be used to activate the HV switch in the pulse generator. The internal delay in closing the switch to generate the current pulse is the critical requirement that must be relaxed as much as possible by minimizing all other contributions to the total pulse latency. The current pulse is sent in vacuum through the feedthrough, adding another 10 ns, after which the transmission lines will carry it to the center of the solenoid to supply the coils, just in time for the arrival of the muon into the storage region.

In total, this results in a time delay of approximately 70 ns, excluding the internal delay of the HV switch. By mounting the switch and coincidence unit immediately adjacent to the vacuum flange, this could be reduced to a minimum of 60 ns. In the remaining 55 ns to 85 ns the switch must be fully closed to supply the current pulse to the coils that produce the pulsed magnetic field in the center of the solenoid.

A conceptual design of the circuitry for a pulse generator has been developed using the simulation software LTSpice and is shown in Fig. 29. The HV (7 kV) power supply is shaded red and charges the capacitor C1 in the blue shaded region, which is discharged after the closure of the HV switch controlled by the input voltage V2 (representing the trigger signal).The coils are indicated as inductors L3 and L5 in the green shaded region, each with an inductance of 170 nH corresponding to a coil radius of approximately 50 mm and assuming a wire radius of approximately 5 mm. The mutual inductance is estimated to be around 8 nH for a coil separation of approximately 100 mm, and this is indicated by the coupling factor K1 of 5% between

---

[7] c.f. Model V976 from Caen, https://www.caen.it/products/v976/

the inductors L3 and L5. This describes the coupling that arises from the currents induced in each coil by the magnetic flux from the other.

The simulated current pulse supplied to the coils is plotted over time in Fig. 28. The maximum current is ~ 100 A and the duration of the pulse is approximately 50 ns, where the integral of the pulse determines the kick applied to the muon.

An important requirement for the pulse generator is the suppression of any residual oscillations after the initial pulse. The lower plot in Fig. 28 shows a zoomed-in view of the current in the coils at times greater than 100 ns. Due to the weakly-focusing field, such small oscillations will not eject the muon from the storage region; however, they will introduce an oscillatory radial magnetic field and thus cause oscillatory precession of the muon spin resulting in systematic effects (see, Sec. VI). The impact of this effect on the sensitivity to the EDM-induced spin precession is currently being assessed to determine quantitative upper limits on the current allowable after the initial pulse. These limits, as well as the exact dimensions defining the inductance of the coils, will provide essential input for the production of a custom-built pulse generator. The demands on pulse latency, in particular, exceed the specifications of the HV pulse generators currently commercially available. However, several companies propose to study and design a custom-made pulse generator that meets our requirements.

As a first step, a physical prototype of the coils will be produced to directly measure their inductance. An existing pulse generator, with lower current and higher latency, will be used to characterize the magnetic field produced by the coils. This will facilitate an empirical study of the effect of introducing additional components of the experiment, such as the aluminum casing of the solenoid bore and the frozen spin electrodes. Each of these components will have inductive couplings to the coils, which will alter the timing characteristics of the current pulse and potentially damp the magnetic field seen by the muon in the storage region. In particular, the effect of eddy currents in the electrodes must be measured to ensure that the magnetic field strength inside the electrodes at the position of the muon orbit is sufficiently large. This will also inform the design of the electrode system, since the formed eddy currents will vary considerably between a continuous and segmented design of the cylindrical electrodes. The resistivity of the material used for the electrodes will also determine the propensity to form eddy currents. These empirical studies will complement and inform the concurrent development of a high-frequency simulation of the system to extrapolate the system behavior to the currents and switching latency that will ultimately be required. Together, these empirical and simulation studies will inform the design of both the trapping coils and frozen spin electrodes, as well as provide input for the commercial development of the required pulse generator.

In parallel to the aforementioned studies, we will investigate novel alternatives that could relax the requirement on the internal delay of the HV switch, should the current upper limit of ~ 70 ns prove to be not cost-effective. Relaxation of this latency could be achieved by gradually reducing the longitudinal momentum or by increasing the path length prior to the time-critical trapping pulse which must be applied as the muon enters the storage region. Various options towards both strategies are already being investigated. One possibility towards the latter is to use corrections coils to increase the magnetic field strength at the far end of the solenoid, such that an injected muon first passes the central region before it is reflected and subsequently trapped on its return transit of the storage region. This introduces the additional complication of asymmetry in the primary field, i.e. an asymmetric perturbation to the solenoid field. Nevertheless, the effect of such an asymmetry as a static field can be understood well using simulations. A dynamic solution could also be implemented in which the asymmetry could be suppressed in coordination with the timing of the magnetic pulse. Ongoing enhancements to experimental simulations and the incorporation of high-frequency electronic simulations will facilitate quantitative studies of these alternative strategies should they need to be adopted.

## F.   Electric field and high voltage

The frozen-spin condition is established for muons with a momentum of $p = 28$ MeV/c in a 3 T magnetic field with a radial electric field of about 3 kV/cm. We will adjust the electric field to match the frozen-spin condition by measuring the $(g-2)$-precession for fields between $-3.3$ kV/cm to $3.3$ kV/cm. The electrode system will consist of two coaxial cylinders made of conducting foils. With the radius of the inner charged high voltage electrode made as large as possible, i.e. 25 mm, and the outer grounded cylinder having a radius of 45 mm, we will need a high-voltage system supplying $U_{HV} = \pm 7.5$ kV, see Eq. (40).

The most stringent systematic effects are related to the orientation of the electric field (see Tab. II). Although a tilt or eccentricity of the inner cylinder with respect to the outer cylinder does not result in a systematic effect, any persistent longitudinal component of the electric field averaged over the muon orbit will lead to an EDM-like signal. Furthermore, the effective radiation length of the electrode material should be as small as possible to reduce the multiple scattering of decay positrons, which leads to misidentification of

the direction of the tracks (see Appendix A). As the entire set-up will be mounted in vacuum, excellent heat conduction needs to be guaranteed to ensure dissipation of the energy deposited by induced eddy currents inside the metal layer. Although the power deposition of a single magnetic pulse may be small, a repetition rate of about $2\,\mathrm{kHz}$ will lead to considerable heating.

We will develop, test, and implement a nested electrode design made of thin graphite or aluminum-coated Mylar foils and a support structure with minimal radiation length for positrons. An alternative option is to use very thin tungsten wires with small spacing, which would also be beneficial to reduce damping of the magnetic pulse.

## G.    Positron detection

The statistical sensitivity for the muon Anomalous Magnetic Moment (AMM) and EDM frequency measurement scales with $(\tau \alpha \sqrt{N})^{-1}$, c.f. Eq. (16), where $\tau_\mu$ is the muon lifetime, $\alpha$ is the asymmetry, and $N$ is the total number of positrons. In the case of the AMM, $\alpha$ is the difference between the inward and outward spins,

$$\alpha_{\mathrm{AMM}} = \frac{N_{\mathrm{in}} - N_{\mathrm{out}}}{N_{\mathrm{in}} + N_{\mathrm{out}}} \tag{65}$$

whereas for the EDM it is the difference between the longitudinal up and down spins,

$$\alpha_{\mathrm{EDM}} = \frac{N_{\mathrm{u}} - N_{\mathrm{d}}}{N_{\mathrm{u}} + N_{\mathrm{d}}} . \tag{66}$$

Figure 31 shows $\alpha\sqrt{N}$ as a function of the positron energy for both the AMM (left) and EDM (right). In the case of the forward-backward asymmetry of the AMM this shows sensitivity for positrons at energies above $0.3\,E_{\mathrm{max}}$. However, since the asymmetry changes sign at about $0.7\,E_{\mathrm{max}}$, the measurement requires a sufficient positron energy resolution.

In the case of the EDM, the sensitive energy range is above $0.4\,E_{\mathrm{max}}$. As no change in asymmetry occurs in this range, simple positron counting in the upstream and downstream hemispheres is sufficient. Note that the sensitivity for the EDM and AMM measurement depends on the energy cut, as $\alpha$ and $N$ depend on the detector energy acceptance and resolution. Furthermore, the value of $\alpha$ generally varies between the AMM and EDM measurements.

The AMM frequency measurement will be used for two purposes: measurement of the mean magnetic field, $\langle B \rangle = \omega_{\mathrm{AMM}}/a_\mu$ seen by muons within the storage zone; adjustment of the radial electric field to match the frozen-spin condition. For this we will measure the AMM frequency as a function of voltage and interpolate to zero frequency.

In all three cases, the critical aspect of the EDM search is the ability to measure the direction of the outgoing positron. In the next years we will demonstrate the three different steps in dedicated test beam times by demonstrating the storage of muons on a stable orbit, measuring $g - 2$ as a function of the electric field, and deploying the frozen-spin condition to search for the EDM.

From preliminary results, the resolutions required for the different studies are the following:

**Momentum:** a few MeV/$c$. This is mainly necessary to choose positrons with the desired asymmetry, which is shown to be momentum dependent, as illustrated in Fig. 31.

**Position:** Taking into account multiple scattering, a resolution of around $1\,\mathrm{mm}$ is sufficient for the fitting of the tracks with the required uncertainties in the direction. This result was achieved by geometric means, assuming that reliable timing information is available [71].

**Time:** less than $1\,\mathrm{ns}$. A positron from the decay of a $28\,\mathrm{MeV}/c$ muon travels at $c$, which means that in the magnetic field of $3\,\mathrm{T}$ a complete rotation takes $\lesssim 0.6\,\mathrm{ns}$. This imposes a limit on the resolution of the timing.

The collaboration will combine a scintillating fiber-based detection scheme with a silicon strip detector. This complementary design of two technologies permits us to profit from the excellent timing provided by scintillator technology and the complementarity of two independent schemes for tracking.
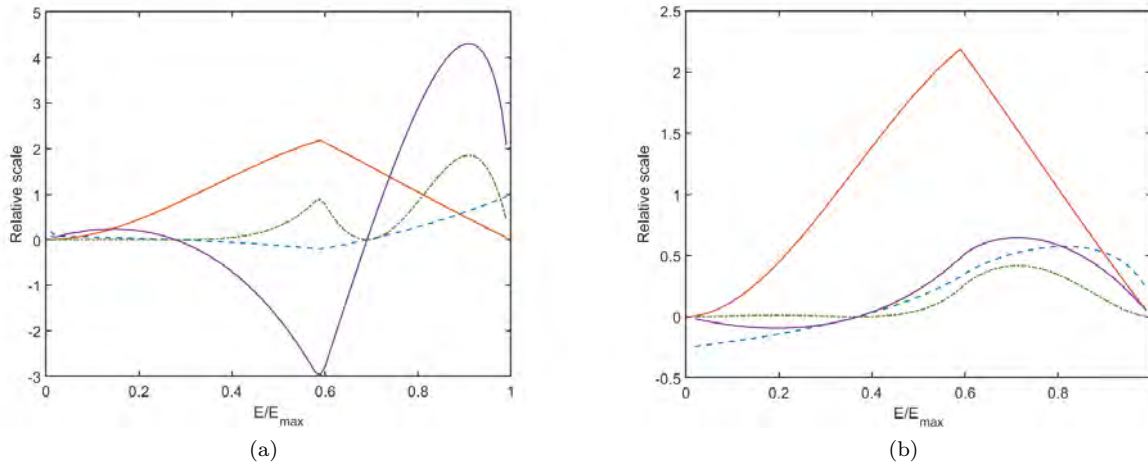
Figure 31: Statistical figure of merit for measurements of AMM (a) and EDM (b) using surface muons with a momentum of $28\,\mathrm{MeV}/c$ corresponding to $\gamma = 1.035$. (Red) Normalized positron energy spectrum, where $E_{\max} = 68.65\,\mathrm{MeV}/c$ is the maximum positron energy. (Blue dashed) Asymmetry $\alpha$. Note that in the case of AMM the asymmetry is negative between 0.3 and 0.7, while it is positive above 0.38 for EDM. (Green dot-dashed) $\alpha^2 N$ and (purple) $\alpha\sqrt{N}$ show the statistical sensitivity. While in the case of the EDM a detector system integrating over all energies above $0.4\,E_{\max}$ and distinguishing the emission hemisphere would be sufficient, a measurement of the AMM frequency to tune the electric field requires an energy resolution in order to distinguish decay positrons above and below $0.65\,E_{\max}$. Note that the positrons below $0.4\,E_{\max}$ do not contribute significantly to the measurement.

### 1. Kinematic Considerations

To ensure that the required momentum resolution to measure AMM is met, a tracking detectors will be needed. In practice this requirement will be met by a combination of the scintillating fibers, see Sec. VII G 6, and additional tracking layers. The following section presents a GEANT4 [58] based study that suggests a silicon based tracker is preferable to a straw-based tracker. A method for devising the optimal layout of the silicon layers to maximize the sensitivity to an AMM using simulations is also presented.

For this study the positron detector is confined longitudinally to the range $-50 < z < 50\,\mathrm{mm}$, and must be placed at a radius less than the magnet bore. This sets limits on the positron decay momenta that depend on the strength of the magnetic field. In Figure 32 the magnet bore radius is assumed to be $100\,\mathrm{mm}$, and the B-Field is set to $3\,\mathrm{T}$. Parallel and anti-parallel positron decays (with respect to the muon momentum) are shown to give an idea of the positron momentum ranges which can be detected. The tracking layers can be placed anywhere between the muon orbit and the magnet bore.

Figure 33 shows how the momentum of the positron changes with the orientation of the muons spin with respect to its momentum direction. This can be compared directly to Figure 31, which shows the average momentum and corresponds to $\hat{p}_\mu \cdot \hat{s} = 0$. The variation in the number of decay positrons as a function of momentum is the difference between the $\hat{p}_\mu \cdot \hat{s} = 1$ and $-1$ lines, and corresponds to the amplitude of the observed sinusoidal variation, were the spin to precess. When the fractional momentum $\lambda = 0.67$ there is no variation, so the number of decay positrons at this momenta will not vary. At this momentum there is no sensitivity to the AMM. Above (below) this momentum the number of decays will increase (decrease) as the muon spin precesses.

### 2. Detector Acceptance

Of course not every decay positron can be detected. The effect of acceptance on the detected positron momentum has been studied using simulation. Placing 2 cylindrical tracking detectors at $r = 35\,\mathrm{mm}$ and $r = 47.5\,\mathrm{mm}$, with both extending to $-50 < z < 50\,\mathrm{mm}$, and with the magnet bore at a radius of $100\,\mathrm{mm}$ the true momentum is shown in Figure 32b. In the simulation the muon orbit is constant at $r = 30\,\mathrm{mm}$, and the choice of radial detector placement is with respect to this fixed orbit. The expected betatron oscillations, which are not considered here, would rule out a detector at $r = 35\,\mathrm{mm}$.
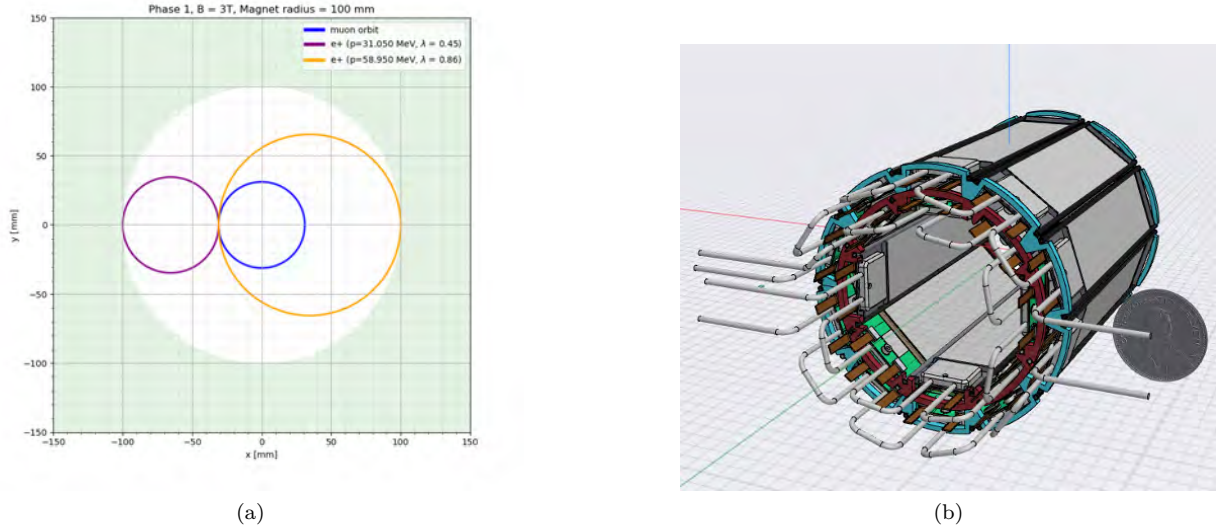
(a)

(b)

Figure 32: (a) Outward and inward positron decays that are contained with a radius of $100\,\mathrm{mm}$ in a $3\,\mathrm{T}$ magnetic field. A reference muon orbit is also shown. This simple model does not account for variation in the decay radius. (b) An example of 2 tracking detectors in place, surrounding the stored muons. Here they are placed at $r = 35\,\mathrm{mm}$ and $r = 47.5\,\mathrm{mm}$. Note the size of the $5\,\mathrm{CHF}$ coin.
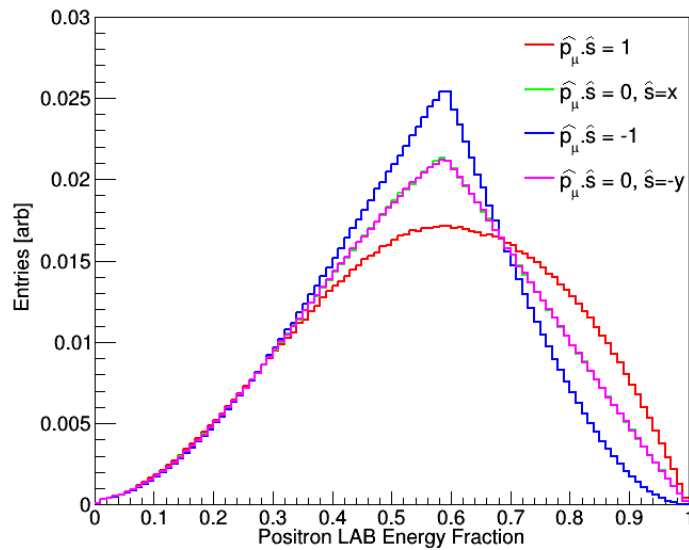


Figure 33: The positron decay momentum for different orientations of muon spin with respect to the muon momentum, as a function of the fractional momentum of the decay in the LAB frame. If the spin remains frozen then the momentum will follow the $\hat{p}_\mu \cdot \hat{s} = 1$ line.

Figure 34 shows the momentum of positrons that hit the detectors, as well as the ratio to all decay positrons, which can be thought of as an acceptance efficiency. The acceptance efficiency does not depend strongly on the orientation of the muon spin and momentum direction. For a momentum measurement at least 3 hits are required. The impact of this further constraint on the detected positron momenta can be seen in Figure 35. The requirement of at least 3 hits reduces the sensitivity of the AMM measurement, which is shown, together with the single hit case, in Figure 36. A completely flat line corresponds to no difference in the number of detected positrons for a precessing spin, and therefore no sensitivity to AMM. The problem here is that not enough of the positrons are re-curling around within the $-50 < z < 50\,\mathrm{mm}$ to ensure there are enough hits in the detectors. In fact only those with a very small longitudinal component of
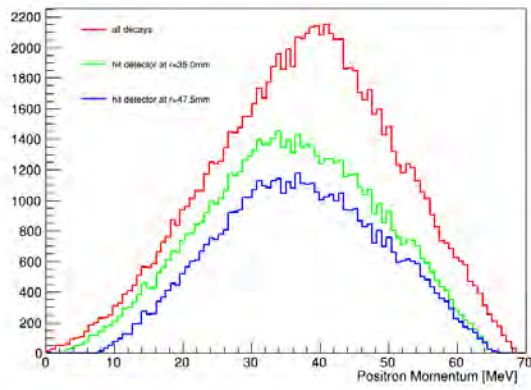
(a) Detected $e^+$ momentum, random spin
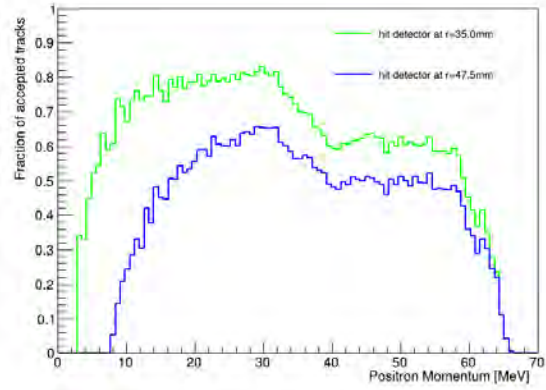
(b) Accepted fraction
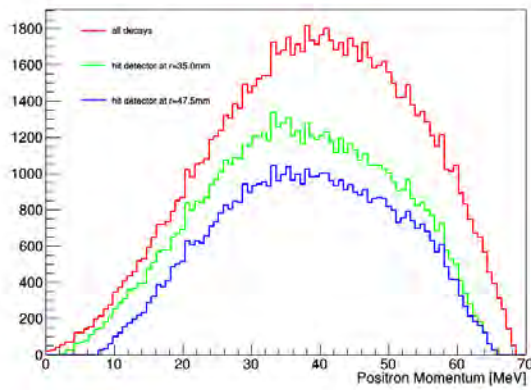


(c) Detected $e^+$ momentum, spin frozen
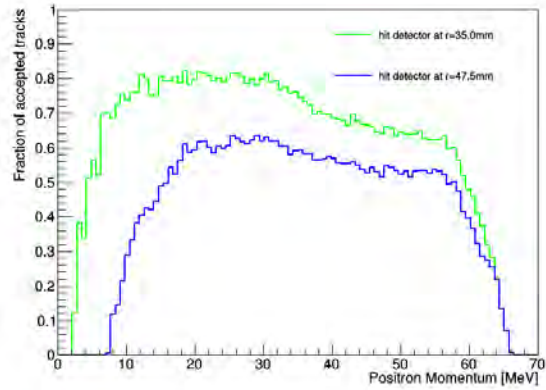
(d) Accepted fraction

Figure 34: The positron decay momentum for a random orientation of muon spin (top) and frozen spin (bottom). The green and blue histograms show the momenta when there are hits in the cylindrical detector planes placed at $r = 35$ mm and $r = 47.5$ mm. Any positrons that hit the magnet bore are not in these plots.

momentum have enough hits to be reconstructed. This can be counteracted by increasing the longitudinal span of the detectors, or by adding more layers at a different orientation. The latter option is studied in the next section.

### 3. Additional Tracking Layers

The orientation of the additional tracking layers is shown in figure 37. The example shown has 10 additional layers, but for the simulation only 8 were considered, spaced evenly around the muon orbit. Each petal extends from $50 < r < 80$mm. The silicon strips are still orientated in the same direction, so there is no sensitivity in the longitudinal direction. The increase in sensitivity to the AMM measurement can be seen in figure 38, where the configuration with 2 concentric layers and the additional petals is preferable. The sensitivity could still be increased further by adding more that 8 layers, or extending in the longitudinal direction. Note also that any positrons that hit the magnet bore are still ignored in this simulation, which needn't be the case when there are 3 layers which can possibly be traversed before hitting the magnet bore. Using these positrons would possibly increase the sensitivity to AMM further, particularly at higher momentum.
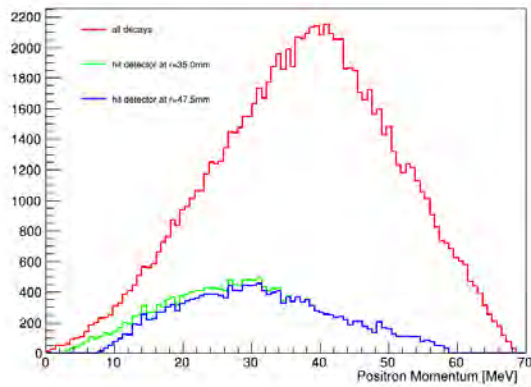
(a) Detected $e^+$ momentum, random spin, nHits > 2
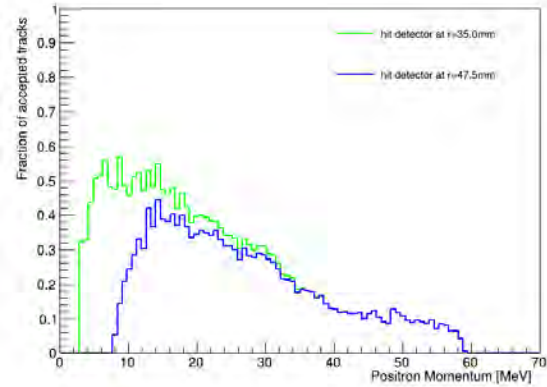
(b) Accepted fraction, nHits > 2
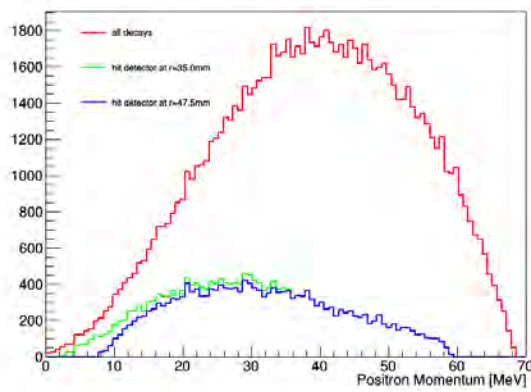
(c) Detected $e^+$ momentum, frozen spin, nHits > 2
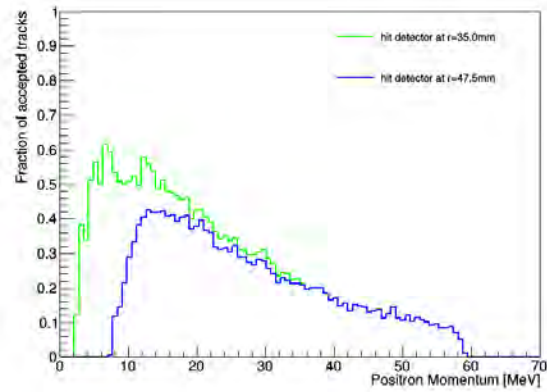
(d) Accepted fraction, nHits > 2

Figure 35: The positron decay momentum for a random orientation of muon spin (top) and frozen spin (bottom). The green and blue histograms show the momenta when there are hits in the cylindrical detector planes placed at $r = 35$ mm and $r = 47.5$ mm. Any positrons that hit the magnet bore are not in these plots.
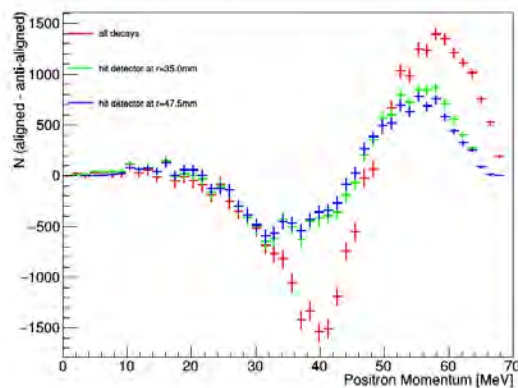


(a) AMM with detector acceptance
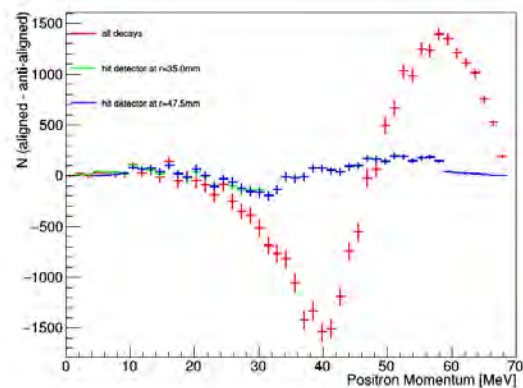
(b) AMM with detector acceptance, nHits > 2

Figure 36: The difference between the number of decays at each positron momentum when there muon spin and momentum are aligned and anti-aligned. The green and blue points are for when there are hits in the cylindrical detector planes placed at $r = 35$ mm and $r = 47.5$ mm. The right plot requires at least 3 total hits in the planes. Any positrons that hit the magnet bore are not in these plots. The red curves, which are identical in each plot, should be compared directly with the purple curve in Figure 31.
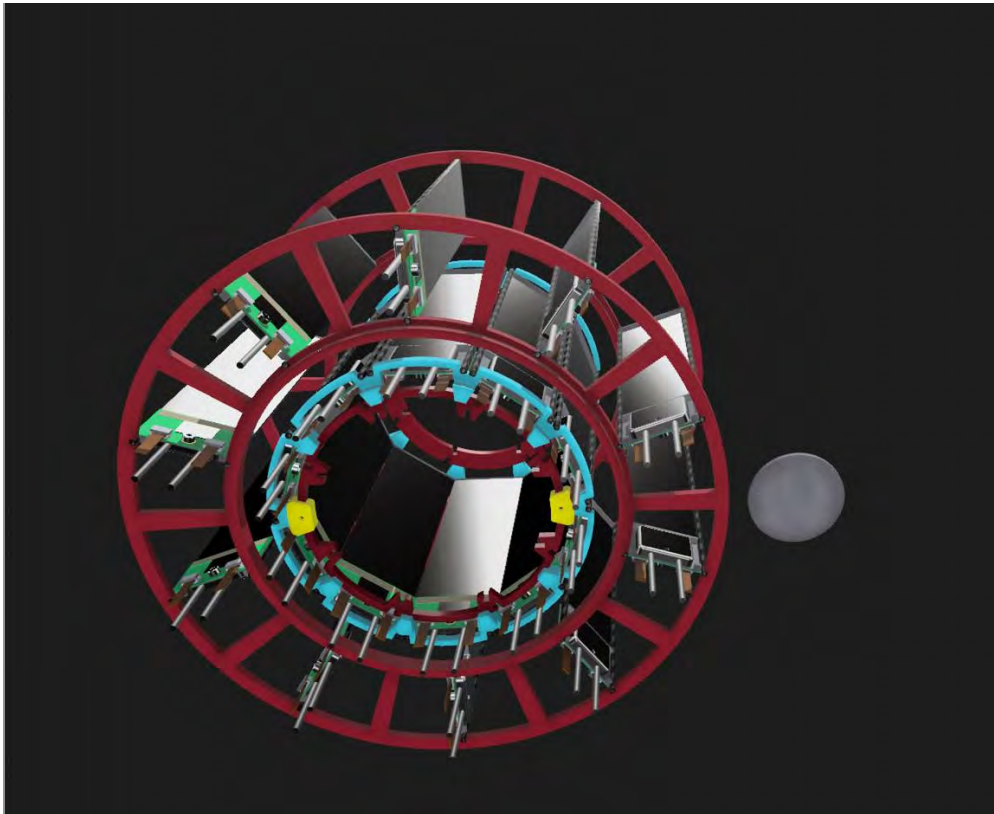
Figure 37: An extension to the original proposal, where the additional layers (here 10) are orientated in a petal formation around the muon orbit.
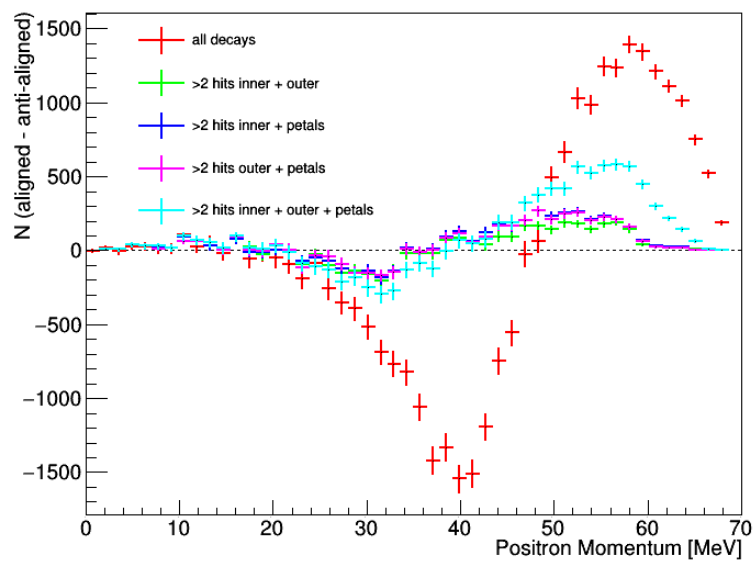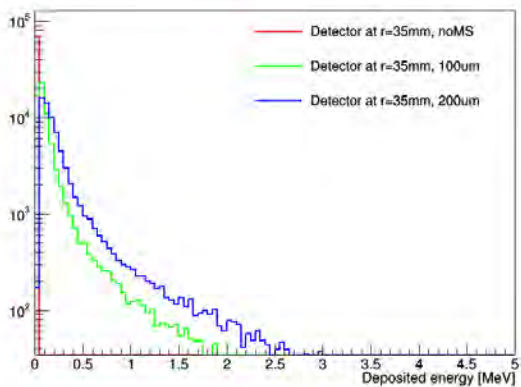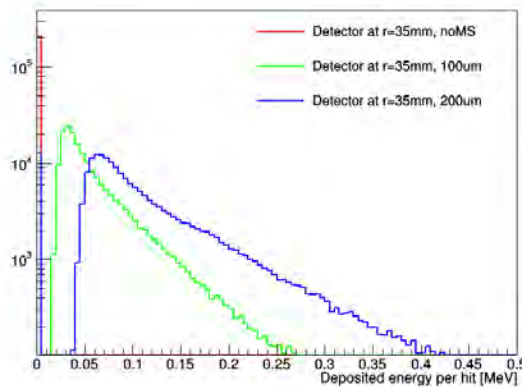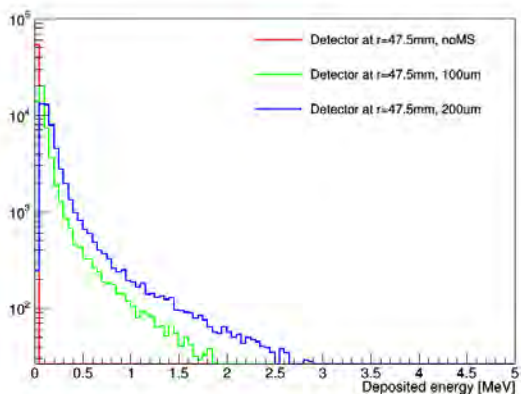


Figure 38: The sensitivity to an AMM measurement for different tracker configurations. The inner and outer layers refer to the original design and the petals are the additional layers.
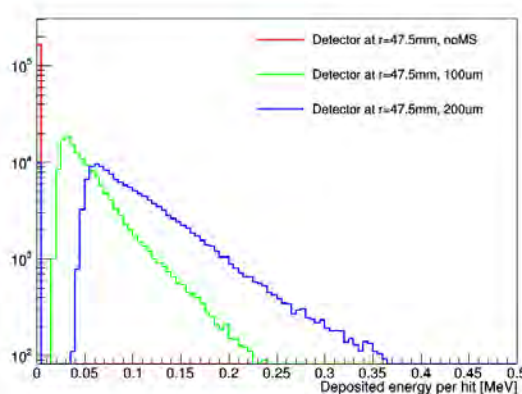
(a) Detector 1



(b) Per hit in Detector 1



(c) Detector 2



(d) Per hit in Detector 2

Figure 39: Deposited energy in each detector, for different detector thicknesses.
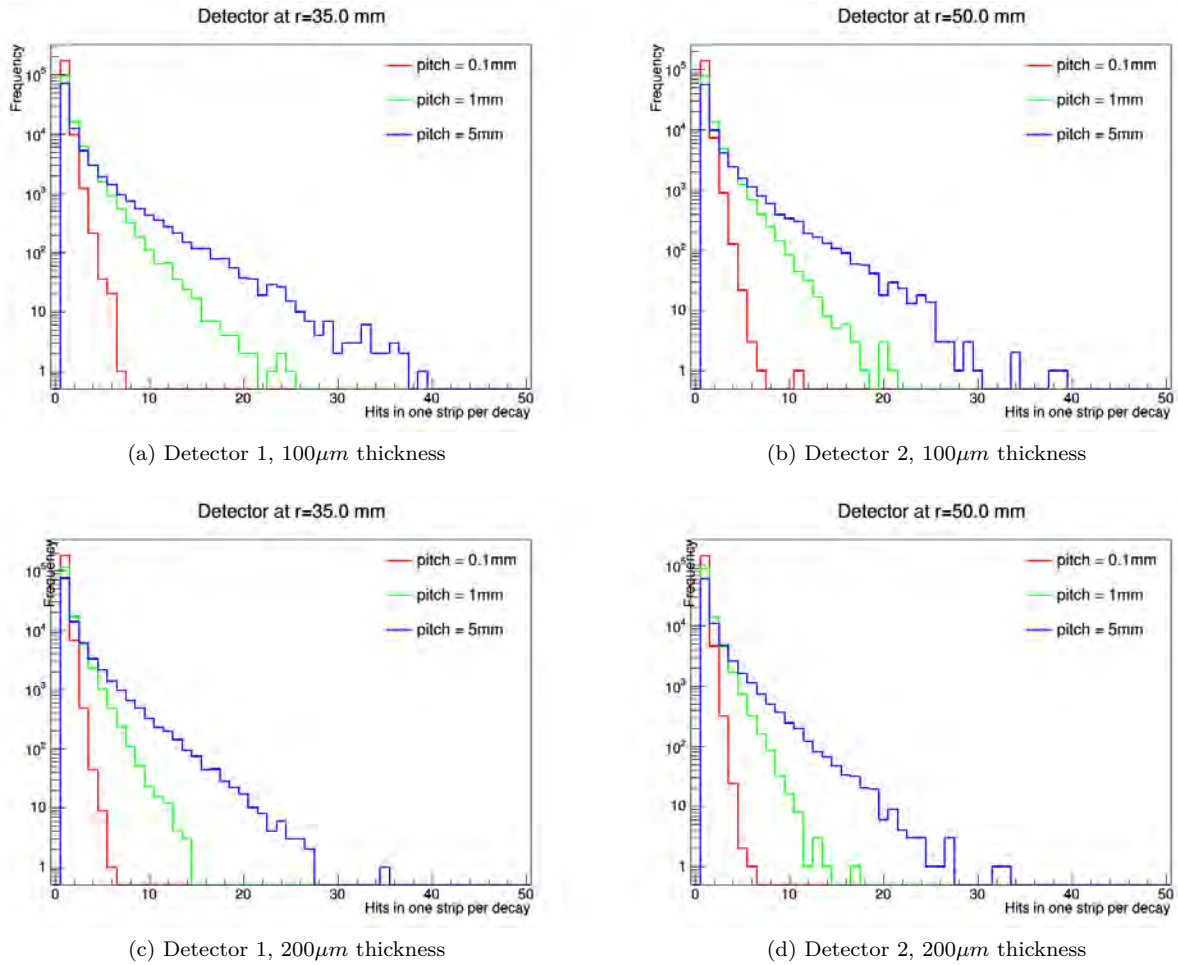
(a) Detector 1, $100\mu m$ thickness

(b) Detector 2, $100\mu m$ thickness

(c) Detector 1, $200\mu m$ thickness

(d) Detector 2, $200\mu m$ thickness

Figure 40: Hit multiplicity in a single strip for 3 different pitches. Each detector is made of Silicon with the quoted thickness.

### 4. Energy Loss due to multiple scattering

The typical energy loss for 2 different silicon detector thicknesses are shown in figure 39. Each detector hit causes an average loss in energy of approximately 50 keV per 100 µm of silicon.

### 5. Strip detectors vs Straws

The detectors in the simulation are assumed to have no longitudinal sensitivity, as they are there to measure AMM, which is longitudinally symmetric. They can be treated as either silicon strip detectors, or straw tube detectors, with the strip and straws running longitudinally. The timing resolution for silicon strip detectors of limited thickness is typically 2 ns, whereas for straw detectors it is 60 ns. The orbit time for a positron is 1 ns, so a hit in the same strip will be difficult to distinguish, and impossible for a straw detector. The number of multiple hits in the same strip, for different pitches is shown in Figures 40. Additional material helps reduce the number of same strip hits due to multiple scattering. Even with the additional scattering from silicon, the large pitch of a straw detector, which typically have a diameter of 5 mm, means that too many hits in the same straw are observed.

### 6. The SciFi detector

In this section, we describe a detector based on thin scintillating fibers of 250 µm size coupled to silicon photomultipliers (SiPMs) that addresses the position and timing requirements for the minimum ionizing
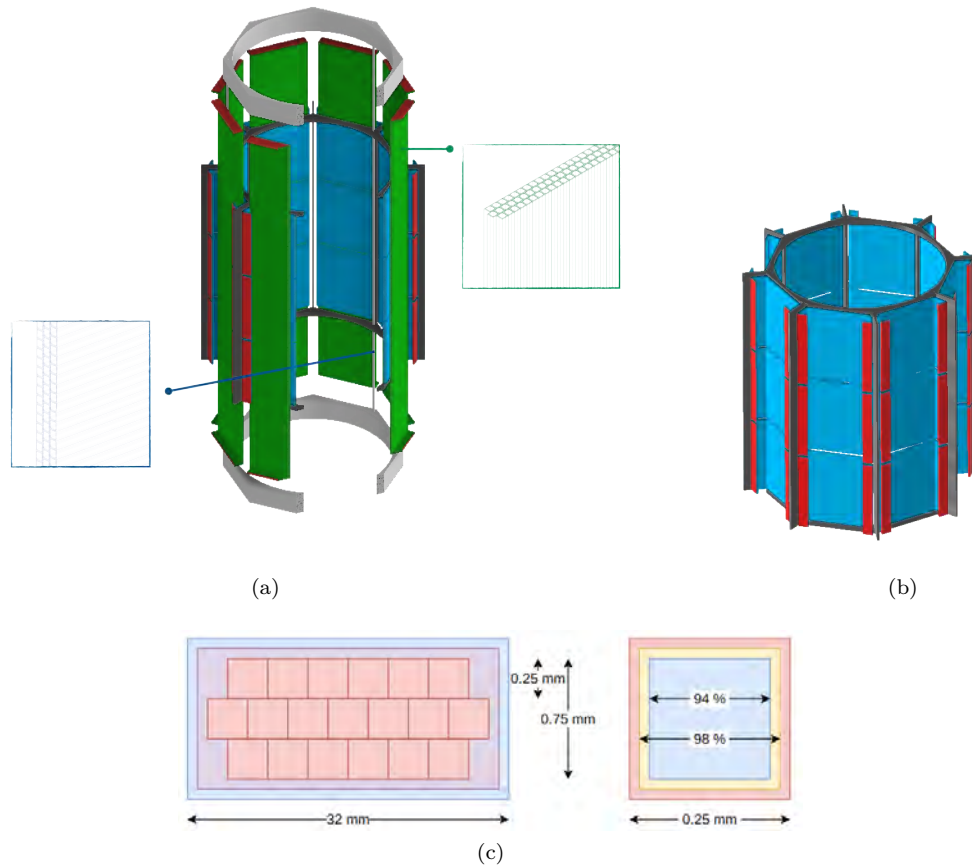
Figure 41: (a) Sketch of the SciFi conceptual design. (b) The inner part is made of three barrels of scintillating fiber ribbons. Each barrel constitutes eight ribbons, with the fibers oriented transversely. This is the so-called SciFi transverse detector (blue). The outer part is made of eight ribbons, with the fibers oriented longitudinally. This is the so-called SciFi longitudinal detector (green). (c) Left: A sketch of the layout of the fibers inside a SciFi ribbon. Right: A sketch of a fiber that comprises a *core* and two *claddings* of PMMA.

particles (mip) as outlined above. This detector option allows for a fast, versatile, modular, and low-cost detector technology usable in magnetic fields and vacuum, the environment in which the muon EDM measurement takes place.

The SciFi detector is designed to provide excellent tracking capacities for mip with a detector thickness below $0.4\%$, a timing resolution better than $1\,\mathrm{ns}$, and a spatial resolution of $1\,\mathrm{mm}$, or probably better. Figure 41 shows a first conceptual design of the detector. The tracker will be a compact detector made of several ribbons of $250\,\mu\mathrm{m}$ scintillating fibers arranged in an inner (transverse) and an outer (longitudinal) detector.

The inner detector is made of a minimum of three barrels, extendable to five, of scintillating fiber ribbons. Each barrel is made of eight ribbons, with the fibers oriented transversely. This is the so-called SciFi transverse detector, as shown in Fig. 41b, providing the necessary longitudinal resolution (up/down) to measure the EDM signal. In this detector, the fiber ribbons are polygonally shaped as shown by the blue elements in the figure. The red elements represent the photosensors. The optional outer detector is made of eight ribbons, with the fibers oriented longitudinally. Here, the ribbons have a parallelepipedal shape (green elements) with photosensors at both ends (red elements), as shown in Fig. 41. This is the SciFi longitudinal detector, which could complement the silicon strip detector discussed in the previous sections. Both detectors are arranged to cover a cylindrical surface, with the radius of the inner detector currently equal to $50\,\mathrm{mm}$.

Each ribbon has three layers of fibers and these three layers are glued together in a staggered way, as sketched in Figure 41c. Each layer is made of 128 $250\,\mu\mathrm{m}$ square or round multiclad fibers. One layer has a width of about $32\,\mathrm{mm}$ and a length of approximately $200\,\mathrm{mm}$. Each ribbon is read out at both ends by silicon photomultiplier, SiPM, arrays. The double readout of each ribbon is essential for matching the experiment requirements. The amount of energy deposited in such a thin fiber by a mip is small ($\mathcal{O}(35\,\mathrm{keV})$) and, given the size of the detector, the relative light reaching the photosensor turns out to be equal to a
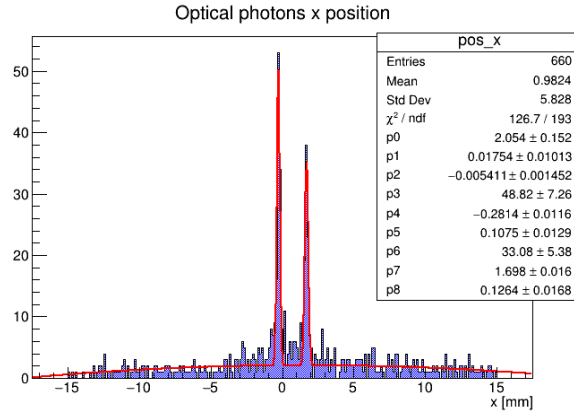
Figure 42: Two particles impinging 2 mm apart on the same ribbon. Using 250 μm fibers and having no pixelation on the readout, the spatial resolution is $\sigma \approx 100$ μm (p5 and p8). This value was obtained with a fit to *plo2+gaus+gaus* and with a bin width of 125 μm (half a fiber width).

few photons/fiber. To successfully collect these few photons with maximum efficiency and high dark noise rejecting factor, a double readout scheme is foreseen, as well as extreme care in the coupling of the fibers to the photosensors.

### a. Geant4 simulation and performance

We have developed a GEANT4 [58] simulation to study different detector design choices.

For the current simulations, the fiber implementation is based on doubleclad BCF20 Saint-Gobain scintillating fiber parameters[8]. The sketches of the fiber section and the ribbon are shown in Fig. 41c Currently, we are performing simulations that include the interaction between radiation and matter using GEANT4 physics processes. The photosensor readout and electronics will be implemented once all details of the detector are finalized. For these simulations, we assume an ideal readout scenario in which all photons that reach the ends of the fibers are detected, and the exact position and timing of each photon are recorded. Additionally, each fiber is treated as a single detector element equivalent to a single fiber readout.

We are considering the possibility of merging multiple fibers into a single photosensor to reduce the number of channels required for the Data Acquisition System (DAQ) of the experiment. However, the performance of the resulting system may be compromised by the balance between the desired resolution and the number of available DAQ channels, as well as by the pixelation of the SiPMs. Despite this, initial results from tests with a prototype ribbon using a fiber merging readout scheme under realistic conditions (including photosensor response, front-end electronics, and noise) show promising potential to meet the muon EDM requirements, as described in Sec. VII G 6 c. These results were obtained by using waveform analysis to extract the necessary information from the digitized data.

The expected performance of a single fiber ribbon for both position and timing resolution, where each 250 μm fiber is read out independently, has been assessed by dedicated studies.

The first step is to study the characteristics and performance of a single ribbon. Having two impinging particles at the same time at a given distance, we can estimate the spatial resolution of this system. Figure 42 shows an event with two particles separated by 2 mm. Looking at the position of the generated photons, we can clearly distinguish the two hits and the resolution is of the order of 0.1 mm.

In Fig. 43, the arrival time of the scintillating photons at the photosensor, generated by two consecutive particles, is shown. The position of the impinging particles is the same but a different $\Delta t$ was set between them. Although the time resolution on a single particle is given by the rising edge of the distribution, much sharper than the required ~ 1 ns, the distribution itself is quite broad. This means that a particle that crosses at the exact same position within ≲ 3 ns will induce a pile-up event. Note that here we neglect the shaping of the waveform, for which a width of 10 ns to 20 ns is expected. This is the time window within which a pile-up event could occur. The resulting distribution is still quite different from that of a single impinging particle, and this feature could be somewhat mitigated. On top of this, the probability of having no deflection due

─────────

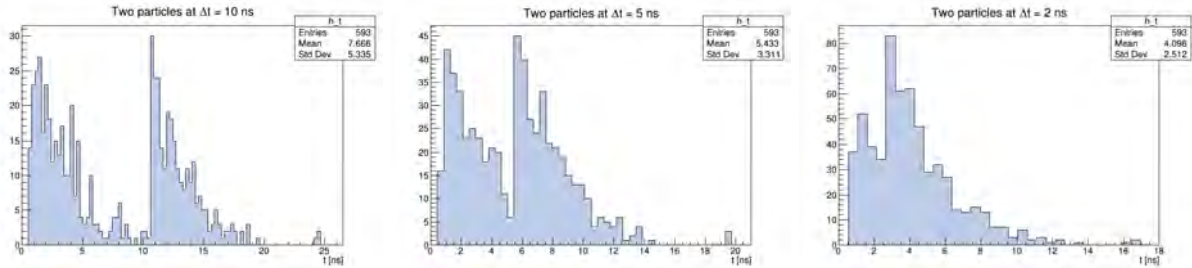[8] https://www.crystals.saint-gobain.com/radiation-detection-scintillators/fibers

Figure 43: In case of a particle impinging on the same position, the timing of the photon can be used to distinguish the two hits. For 20 cm fibers, the limit seems to be 3 ns to 5 ns.
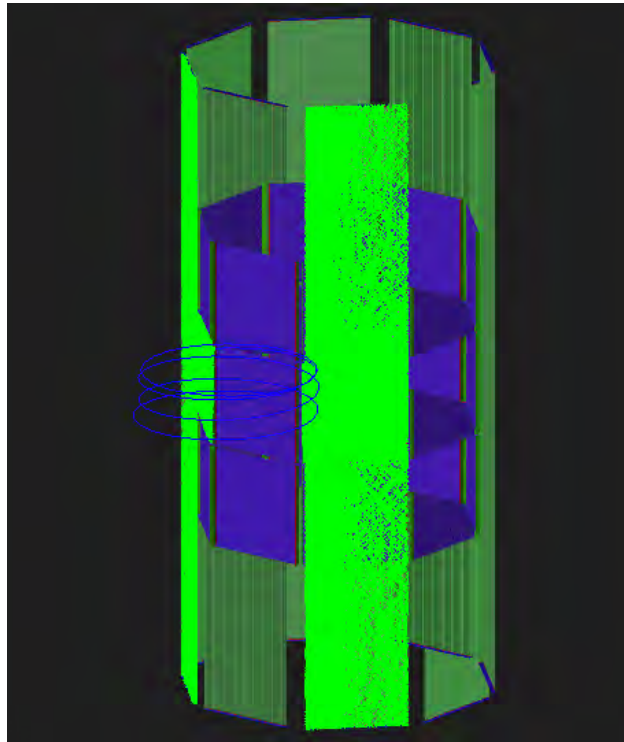


Figure 44: An example of GEANT4 simulated event. In green the optical photons reflecting inside the fiber ribbons; in blue the trajectory of the positron. Keeping the same colour scheme, the longitudinal SciFi is green while the transverse one is blue.

to multiple scattering on a full rotation is quite low: the spatial resolution will further mitigate this pile-up effect.

### b. MuEDM geometry

Simulating the full geometry of our detector, including both the inner layer of transverse fibers and the outer layer of longitudinal fibers, and incorporating the effects of the magnetic field, leads to more complex events. An example is shown in Fig. 44. In this scenario, a single particle can pass through multiple layers, undergoing scattering and losing energy. The spatial information provided by both layers, as shown in Fig. 45, demonstrates that the positions of the hits on the transverse plane are relatively stable, probably due to the low material budget. On the contrary, the inner layer provides information about the longitudinal movement of the particle.

The incorporation of timing information for the transverse fibers results in the plot shown in Fig. 46. This plot includes horizontal lines that represent the separation between different barrels. The relationship between transverse position and time provides additional information, although it can be more difficult to interpret. The resulting plots are shown in Fig. 47.
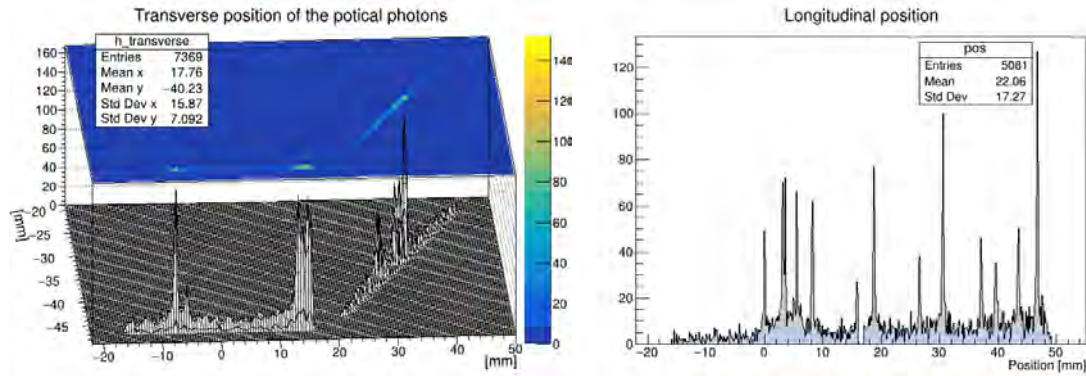
Figure 45: Looking at the position for the photons arriving at the readout for both SciFi layers.
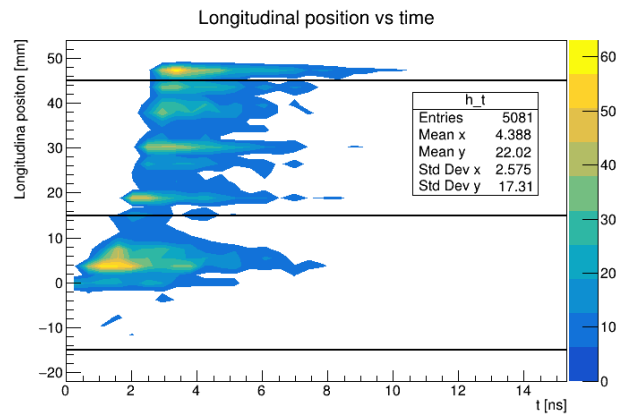


Figure 46: Looking at the relationship between time and longitudinal position for the inner layer makes it possible to see if the particle is spiraling up or down.

### c. *SciFi performance: A first ribbon prototype*

We summarize here the performance achieved with the so-called Large Prototype detector, which mimics a ribbon for muon EDM measurements.

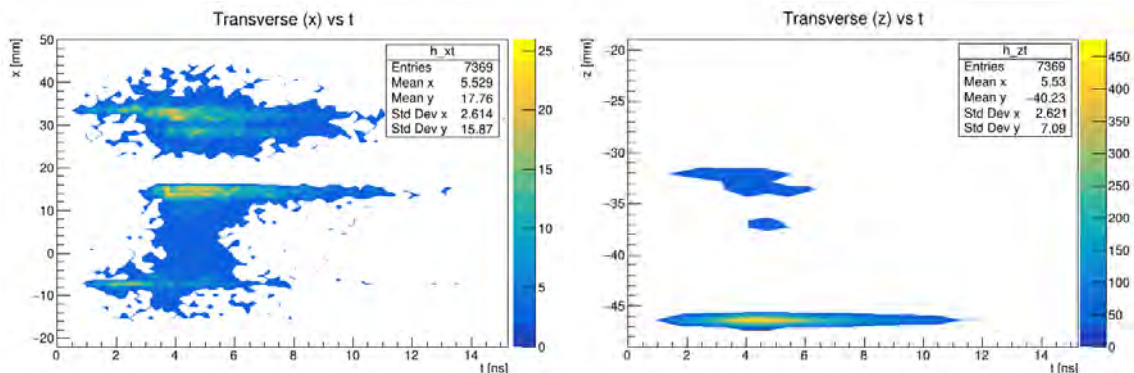The Large Prototype shown in Fig. 48, consists of 32 squared, 250 μm thin multiclad BCF-12 fibers



Figure 47: The information from the joint use of transverse position and time, given by the outer layer, is more complex but nonetheless essential (and a unique feature of this detector) in understanding the particle trajectory.
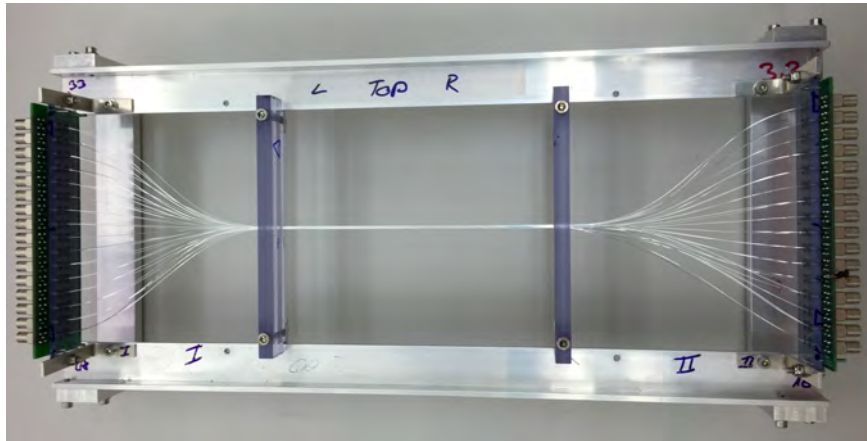
Figure 48: The Large Prototype, made of 32 squared, multiclad BCF-12 fibers of 250 µm thickness. Each individual fiber is coated with ~ 100 nm of aluminum and read out by a SiPM at each end.



| (a) | (b) |

Figure 49: Illustration of a column-wise readout of fiber tracker using SiPM arrays, rather than reading out every fiber individually. Fiber tracker (blue) coupled to a SiPM array (gray/b). Emulation of the column-wise read-out by SiPM arrays, combining offline the SiPM read out (b).

manufactured by Saint-Gobain[9]. The fibers were assembled to make four fiber layers; the first one was used as a trigger, and the others, staggered by half a fiber, were used as a detector. Each fiber was coated by physical vapor deposition with ~ 100 nm of aluminum along its whole length, with the aluminum acting as an optical insulator. The fiber ends were fixed on two plexiglass end plates (one for each side), which were polished with a diamond cutting blade and fixed to an aluminum support structure. Each fiber end was coupled with BC630 optical grease to a Hamamatsu 13360-1350CS SiPM (active area $1.3 \times 1.3$ mm$^2$, pixel size 50 µm, PDE 40 %[10] [72]), resulting in 64 channels. All SiPMs were biased at the same bias voltage ($\approx 55$ V). The signal was passed through a minicircuit MAR-6-based amplifier, working with a typical gain of 40 dB, and finally digitized with DRS V5 evaluation boards [73, 74] at a sampling speed of 5 GSPS. The results shown here are based on waveform analysis.

To emulate the situation in which the fiber tracker is read out column-wise by SiPM arrays (see Fig. 49a), rather than reading out every fiber individually, the information from fibers of three consecutive layers was combined at the software level, as shown in Fig. 49b.

The prototype was studied in both the laboratory with a $^{90}$Sr source (electrons with endpoint energy 2.28 MeV) housed in a plexiglass collimator and at PSI's πM1 beam line. Unless otherwise stated, the following results refer to measurements at the πM1 beamline when selecting minimum ionizing positrons and irradiating the fibers at approximately half the fiber length, perpendicularly to their central axes. The πM1 beam was tuned to positive polarity and to a momentum of 115 MeV/$c$.

The Large Prototype showed a uniform response (variations between fibers $\lesssim 10\%$, variations in time and different trigger conditions $\leq 5\%$) with the average number of photoelectrons (phe) (average of the histogram) being $4.6 \pm 0.3$ (stat) for the AND and $3.7 \pm 0.3$ (stat) for the OR configuration at a threshold of 0.5 phe, consistent with the expectations. A typical light spectrum is shown in Fig. 50.

---

[9] https://www.crystals.saint-gobain.com/radiation-detection-scintillators/fibers
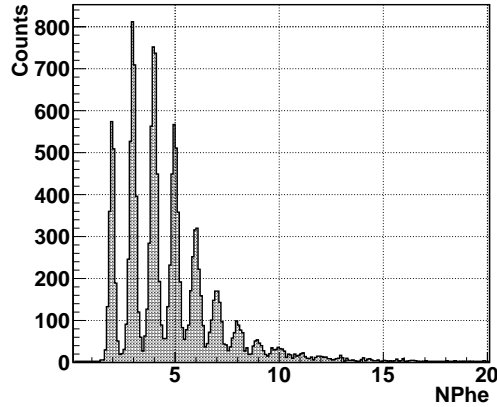[10] www.hamamatsu.com/us/en/product/category/3100/4004/4113/S12571-100C/index.html

Figure 50: Typical light spectrum (threshold 0.5 phe) measured by a single $250\,\mu$m square multiclad fiber ($\approx 50\,$cm length) read out by a SiPM on each end (SiPMs combined in logic AND) upon the passage of a mip.

| | Single layer | Double layer | Triple layer | Array |
|---|---|---|---|---|
| $\varepsilon_{AND}$ [%] (1.5 phe) | $34 \pm 1$ | $52 \pm 1$ | $67 \pm 1$ | $88.0 \pm 0.3$ |
| $\varepsilon_{OR}$ [%] (1.5 phe) | $79 \pm 1$ | $93 \pm 1$ | $97 \pm 1$ | $97.5 \pm 0.2$ |
| $\varepsilon_{AND}$ [%] (0.5 phe) | $72 \pm 1$ | $89 \pm 1$ | $95 \pm 2$ | $95.8 \pm 0.2$ |
| $\varepsilon_{OR}$ [%] (0.5 phe) | $96 \pm 1$ | $99 \pm 1$ | $98 \pm 1$ | $98.3 \pm 0.2$ |

Table V: mip detection efficiencies $\varepsilon_{\mathrm{AND}}$ and $\varepsilon_{\mathrm{OR}}$ measured by the large prototype when triggering at the indicated threshold (0.5 or 1.5 phe) on the respective SiPMs in the AND and OR logic. The errors are statistical.

The detection efficiency for both individual and multiple fibers combined was evaluated by using the first fiber layer (and, where appropriate, also preceding / successive fibers) as a trigger. The measured mip detection efficiency for the different logic configurations, thresholds, and layer numbers are summarized in Table V.

The time resolution on the mean time for a single fiber was determined considering the distribution $T_{single} = (t_1 - t_2)/2$, where $t_1$ and $t_2$ denote the time extracted from the SiPM at the left and right ends of the fiber, respectively. A typical distribution measured for a single fiber is shown in Fig.51.

When a particle hits more than just one fiber, the mean times of the individual fibers can be combined to obtain more precise timing information. Table VI summarizes the measured timing resolutions for different combinations of fibers, which correspond to potentially different thick ribbons, thresholds. The quoted sigma
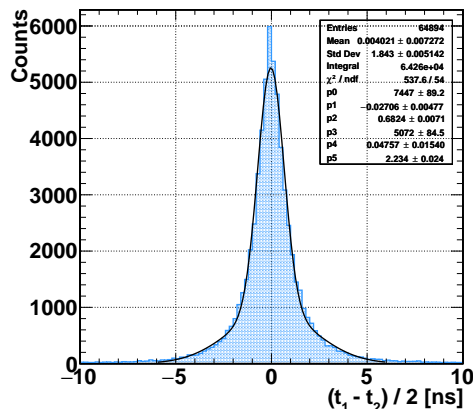


Figure 51: Timing distribution of a single fiber with a double Gaussian fit (solid line).

|  |  | Single | Double | Triple |
|---|---|---|---|---|
| $\sigma_t$ [ps] | (0.5 NPhe) | $1160 \pm 50$ | $830 \pm 3$ | $681 \pm 4$ |
| $\sigma_t$ [ps] | (1.5 NPhe) | $803 \pm 5$ | $600 \pm 5$ | $504 \pm 6$ |

Table VI: Timing resolutions measured by the Large Prototype when triggering at the indicated threshold on the respective SiPMs in the AND logic. The numbers are extracted from single Gaussian fits to the timing spectra. The errors are statistical.
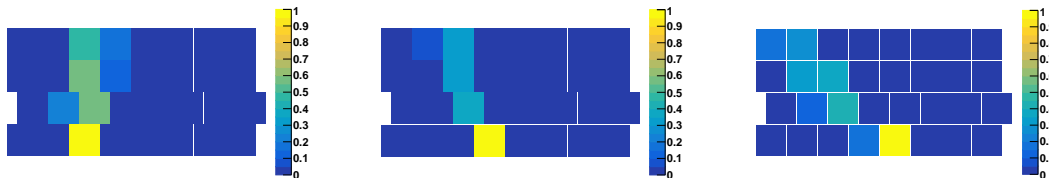


Figure 52: Particle tracks observed in the Large Prototype as a function of the inclination angle $\phi$. From left to right, the impinging angle is $\phi = 0°$, $\phi = 22°$, and $\phi = 60°$. The color scale indicates the number of events involving the corresponding fiber relative to the number of triggered events.

was obtained with a single Gaussian fit. A better resolution can be quoted using a double Gaussian fit, but is beyond the scope of this report. As shown by the measurements, with a ribbon made of three layers of fibers, a timing resolution of 500 ps can be achieved with a detection efficiency $\geq 90\%$.

Finally, Fig. 52 shows the tracking capability of the detector with real data. Positrons are impinging at different angles with respect to the plane of the ribbon prototype, and consequently, the fired fibers reproduce the particle path. To push the detector performance in this direction, each fiber was coated with a layer of 100 nm aluminum before assembling the prototype, reducing optical crosstalk between fibers from around 30% with naked fibers to $\leq 1\%$ with coated aluminum fibers.

The tracker technology and geometry illustrated above are a preliminary design, but already meet the requirements of positron tracking, i.e. millimeter and nanosecond resolutions. The interplay of a transverse SciFi detector and a silicon-based longitudinal detector seems to be a desirable choice. Working under this assumption, we envision the possibility of removing the longitudinal outer SciFi, which would be redundant, further reducing multiple scattering. Still, alternative geometries are being studied, for example the deployment of radial detectors on the outer part to better follow the positron tracks.

## VIII.   PLANNING AND SCHEDULE

### A.   Organizational structure

The collaboration is on its way to signing a "Framework collaboration agreement" (MoU in Fig. 53) between all participating institutions. Figure 53 displays the organizational chart of the collaboration top level.

The principal governing body is the "collaboration board" consisting of a representative of each collaboration member. It nominates and elects two co-spokespersons, at least one of them from PSI, managing the collaboration on a day-to-day basis, and representing it externally. The board proposes and reports its research program and progress to PSI's CHRISP research committee, and other governing bodies on demand. In addition, it designates task managers responsible for the implementation of the research and development strategy defined by the board.
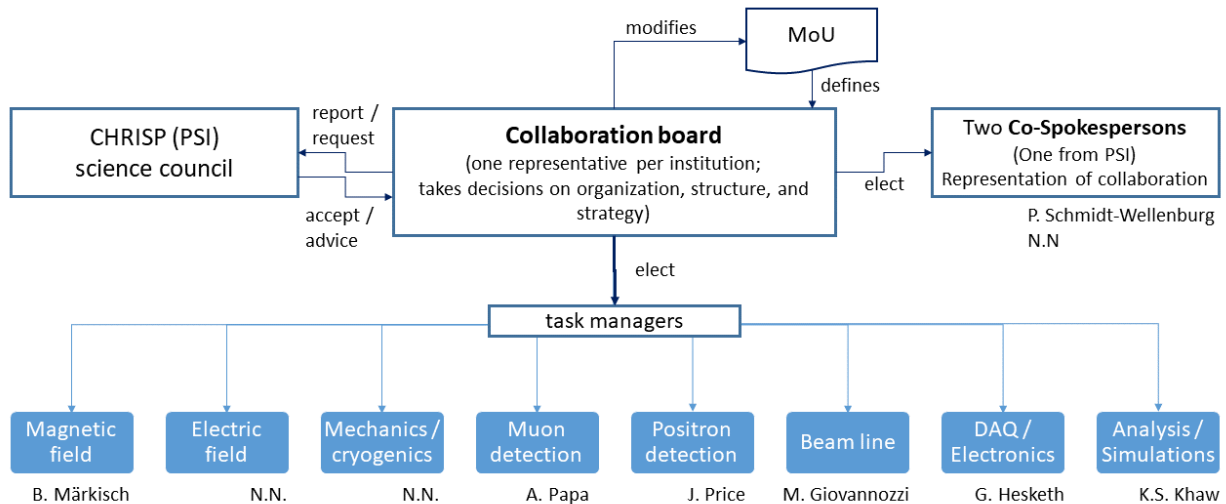
Figure 53: Organizational chart of the muEDM collaboration.

## B.   Tasks and planning phase 1

The proposed project, to set up and commission an apparatus to demonstrate the frozen-spin technique and search for a muon EDM with unprecedented sensitivity, is organized into a number of tasks:

**Magnetic field** The magnetic field is tightly connected to the injection and storage of muons inside the solenoid. The task covers all aspects of the magnetic field:

- magnetic-field mapping of the two existing solenoid magnets at PSI,
- calculation and optimization of field correction coils to adjust the magnetic field for best performance,
- design and construction of the pulsed field coil,
- specification, design, procurement of the pulse power supply.

**Electric field** The electric field is required to establish the frozen-spin condition and can be used to tune the $(g-2)$-frequency to measure the magnetic field and potential systematic effects. The task covers all aspects of the electric field:

- design, prototype tests, and construction of electrodes,
- specification, procurement, and tests of the vacuum feed through, and
- specification, design, procurement of the high-voltage power supply.

**Mechanics and cryogenics** The superconducting injection channel needs to be cooled to about $4.2\,\mathrm{K}$, further it needs to be heated to above the critical temperature, each time the main SC magnet is ramped. To change from clockwise to counterclockwise injection, the SC magnet has to be moved vertically by about $80\,\mathrm{mm}$. The task covers:

- design, procurement, and assembly of the cryostat,
- mounting structures and mechanical integration of all experimental devices,
- setup and maintenance of a CAD model of the experiment.

**Muon detection** At several positions along the muon injection trajectory, we will use scintillating detectors for detection and monitoring. The task covers all muon detectors:

- segmented muon entrance monitor for beam steering and monitoring of the incident flux;
- entrance detector at the exit of the injection tube,
- scintillating apertures to generate a trigger in anticoincidence with the entrance detector, when a muon is within the acceptance phase space for storage,
- end-detector to detect muons which cannot be stored and pass the central region of the solenoid,
- auxiliary scintillating detectors for beam diagnostics.

**Positron detection** All information on muon spin precession is imprinted on the ejected positron when the muon decays. The task covers all detectors to reconstruct positron tracks from decay:

- $(g-2)$ detector sensitive to decays that give access to the AMM frequency used to determine the mean magnetic field seen by muons and to adjust the electric field for the frozen-spin condition,
- EDM detector sensitive to decays which give access to the radial frequency indicating an electric dipole moment.

**Beam line** The secondary beam line $\pi$E1_2 serves many different experiments every year, possibly with very different requirements. This task comprises the optimization of the beam line for an injection into the experiments injection channel:

- Optimization of transverse phase space and flux, and minimization of the momentum bite for the existing beam line;
- design and procurement of additional magnets, i.e. horizontal dipole, for an optimum transport of muons from beam exit to injection tube entrance,
- investigation, and design of nonlinear beam elements to adjust beam phase space to acceptance phase space.

**DAQ and electronics** The DAQ and electronics task takes care that in each experimental step, demonstrating the ability to deploy the frozen-spin technique for a measurement of the muon EDM, all relevant data are correctly acquired and electronics meet PSI's laboratory standards of safety. The task covers:

- DAQ for muon detectors,
- DAQ for positron detectors,
- electronics to measure and adjust magnetic fields,
- electronics to control the high voltage supply,
- electronics to measure temperatures and control the cryostat,
- connection and interface to the beam line control system,
- and safe storage of all data in open data fit storage facilities.

**Analysis and Simulations** The analysis and simulation task encompasses a start-to-stop simulation of the experiment and the preparation of the analysis based on synthesized simulation data. The task covers:

- beam line simulation and transport calculations from proton target to exit of secondary beam line
- injection and storage simulations using Monte Carlo methods and surrogate models for design and parameter optimization,
- simulation of detector response using Monte Carlo methods to synthesize toy data to develop an automated and blinded analysis
- an automated and blinded analysis for the final data demonstrating the frozen-spin technique and searching for an EDM.

## C.   Long-term perspective including Phase-II

Already during Phase-I certain aspects of the Phase-II instrument will be studied using finite element methods, Monte Carlo physics simulations, and machine learning algorithms for optimization. Together with the gradual progress of Phase-I, we will converge to an instrument design by the end of 2026. Figure 55 shows a tentative long-term plan that includes both phases. The second phase instrument coupled to a muon beam with $p \geq 125\,\mathrm{Mev/c}$ will further increase the sensitivity by a factor 50.
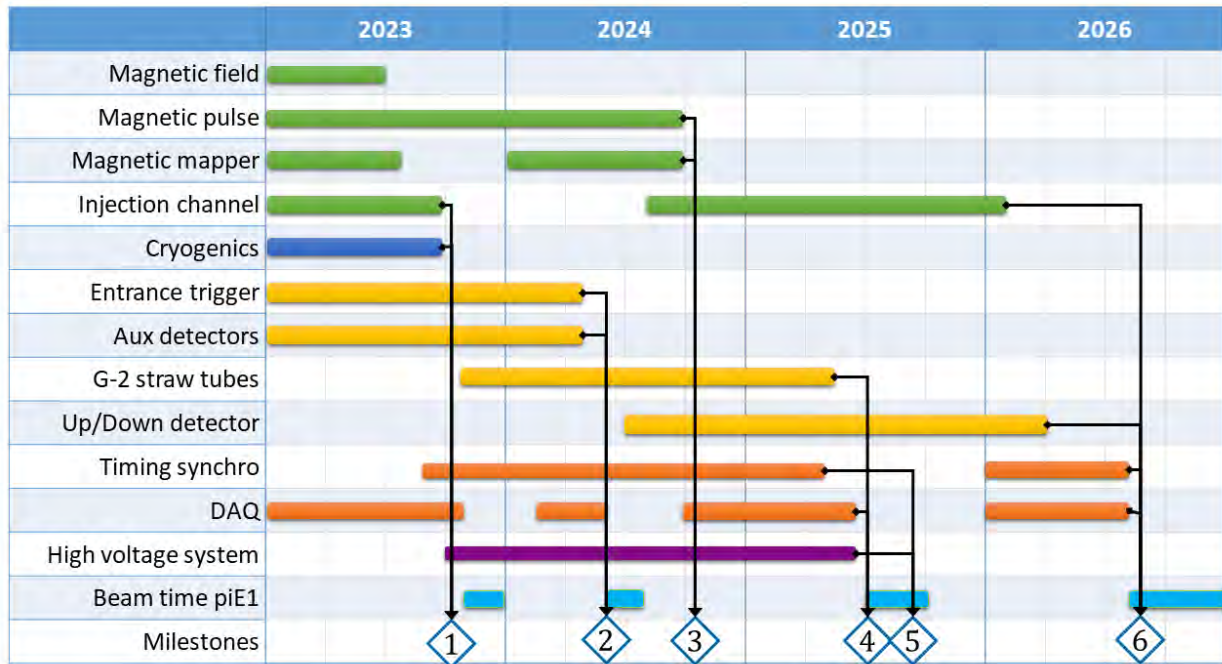
Figure 54: Schedule of top level tasks and milestones. (M1) Demonstration of off-axis injection, (M2) Muon selection and generation of trigger, (M3) application of pulsed magnetic field and measurement of eddy-currents, (M4) stopping of muons and detection of $(g-2)$-precession, (M5) adjust electric field by tuning $(g-2)$-precession to zero, and (M6) data-taking in muon EDM mode.
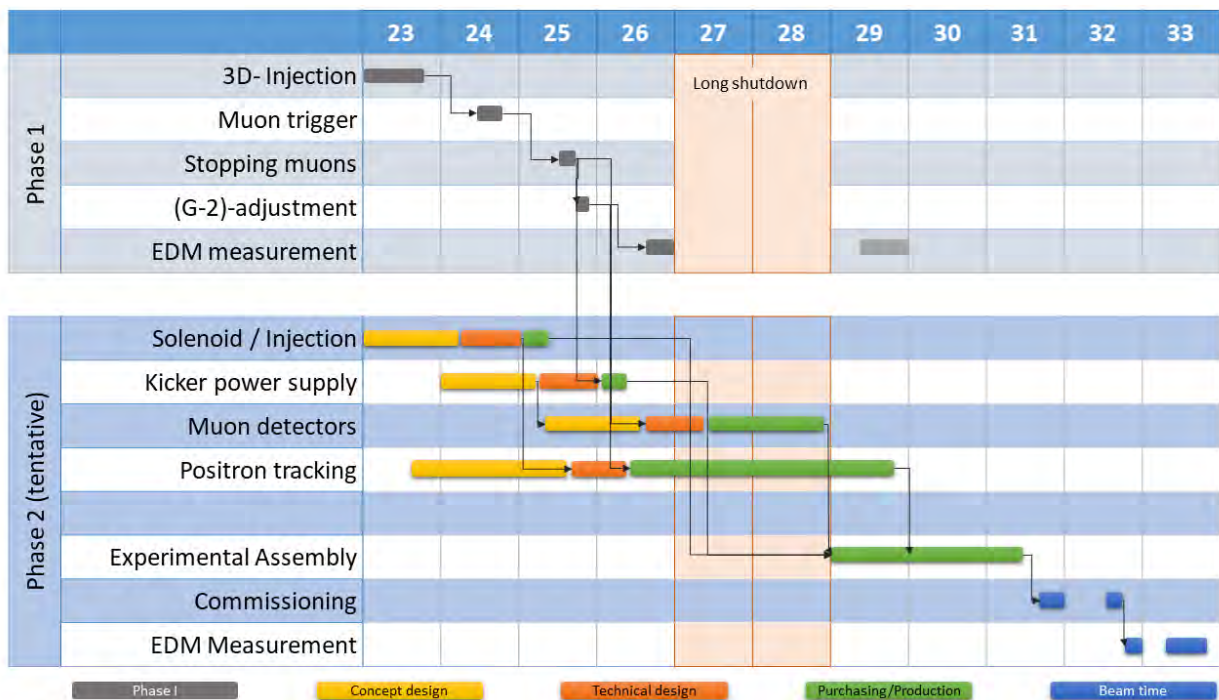


Figure 55: Long-term schedule. Phase-I is summarized in gray bars. Tasks of Phase-II are subdivided into three phases: conceptional design, technical design, purchasing and production. Once the instrument is assembled, we plan an engineering/commissioning run of 100 days, followed by a data production run of 200 days to accomplish a statistical sensitivity of better than $\sigma \leq 6 \times 10^{-23}\,e{\cdot}\mathrm{cm}$. Note that a data-taking run in 2029 after the long shutdown could be highly attractive to exploit the sensitivity of the Phase-I apparatus on a high intensity surface beam, e.g. $\pi$E5.

# IX.  REQUEST FOR BEAM AND TECHNICAL SUPPORT

## A.  Beam time requests

In the next years, until the long shutdown for IMPACT, the collaboration requests regular beam time on $\pi$E1 to demonstrate the feasibility of the experimental techniques necessary to accomplish a first measurement of the muon EDM using the frozen-spin technique in autumn 2026. According to our planning, we request beam time on $\pi$E1_2 in the following periods:

**2023** we will demonstrate the off-axis injection of a spiral beam into the solenoid. For this purpose we need one week of preparation of SC magnet and cryostat on the beam line and a second week for measurements.
**Duration:** 2 weeks.
**Period:** End of year, preferably in December.

**2024** we will demonstrate the selection of muons for storage by generating a trigger for the magnetic pulse by deploying the muon entrance detector.
**Duration:** 3 weeks.
**Period:** Start of HIPA in May.

**2025** we will demonstrate stopping and storage of muons in the central plane of the solenoid and measure the (g-2) frequency as a function of the electric field. For setting up the experiment, we estimate one week and three weeks of measurements.
**Duration:** 4 weeks.
**Period:** October - December.

**2026** we will freeze the spin and attempt a first measurement of the muon EDM at PSI. We estimate for the assembly of the experimental setup and full commissioning two weeks. Once we have successfully demonstrated the frozen-spin technique, we would like to take data with a sensitivity better than the current limit of $1.5 \times 10^{-19}\,e\cdot$cm and possibly better than $1 \times 10^{-20}\,e\cdot$cm, requiring at least three weeks without interruption. Note that using the same setup at a higher intensity beamline, e.g. piE5, could allow us to establish a new limit close to or below $1 \times 10^{-21}\,e\cdot$cm by 2026.
**Duration:** min 5 weeks.
**Period:** October - December.

## B.  Technical support

The collaboration has a strong participation of PSI, involving scientists from many different groups. In addition to these contributions to the experimental setup we request technical support from the "Hallendienst" and the "Beamline group" similar to that provided to other muon experiments, i.e. mu3e, MUSE, or MEG.

## X.   PHASE 2: GOING BEYOND $1 \times 10^{-21}\, e{\cdot}\mathrm{cm}$

The second phase of the search for a muon EDM at PSI requires the highest flux of polarized muons available at PSI, with a fairly high momentum, as the sensitivity scales with $\sqrt{N}$, $P_0$ and $\gamma$ from Eq. (16) with $E_{\mathrm{f}} \approx a_\mu B c \beta \gamma^2$. This favors the $\mu$E1 beamline at PSI as a potential beamline to host the experiment to achieve the highest sensitivity. Note that even higher momenta would result in higher values of the laboratory electric fields for a given magnetic field to deploy the frozen-spin condition. Therefore, an optimal beam momentum is in the range of $120\,\mathrm{MeV}/c$ to $150\,\mathrm{MeV}/c$. Preliminary studies of injection efficiency, based on a characterization of the $\mu$E1 beam line, see Sec. X A, show that from an initial muon flux of $1.2 \times 10^8\,\mathrm{s^{-1}}$ about $360 \times 10^3\,\mu^+/\mathrm{s}$ could be stored. Assuming that due to geometric and energetic acceptance only a quarter of the positrons can be detected, we derive a statistical sensitivity of better than $\sigma(d_\mu) \le 6 \times 10^{-23}\, e{\cdot}\mathrm{cm}$ for 200 days of data collection (see Table I).

### A.   Muons from the $\mu$E1 beamline

In 2019, we performed a characterization of the $\mu$E1 beamline to obtain essential input parameters for simulations towards the experiment as well as the injection study. We measured the muon beam rate, transverse phase space (emittance), and polarization level for several muon momenta from $65\,\mathrm{MeV}/c$ to $125\,\mathrm{MeV}/c$. Measurements at higher momentum were not possible, as it would have also increased the pion momentum, which resulted in the quenching of the long superconducting solenoid, $\mu$-channel in Fig. 56.

Figure 56 shows the layout of the $\mu$E1 beam line[11] at PSI: the pions produced at target E are extracted, selected in momentum by the dipole magnet ASX 81, and then transported through a 5 T superconducting solenoid, where muons are collected from the decays of the pions followed by a second selection of the momentum of the backward decaying muons performed by the dipole magnet ASK 81.

A scintillating fiber (SciFi) beam monitoring detector mounted $526\,\mathrm{mm}$ downstream of the quadrupole QSE83 (see Fig. 56), was used to measure the muon-beam rate and the transverse beam size. The transverse phase space was explored by employing a quadrupole-scan technique, which uses the quadratic relationship between the magnetic-field strength of the final focusing quadrupole in the beam line upstream of the beam monitoring detector and the transverse beam size to extract the phase-space parameters, namely Twiss parameters and emittance. Note that such a technique relies on the independent knowledge of the dispersion function for each strength value of the quadrupole used for the scan in order to disentangle the betatronic from the dispersive part of the measured beam size.

A maximum muon-beam rate of $1.05 \times 10^8\,\mu^+/\mathrm{s}$ at $2.2\,\mathrm{mA}$ proton current was obtained by the new setting of the transfer line, which also minimized the dispersion function at a beam momentum of $125\,\mathrm{MeV}/c$ as shown in Fig. 57a. Figure 58 presents the corresponding horizontal and vertical phase-space ellipses with emittances of $945\,\mathrm{mm{\cdot}mrad}$ and $716\,\mathrm{mm{\cdot}mrad}$ $(1\,\sigma)$, respectively, and Fig. 57b summarizes the horizontal and vertical emittances for two beam line settings as a function of the momentum of the muon beam.

Although we made sure, using TRANSPORT simulations, that for the new beam line setting the beam divergence is large and symmetric around the position 'FS81' and close to zero at the position of the beam monitor, this was not the case for the '$\mu$SR-tune' used for solid-state research. Hence, the Twiss parameters and emittance for the horizontal planes of the '$\mu$SR-tune' are not completely correct, as they still retain a dependence on the dispersion function.

This first characterization serves as a starting point to optimize the transfer beam line between the muon decay channel and the muon EDM experiment. If calculations and simulations indicate that an alternative beam layout would further increase the rate and better match the injection phase space, the modification of the beam line shown in Fig. 56 is in principle possible. This probably also requires a second test with the beam.

Polarization measurement was performed with a copper stopping target inside the existing $\mu$SR detector of the GPD instruments, and an example of the measured up-down counting asymmetry $A(t)$ at $125\,\mathrm{MeV}/c$ with the new tune is shown in Fig. 59:

$$A(t) = \frac{\alpha(N_\uparrow(t) - B_\uparrow) - (N_\downarrow(t) - B_\downarrow)}{\alpha(N_\uparrow(t) - B_\uparrow) + (N_\downarrow(t) - B_\downarrow)}, \tag{67}$$

where $\alpha$ accounts for the different detector efficiencies and solid angles, $N_\uparrow$ and $N_\downarrow$ are the number of positron
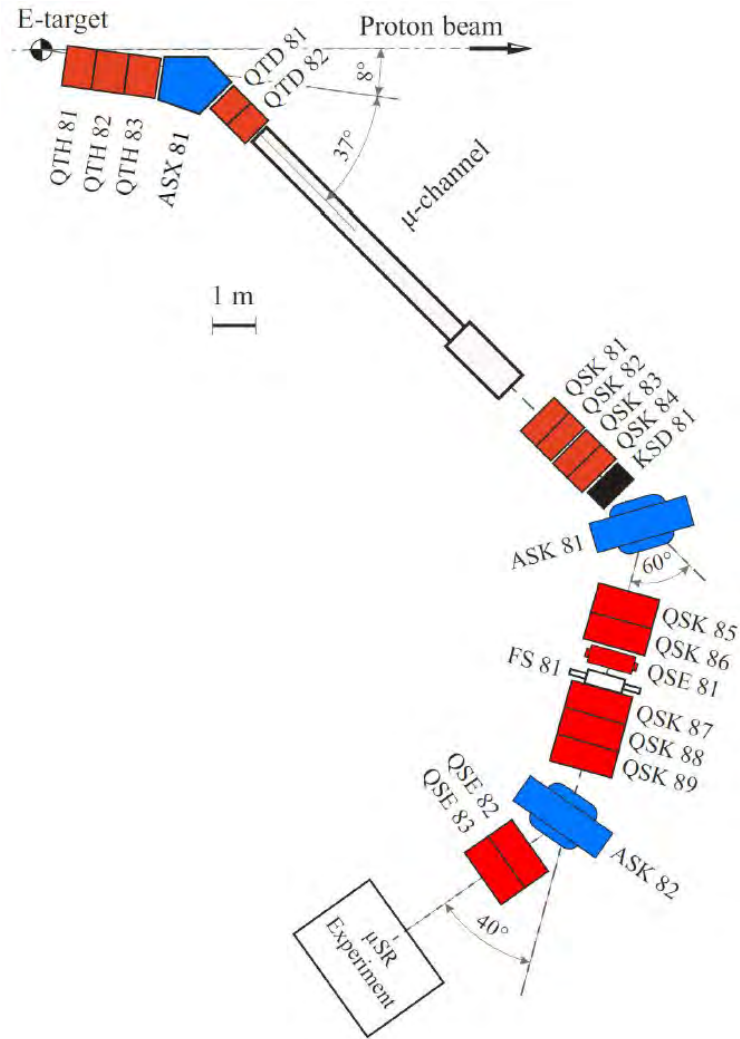
---

[11] https://www.psi.ch/en/smus/e1

Figure 56: Layout of the $\mu$E1 beam line.

counts in the up and down detectors, respectively, and $B_\uparrow$ and $B_\downarrow$ represent constant backgrounds in the corresponding detectors.

Since the oscillation amplitude of $A(t)$ is proportional to the initial muon-beam polarization, the comparison of the amplitude determined from the measurement and the GEANT4 simulation assuming 100% beam polarization results in an absolute value of the muon-beam polarization. The absolute muon-beam polarization at the $\mu$E1 beam line for both beam tunes as a function of the muon-beam momentum is summarized in Fig. 60 and confirms that the initial polarization is about 95.0(0.2)%.
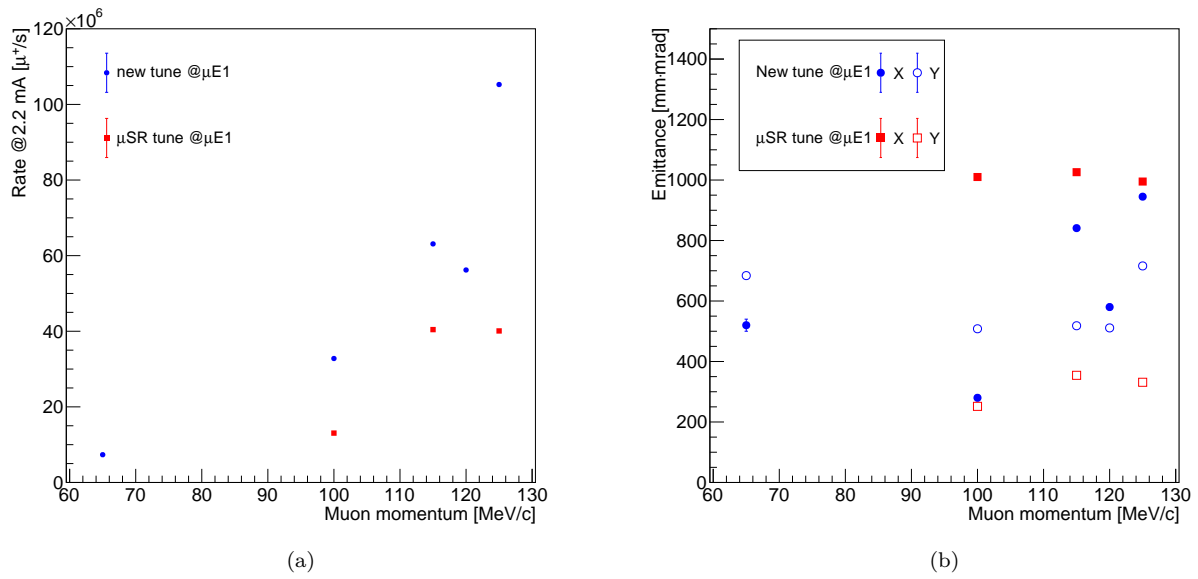
Figure 57: Muon-beam rate (a) and emittance (b) at the $\mu$E1 beam line for two beam line settings as a function of the muon-beam momentum.
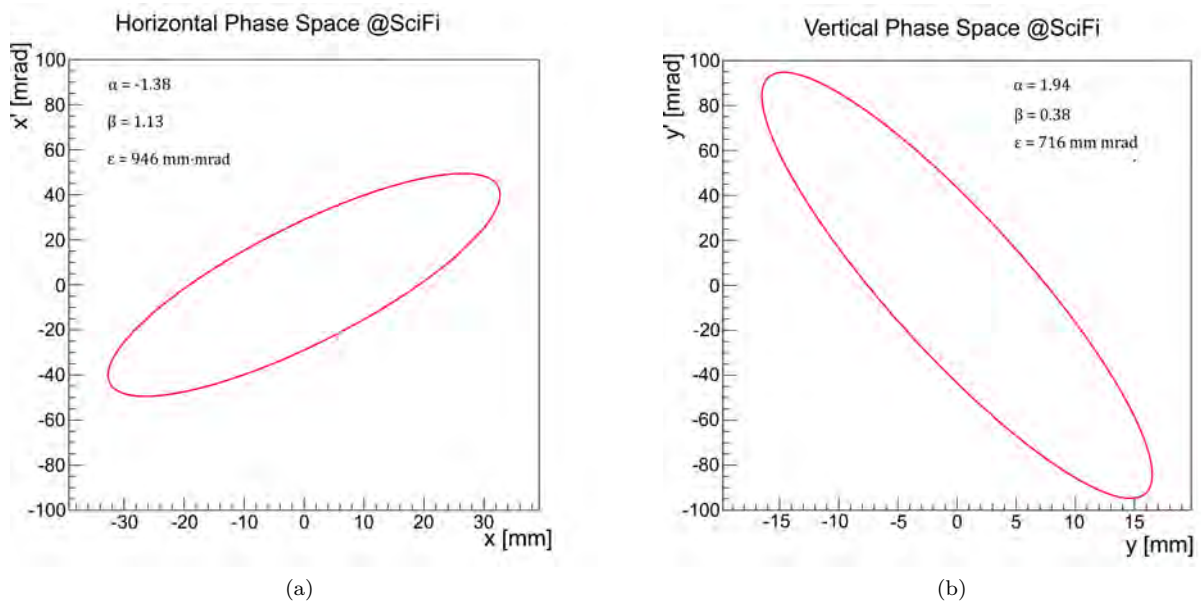


Figure 58: Horizontal (a) and vertical (b) $1\sigma$ phase space ellipses of 125 MeV/$c$ muon beam at the SciFi beam monitor position at the PSI $\mu$E1 beamline.

## B. The experiment of phase II

Going from a muon momentum of 28 MeV/$c$ to a momentum of 125 MeV/$c$ significantly increases the relativistic boost of the positrons and hence also the kinematic acceptance of the positrons. Most remarkable is the fact that at 125 MeV/$c$ most decay positrons have a momentum below the muon momentum and hence curl inward from the muon orbit. Figure 61 illustrates the two scenarios in a G4BEAMLINE simulation.

As in the precursor experiment, muons will enter the uniform 3 T magnetic field through a collimation injection channel inside a magnetic shield. The magnet coil package is arranged so that the magnetic field gradient between the injection zone and the storage zone is less than 3 mT/m resulting in a large acceptance phase space (see Fig. 23). Even at the high muon flux of $\mu$E1, on average, only one muon at a time will enter
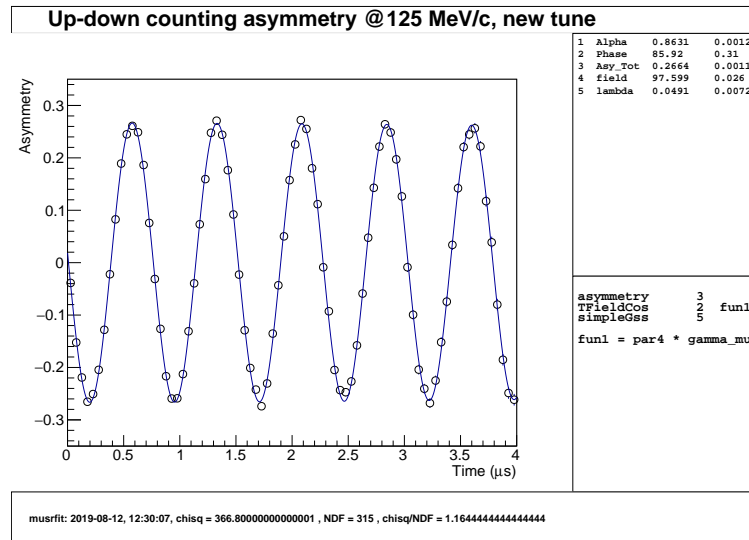
**Up-down counting asymmetry @125 MeV/c, new tune**

| | | | |
|---|---|---|---|
| 1 | Alpha | 0.8631 | 0.0012 |
| 2 | Phase | 85.92 | 0.31 |
| 3 | Asy_Tot | 0.2664 | 0.0011 |
| 4 | field | 97.599 | 0.026 |
| 5 | lambda | 0.0491 | 0.0072 |

```
asymmetry      3
TFieldCos      2   fun1
simpleGss      5

fun1 = par4 * gamma_mu
```

musrfit: 2019-08-12, 12:30:07, chisq = 366.80000000000001 , NDF = 315 , chisq/NDF = 1.1644444444444444

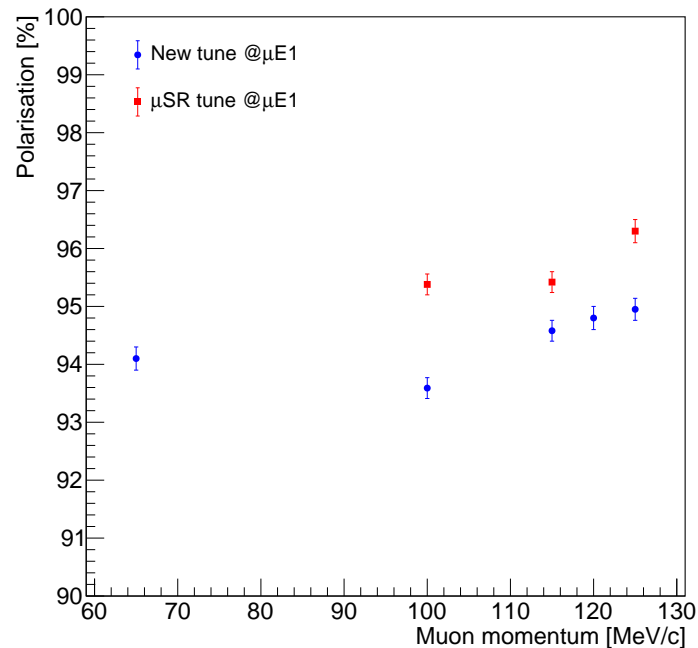Figure 59: Measured up-down counting asymmetry plot with the new tune at a momentum of the muon beam of 125 MeV/*c*.

Figure 60: Muon polarization of the $\mu$E1 beam line for two beam tunes as a function of the muon-beam momentum.

the spectrometer and spiral to the central area, where a triggered magnetic quadrupole pulse is applied. The muons will then be stored on an orbit with radius 139 mm (c.f. Fig. 61). The positron tracker made of silicon pixel sensors and fast scintillating fibers will be mounted inside the muon orbit, where most positrons can be detected.

As in the precursor experiment, we will use clockwise and counterclockwise injected muons to cancel the dominant systematic effects to first order (see Table II in Sec. VI).

Apart from a small magnetic-field gradient along the injection trajectory, the new magnet also needs a large bore diameter to accommodate the larger muon orbit of about 28 cm diameter. As the sensitive positron detection scheme and all necessary diagnostic sensors for the magnetic field will be mounted inside the muon orbit, we will ground the inner cylindrical electrode with a radius of about 13 cm, while the outer
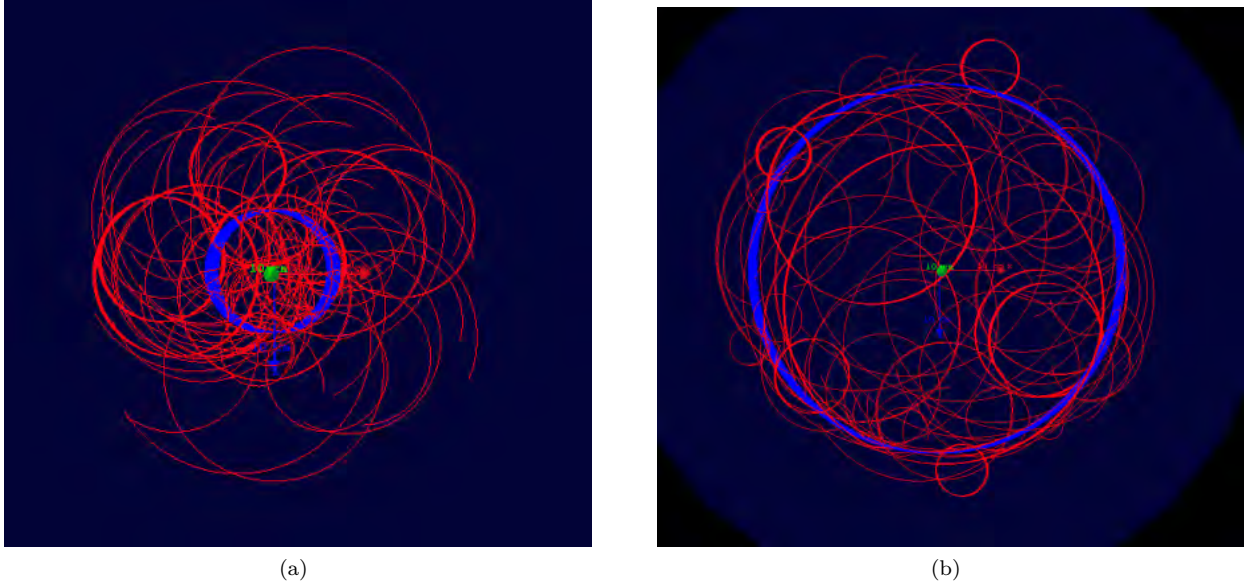
Figure 61: Plots from G4BEAMLINE simulations with muons in a 3 T uniform magnetic field, at (a) 28 MeV/$c$ and (b) 125 MeV/$c$ momenta, view along the solenoid axis. While in the low-momentum case most positrons tracks (red) have radii larger than the muon orbit (blue), $r = 31$ mm, in the high-momentum case the positron track radii are smaller than the muon orbit, $r = 139$ mm, and the positrons curl inward.

cylindrical electrode with about 15 cm will be charged to about 41 kV. These parameters require that the bore of the magnet has a diameter of at least 36 cm.

## XI.   ACKNOWLEDGMENTS

## Appendix A: Multiple scattering in thin conductive foils

The deployment of the frozen-spin technique requires the placement of coaxial electrodes proximate to the reference orbit of the muon. Subsequently, the electrode material intersects the volume transited by decay positrons within the kinematic acceptance (as defined by the muon orbit and bore diameter). Since an asymmetry in the emission direction of these positrons is the experimental signature for EDM-induced spin precession (and similarly for observation of that induced by the AMM), precise reconstruction of the positron trajectories is central to achieving the target sensitivities to $d_\mu$.

Along their spiral trajectories through the magnet bore, the positrons will undergo multiple scattering[12] as they repeatedly intersect the passive material of the electrodes (see Sec. VII F), as well as the material (both active and passive) of the positron detection scheme (see Sec. VII G).

It is important that simulations of the positron track reconstruction are able to accurately predict the impact of multiple scattering on the contrast of the asymmetry derived from the reconstructed emission directions. That is, some trajectories will be so perturbed by multiple scattering that the emission direction is incorrectly assigned, i.e. into the top rather than bottom hemisphere, or vice versa. Incorporating this reconstruction efficiency into the simulations ensures that the contribution of multiple scattering to the EDM sensitivity is estimated correctly to inform design choices and ultimately cross-check the experimental sensitivity.

The muEDM beamtime allocation in December 2021 facilitated the measurement of multiple scattering in various materials relevant for the design of the muEDM Experiment. The trajectory of positrons and muons passing through silicon and scintillating fibers, candidates for the positron detection scheme, were measured. Graphite and a polycarbonate film called Pokalon were measured as candidates for frozen-spin electrodes

| Momentum (MeV/$c$) | Graphite | Pokalon | Silicon | Mylar | SciFi |
|---|---|---|---|---|---|
| 50 ($e^+$) | 19 $\mu$m<br>46 $\mu$m | 16 $\mu$m | 50 $\mu$m | – | 3 layer<br>4 layer |
| 70 ($e^+$) | 19 $\mu$m<br>25 $\mu$m<br>46 $\mu$m | 16 $\mu$m | 50 $\mu$m | – | 3 layer<br>4 layer |
| 90 ($e^+$) | 19 $\mu$m<br>46 $\mu$m | 16 $\mu$m | 50 $\mu$m | – | – |
| 125 ($e^+, \mu^+, \pi^+$) | – | – | – | 25 $\mu$m<br>50 $\mu$m<br>75 $\mu$m<br>100 $\mu$m<br>125 $\mu$m<br>175 $\mu$m<br>250 $\mu$m | – |
| 135 ($e^+, \mu^+, \pi^+$) | – | – | – | 25 $\mu$m<br>50 $\mu$m<br>75 $\mu$m<br>100 $\mu$m<br>125 $\mu$m<br>175 $\mu$m | – |
| 140 ($e^+$) | 19 $\mu$m<br>46 $\mu$m | 16 $\mu$m | 50 $\mu$m | – | – |

Table VII: Summary of measurements conducted for various samples (horizontal) at various momenta and thicknesses (vertical). With the exception of the measurements for Mylar samples, a pure positron beam was used.

———

[12] For MeV positrons interacting in thin conductive foils, the leading effect with which we are concerned is multiple Coulomb scattering, scattering on the screened Coulomb potential of the constituent atomic nuclei (where the screening is due to the atomic electrons) [75].
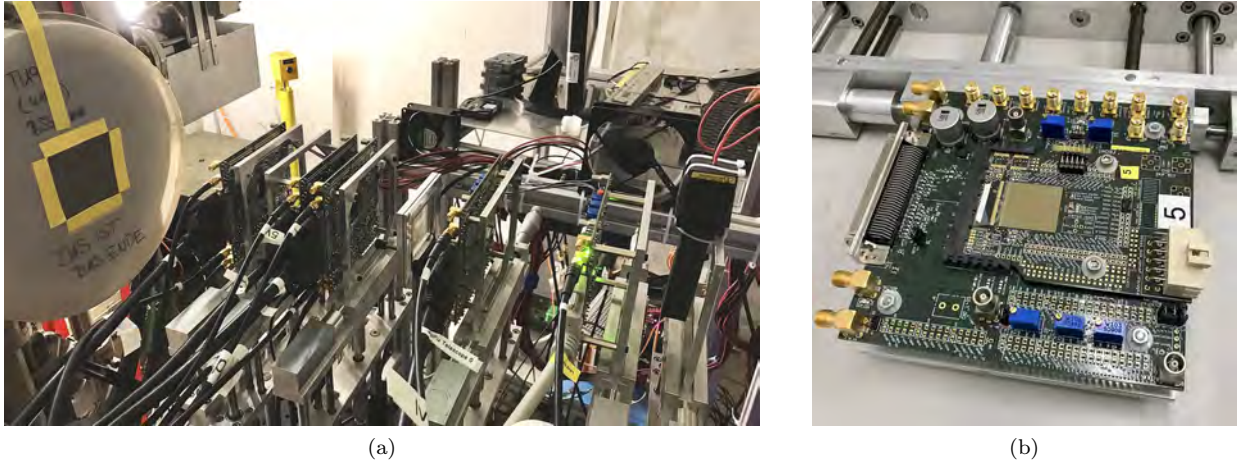
(a)             (b)

Figure 62: (a) A beam telescope set up composed of five (b) MuPix10 silicon pixel sensors was used to measure multiple scattering in thin foils mounted in an aluminium holder between the third and fourth sensors. A plastic scintillator downstream of the final sensor was aligned along the beam telescope to provide time of flight and energy loss, as well as providing an offline software trigger. The exit window of the $\pi$E1 beamline is visible at the left of the image in (a). The 20.00 mm × 20.48 mm silicon pixel matrix is visible at the center of the PCB in (b).

(see Sec. VII F). For muons, multiple scattering is relevant only in the design of the entrance detector (see Sec. VII D 4). Measurements of muons in Mylar were made for various thicknesses. The SciFi and Mylar measurements were also of interest to the MEG and mu3e Experiments at PSI. A complete summary of the measurements made for these materials at various momenta is provided in Table VII.

### 1. Experimental apparatus

The measurements were made using an array of silicon MuPix10 [76, 77] High Voltage Monolithic Active Pixel Sensors (HV-MAPS), an example of which is shown in Fig. 62b, arranged with three upstream and two downstream of the sample, to enable reconstruction of an upstream and a downstream track. This configuration is known as a beam telescope. The complete apparatus is shown in Figure 62a, where the placement of the sensors is identified by the five PCBs. The distance from the first sensor to the downstream edge of the sample holder is 192.5 mm and a further 155.8 mm to the last sensor. A plastic scintillator, visible on the right of the image in Fig. 62a, was also placed at the downstream end of the telescope for use as a data acquisition trigger with good timing resolution.

### 2. Analysis methods

If we could neglect multiple scattering in the beam telescope itself (comprising 100 μm silicon for all sensors with the exception of the one immediately downstream of the sample having a thickness of 50 μm), as well as the intervening air, then the tracks would reflect the incoming and outgoing directions from the scattering in the sample. However, this instrumental contribution from silicon and air is actually much larger than the scattering in the sample. Since in this case the angular resolution of the instrument is much larger than the scattering angle to be measured, the angle of multiple scattering cannot be reconstructed event-by-event. Instead, the distribution of multiple scattering must be extracted from the deconvolution of two distributions: one measured with the sample present, and one without to characterize the instrument response. Where this response function measured without sample is denoted $f_{\mathrm{tel}}(\theta)$, the sample distribution $f(\theta)$ can be deconvolved from the following expression for the total angular distribution of tracks measured with sample,

$$f_{\mathrm{meas}}(\theta) = f_{\mathrm{tel}} * f(\theta) = \int_{-\infty}^{\infty} d\alpha \, f_{\mathrm{tel}}(\alpha) f(\theta - \alpha) \tag{A1}$$
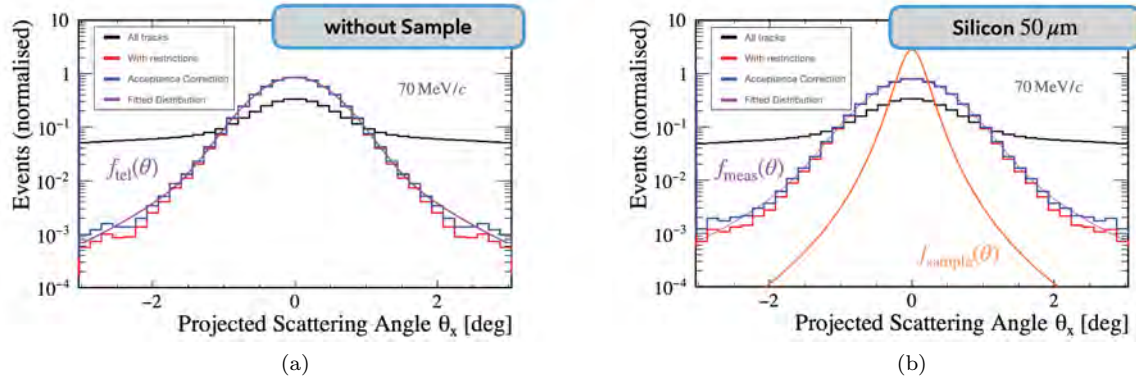
Figure 63: The angular distributions of the experimental data measured without sample (a) and with $50\,\mu m$ Si (b) are shown, along with fitted functions. The raw distribution (black) is restricted to tracks that meet criteria on the fit and intersection at the sample plane. A correction is applied to account for the geometric acceptance of the telescope. The orange curve in (b) shows the sample distribution extracted from deconvolution of the two fitted distributions.

for $\theta$ the parameter describing the scattering angle. The results presented here are parameterized, according to convention, by the projected angles giving the $x$ and $y$ components, denoted by $\theta_x$ and $\theta_y$, respectively.

An overview of the analysis workflow is shown by the angular distributions plotted in Figure 63. The plot in Figure 63(a) corresponds to the characterization measurement made without the sample, and in Figure 63(b) the measurement for the $50\,\mu m$ silicon sample. The raw distribution (black) is restricted (red) by requiring that the distance separating the intersection points of the upstream and downstream tracks from the sample plane should be separated by less than $1\,mm$. The distribution is corrected for the geometric acceptance of the telescope (blue), which is particularly relevant for such a measurement at low momentum. The corrected distributions were fitted with the sum of a Gaussian and Student's t distribution, and the sample distribution was extracted by deconvolution of the fit functions according to Eq. (A1).These histograms have been normalized so that each has an integral of 1, allowing the distributions to be interpreted as the observed probability density for a given scattering angle. Furthermore, under the assumption of spatial independence, the distributions shown are the sum of 720 rotations of the $x$-$y$ axes. Any variation in the position or width of the distribution over these rotations of the coordinate system can only be an artifact of the apparatus or analysis procedure. The symmetrization and suppression of statistical fluctuations resulting from this approach gave greater stability in the fitting algorithm, while the statistical uncertainty of the fit was derived to reflect the original counts. This procedure also enabled estimation of the systematic uncertainties by taking the relative fluctuation in the standard deviation of the distribution over all coordinate system rotations. From the extracted sample distributions, the RMS of the central 98% of the distribution ($RMS_{98}$) was determined and used as a metric for comparison with the model predictions.

### 3. Results & Model evaluation

The results for multiple scattering in silicon, graphite and Pokalon samples at $50\,MeV/c$ and $70\,MeV/c$ are presented in Fig. 64.

The $RMS_{98}$ values determined from the measurements are compared with the predictions of the Highland formula and GEANT4 . The graphite and Pokalon samples show relatively good agreement, validating both models within uncertainties. In both cases, GEANT4 offers a better prediction than the empirical estimate given by the Highland formula. However, the silicon samples are systematically overestimated by $\sim 3\sigma$ by GEANT4 , showing much better agreement with the Highland formula. Analysis of data collected at $50\,MeV/c$ is ongoing due to the loss of the sensor immediately upstream of the sample in some of these runs.

A Variational Autoencoder Hit Prediction Model has been developed to estimate the lost hits in this sensor by training on those runs in which it was active. Since the lost sensor was upstream of the sample, the model is independent of the sample present in the training data. Preliminary results are expected shortly for the analysis using these reconstructed hits.

The results of the Mylar measurements are in preparation, and the preliminary results indicate good agreement with the predictions of GEANT4 .

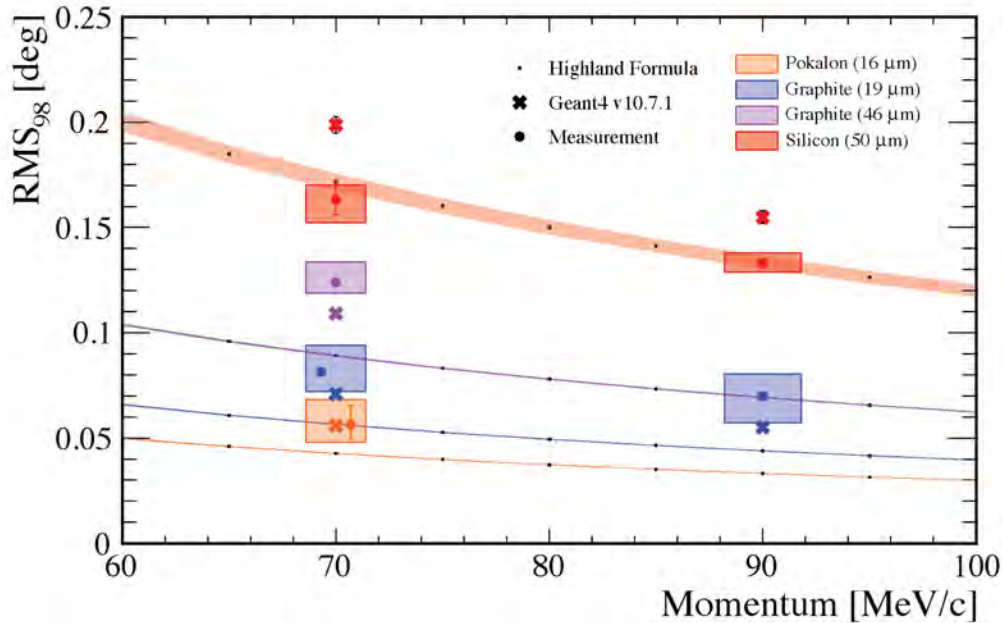Measurements taken for the 3-layer and 4-layer SciFi ribbons have enabled a determination of their thick-

Figure 64: Experimental results are shown by the RMS of the central 98% of the sample distributions extracted by deconvolution. Statistical uncertainty is shown by the error bars, and the total error by the shaded rectangles. The RMS$_{98}$ predicted by the Highland Formula and the GEANT4 Urbán model are also plotted, where the uncertainties on these points reflect the uncertainty in the determination of the sample thicknesses.

ness as a fraction of the radiation length $X/X_0$ by assuming the validity of the Highland formula, which predicts the mean scattering angle as a function of this thickness fraction, as well as the charge, mass and velocity of the incident particle. This information is an important input for simulations incorporating these SciFi ribbons developed for the mu3e experiment. A similar design is anticipated for the muEDM positron detection scheme (see Sec. VII G 6 c).

The direct empirical validation of the multiple scattering model in GEANT4 is a valuable reassurance as we advance further in the design of the muEDM Phase I experiment.

Preliminary design and prototyping will begin for the electrode system in 2023, so the multiple-scattering studies previously undertaken provide timely input to support the design choices that will be confirmed in the near future.

Simulation studies in GEANT4 are already well underway to inform the development of a positron detection scheme. The results for SciFi and silicon are informative in estimating the effects of multiple scattering on the resolution limits of the positron reconstruction. If GEANT4 overestimates the multiple scattering of positrons in silicon, as the measurements suggest, then the resolution obtained from the simulation should be a conservative upper limit. Once the final results are confirmed, further consideration will be made of alternative models for simulations. These measurements address multiple scattering of positrons at momenta much lower than existing measurements reported in the literature (e.g., [78, 79]). Many of the challenges encountered in the analysis have arisen from the reliance on the deconvolution method, which is essentially a very low signal-to-noise ratio. Although defined by the apparatus design, this is essentially unavoidable using such a beam telescope at these low momenta, partially explaining the gap in the literature. This work thus represents a significant contribution to the characterization of multiple scattering of positrons in materials relevant for precision experiments in low-energy particle physics.

### Appendix B: Test beam results for a minimal-mass, high-granularity time projection chamber

Tracking muons at $28 \, \text{MeV}/c$ in a TPC will require a very light gas mixture, to avoid MS and energy loss dominating the resolutions in the reconstruction of the trajectory. The lightest mixtures used in gaseous detectors are based on helium, with minority components such as hydrocarbons, fluorocarbons and $CO_2$, which are used to control the size of the avalanches produced in the electron multiplication structures and
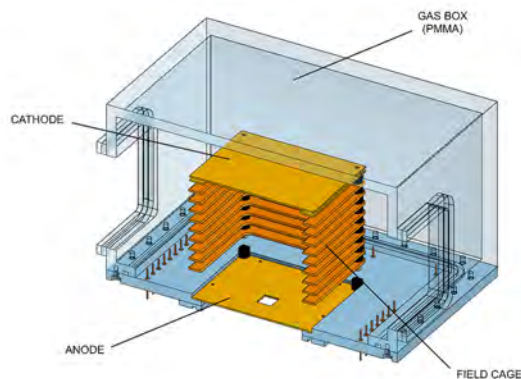
Figure 65: A schematic of the TPC prototype used for the characterization of the GridPix (section view).

avoid discharges.

As reported in Sec. VII B, for the measurement of the muon injection angle, we propose using a TPC readout using GridPix chips. Not much literature is available on GridPix operations with helium-based gas mixtures. So, in 2022 we performed two beam tests at PSI, operating a TPC instrumented with one GridPix chip in mixtures of helium-isobutane and helium-$CO_2$ mixtures at different concentrations.

A sketch of the TPC prototype used in these tests is shown in Fig. 65. A gas-tight acrylic box is filled with the desired gas mixture. Inside the box, a set of electrodes at different voltages defines a region of space (*drift region*) with a uniform electric field: a cathode plane (a PCB with a uniform copper layer) at high negative voltage, an anode plane (a plastic plate covered with copper tape) at a lower negative voltage, eight copper rings in between, spaced by 1 cm and with a voltage dropping linearly from the cathode to the anode. At the center of the anode plane, a 1.6 cm × 1.6 cm square window is cut, and a GridPix sensor is placed 0.8 mm below. With the GridPix readout plane at ground voltage and the GridPix mesh at about 400 V, the anode plate, the ring and cathode voltages are set accordingly to get the desired uniform field in the drift region. Fields from 300 V/cm to 700 V/cm have been explored.

The TPC was tested with beam in the $\pi$M1 and $\pi$E1 areas at PSI. In $\pi$M1, most of the measurements were performed with a 105 MeV/$c$ beam, mainly composed of positrons, while in $\pi$E1, surface muons (28 MeV/$c$) are used.

The $\pi$M1 test was performed in July 2022 with Helium:Isobutane gas mixtures, in 85:15, 90:10 and 95:5 concentrations. The test allowed one to characterize the response of the GridPix with such mixtures, a necessary step toward the development of the muon tracking devices, given the poor literature that is available for the GridPix with helium-based mixtures.

Figure 66 shows the relative efficiency of the GridPix sensor at different mesh voltages. The measurement was obtained by counting the average number of reconstructed ionization electrons along a track. At 470 V the GridPix becomes unstable for all mixtures. The 90:10 and 85:15 mixtures show a clear and wide efficiency plateau above 420 V, the 95:5 mixture requires higher voltages and can be operated at full efficiency only at 460 V. This counterintuitive trend (one could naively expect the efficiency to be lower when the isobutane concentration is higher) could be due to the Penning effect appearing when the isobutane concentration is higher.

The GridPix is also expected to lose efficiency when exposed to a high rate of ionization electrons because of some charge build-up in the mesh, reducing the effective amplification field. In Fig. 66 the efficiency drop as a function of the beam rate is also shown. The rate of particles going through the sensitive volume of the detector is approximately estimated by the counting rate of the coincidence of two scintillators, placed right before and after the TPC, and having a transverse dimension comparable to the GridPix chip. A clear but small drop of the efficiency is observed above a few kiloHertz.

The experimental setup also allowed one to measure some electron transport properties of the gas mixture. In Fig. 67 the observed electron drift velocity and electron diffusion are shown and compared with the results of simulations performed with the GARFIELD software.

In $\pi$E1, tests were performed in December 2022 using Helium:$CO_2$ mixtures. The data analysis is currently in progress. Considering some differences in the setup, measurements of efficiency plateaus and diffusion coefficients should be possible, along with an approximate measurement of the drift velocity.
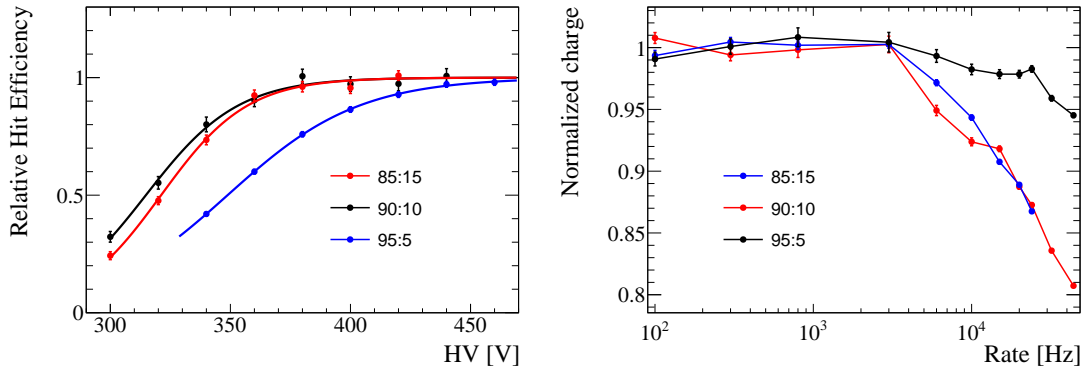
Figure 66: (Left) Efficiency of the GridPix hit reconstruction as a function of the mesh voltage, fitted with a sigmoid function and normalized to its maximum value. (Right) GridPix efficiency drop produced by the charge buildup in the mesh at high ionization rates. Efficiency is normalized to the average of the first three points. Three different Helium:Isobutane gas mixtures are considered.
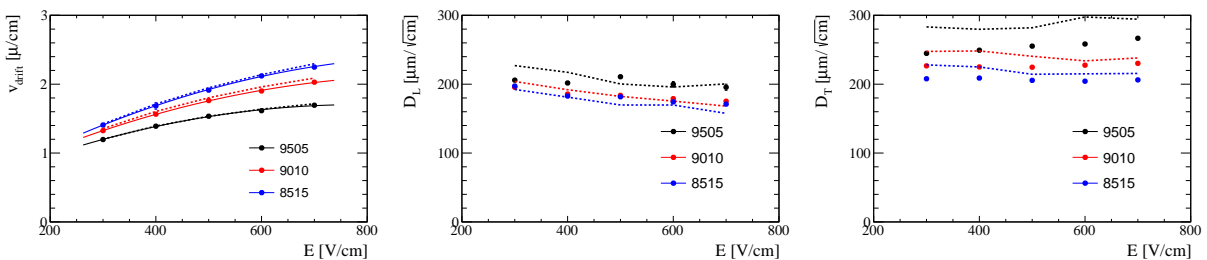


Figure 67: Electron drift velocity (left), longitudinal diffusion (center), and transverse diffusion (right) as a function of the drift field for three different Helium:Isobutane gas mixtures. The drift velocity is fitted with a second-order polynomial (continuous line). The results of GARFIELD simulations are shown with dashed lines.

## Appendix C: Test beam results for muon entrance trigger

As reported in Sec. VII D 4, a muon entrance trigger is required to select suitable trajectories and thereby produce a signal to activate the magnetic kick in the center of the solenoid for the muon storage. Prototypes of the entrance trigger were constructed using a set of plastic scintillators read out by SiPMs. These prototypes comprised a scintillating channel through which the muons pass after traversing an entrance detector. The core aim was therefore to test the efficiency of selecting muon trajectories using such a detector array in anti-coincidence. This approach prevents muons being perturbed by multiple scattering during their outgoing transit through the detector. We have successfully tested these prototypes in Nov-Dec 2022 at the $\pi$E1 beamline.

First, we tuned the $\pi$E1 beamline (see Fig. 12) to obtain muons with a momentum of $27.5\,\mathrm{MeV}/c$. A beam scanner consisting of a photomultiplier tube (PMT) and a $3\,\mathrm{mm}$ diameter pill-shaped scintillator (Pill Counter) on a movable table was set up (see Fig. 68) to facilitate tuning of the beam properties. Rate optimization at the desired focal point was used for preliminary tuning of the beamline elements and beam profile scans informed subsequent adjustments, particularly to the slits and dipoles, intended to symmetrize the beam profile. Two muon beam tunes (optimized in air) corresponding to focal points at two positions along the beamline ($z$-direction), the entrance focus ($z = 0\,\mathrm{mm}$) and exit focus ($z = 246\,\mathrm{mm}$), were chosen for use in data taking.

The transverse beam profiles at several positions between the entrance and exit focuses were also measured. Waveforms from the PMT were digitized using the DRS4 evaluation board. The trigger rate on the PMT was normalized to the rate of the proton beam current monitoring signal (frequency modulated at $10\,\mathrm{Hz}/\mu\mathrm{A}$), accessible in the experimental area. Transverse beam profiles at various $z$ positions were measured in steps of $1\,\mathrm{mm}$ along the $x$ and $y$ axes, as well as full matrix scans at the focal points themselves. Figure 69 and Fig. 70 show the extracted beam profiles for both beam tunes. The Twiss parameters can be extracted from the widths of the beam profiles (after correcting for broadening effects due to multiple scattering in the air) and will serve as the simulation input necessary for the evaluation of the performance of the entrance trigger
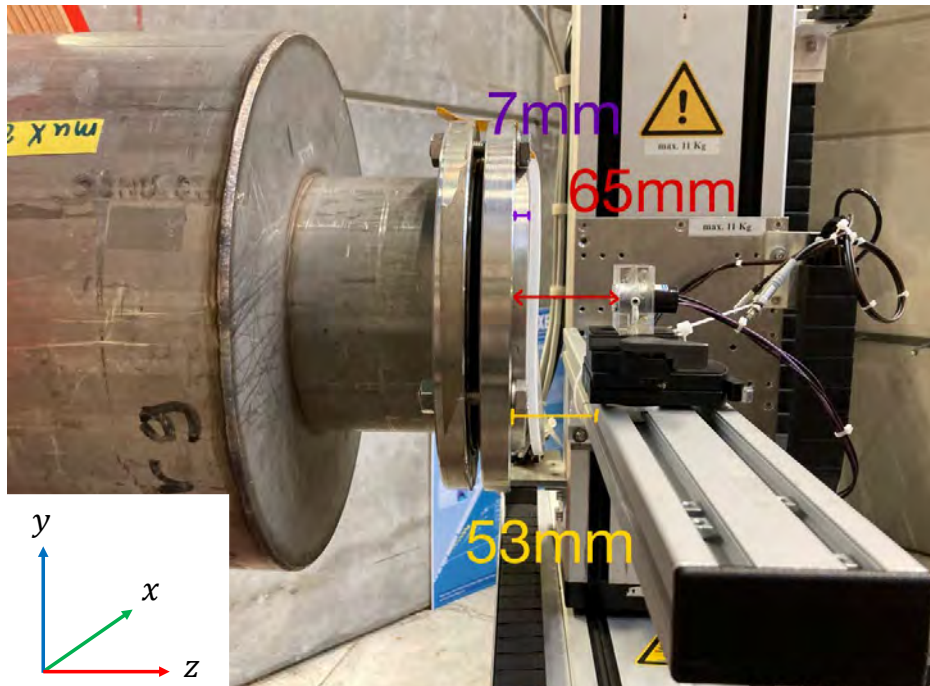
Figure 68: Setup of the beam scanner. The PMT on the plastic holder (the pill scintillator is covered at the front of the PMT and is not shown) is at the $z = 0$ position. The muon beam direction is taken as the $z-$direction. The last flange will be housing for the entrance detector's vacuum tube. Part of the last quadrupole magnet in the beamline is also shown.
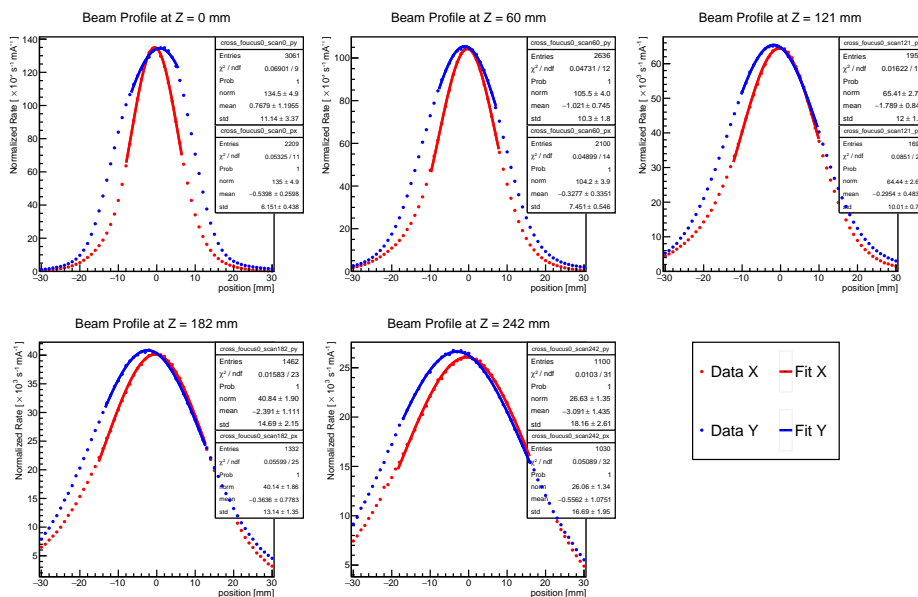


Figure 69: Fitted transverse beam profiles for the case of entrance ($z = 0$) focus. The trigger rate is normalized to the proton current.

during the test beam period.

During the test beam, a series of detectors were utilized for a better characterization of the performance of the entrance detector. In addition to the Pill Counter, a SiMon detector was installed at the end of the entrance detector to record the beam profile, as shown in Fig. 71. A veto detector made of plastic scintillator acting as a beam collimator was also installed. For the entrance detector, two variants (Shanghai and Pisa) with some common parts were developed for this test beam.

In Fig. 72 and Fig. 73, the Shanghai version is shown. It consists of a thin plastic scintillator (gate detector)
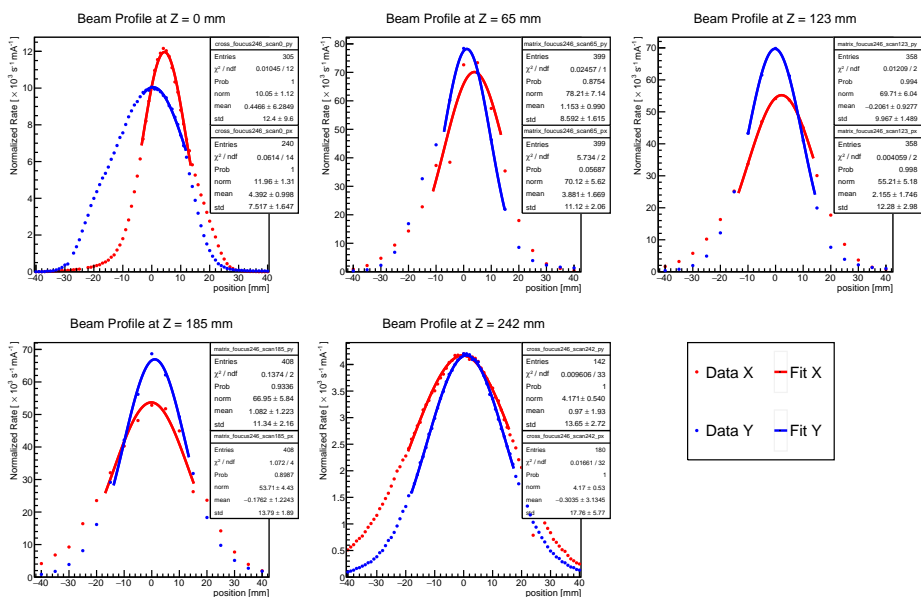
Figure 70: Fitted transverse beam profiles for the case of exit ($z$ = 246 mm) focus.
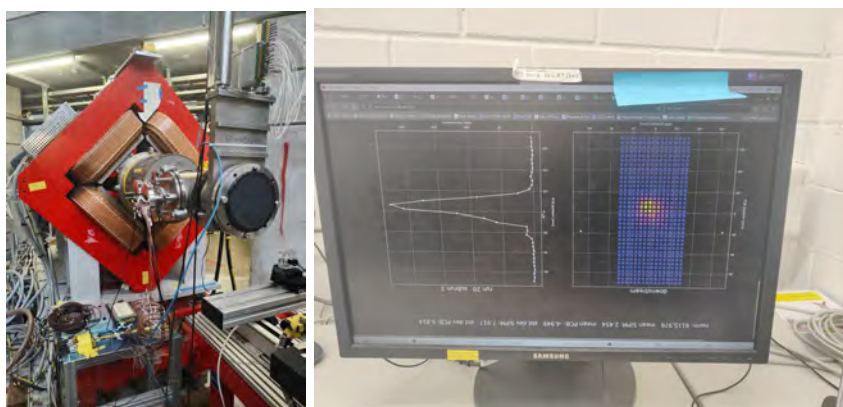


Figure 71: (Left) SiMon detector at the end of the beamline. (Right) A typical beam profile measured during the beam test.
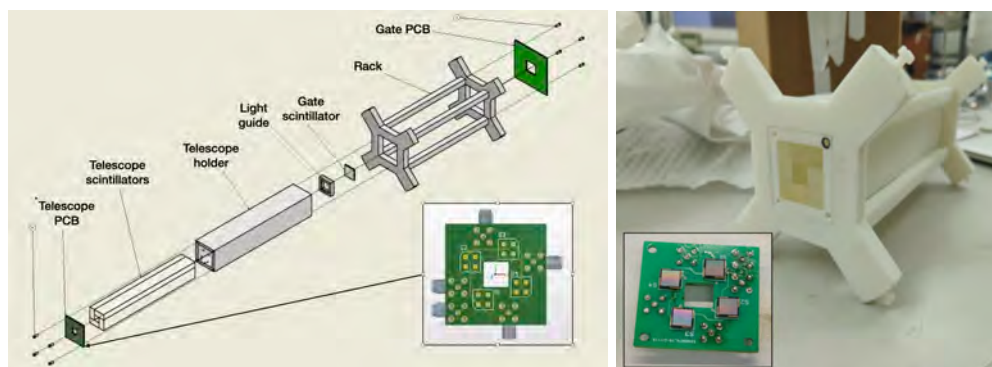


Figure 72: (Left) A 3D CAD drawing of the muon entrance detector. (Right) A prototype entrance detector developed for the test beam at PSI. Insets are SiPM read out boards for the telescope scintillators.
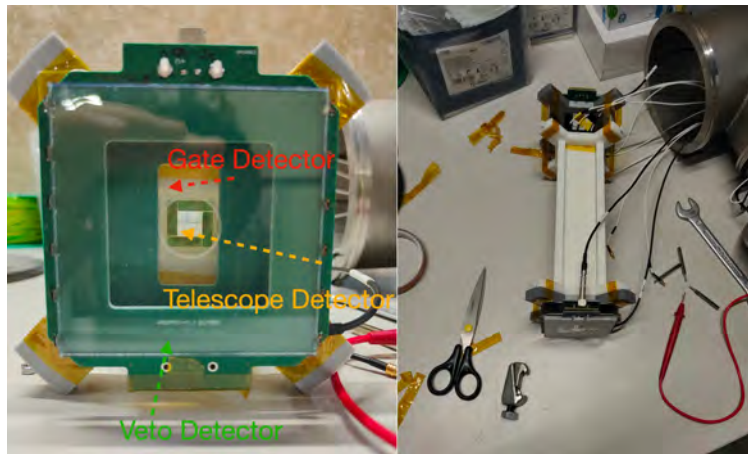
Figure 73: (Left) A muon beam view of the entrance trigger. (Right) A top view of the entrance trigger.

and four GNKD[13] plastic scintillating tiles with a cross-section of $20 \times 10\,\mathrm{mm}^2$ (telescope detectors), each read out by NDL[14] silicon photomultipliers NDL15-6060S. The NDL SiPMs were coupled to the scintillators using optical grease BC-603. The scintillators and readout electronics were held together by a 3D-printed holder and rack made of resin material. An exit detector, also consisting of plastic scintillator, similar to the gate detector was installed immediately downstream of the telescope detectors. Signal digitization of all the SiPMs was done using WaveDAQ based on DRS4. A typical muon event recorded during the test beam is shown in Fig. 74.
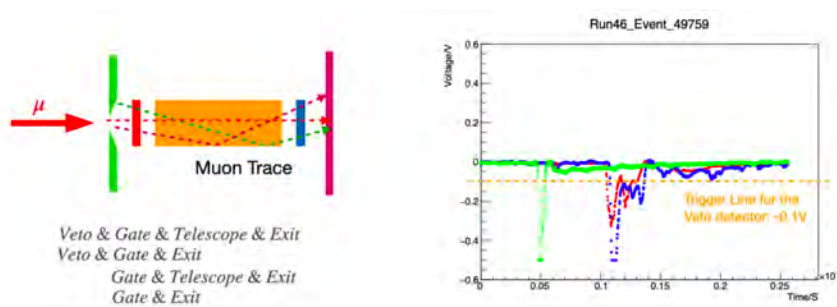


Figure 74: (Left) Classification of event types. (Right) A typical event recorded during the test beam. In this event, the muon hit the Veto (green), the Gate (red) and the Exit (blue) detectors.

The difference between the Shanghai and Pisa variants (see Fig. 75) is the telescope detector, which is based on four plastic scintillating tiles (two scintillating tiles with a cross-section of $30 \times 10\,\mathrm{mm}^2$, two with a cross-section of $10 \times 10\,\mathrm{mm}^2$), each read out by two Hamamatsu silicon photomultipliers. The SiPMs were coupled to the scintillator ends using optical grease BC-603.

---

[13] Beijing Gaoneng Kedi (GNKD) Technology Co. Ltd., http://www.gaonengkedi.com/pro.asp?classID1=28
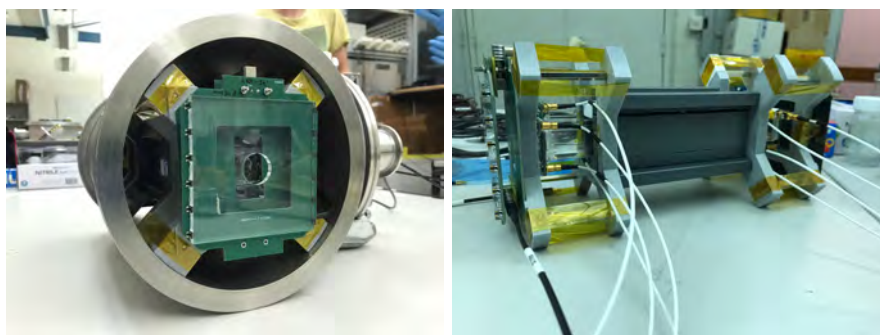[14] Novel Device Laboratory (NDL), http://www.ndl-sipm.net/indexeng.html

Figure 75: (Left) the entrance detector installed into the vacuum tube. (Right) A side view of the entrance trigger.

A total of 1.35 million events was collected during the test beam: 0.7 million muon events for the Shanghai detector and 0.65 million muon events for the Pisa detector. All the data falls into three categories: the gate detector in coincidence with the exit detector, only the gate detector trigger, and the gate detector in coincidence with the telescope detector. For each category, it falls into two different beam focuses: behind the gate detector (entrance focus), and behind the exit detector (exit focus). Initial analysis suggests that the entrance detector achieved its designed anti-coincidence function. Approximately 5% of selected muons are ideal events when only the gate detector is triggered, whereas 95% of selected muons are ideal events when the coincidence of the gate and exit detectors is used for selection. (Ideal event are defined as muons hitting the gate and exit detector, without hitting the veto and telescope detector, thus corresponding to a narrowly defined phase space of "straight tracks".) Events involving muon scattering on the inner surfaces of the telescope detector are also being studied. Different beam focus configurations result in a shift to these values. Data analysis for both detectors is ongoing, and a cross check between the Shanghai and Pisa detectors will be performed to characterize the efficiency of the muon entrance detector.

---

[1] M. Bartelmann, Rev. Mod. Phys. **82**, 331 (2010), 0906.5036.
[2] E. Komatsu et al. (WMAP Collaboration), Astr. Phys. J. S. **192**, 18 (2011), 1001.4538.
[3] A. D. Sakharov, JETP Lett. **5**, 24 (1967).
[4] D. E. Morrissey and M. J. Ramsey-Musolf, New J. Phys. **14**, 125003 (2012), 1206.2942.
[5] Lüders, G., Dan. Mat. Fys. Medd. **28**, 1 (1954), URL https://cds.cern.ch/record/1071765.
[6] F. J. M. Farley, K. Jungmann, J. P. Miller, W. M. Morse, Y. F. Orlov, B. L. Roberts, Y. K. Semertzidis, A. Silenko, and E. J. Stephenson, Phys. Rev. Lett. **93**, 052001 (2004), hep-ex/0307006.
[7] A. Adelmann, K. Kirch, C. J. G. Onderwater, and T. Schietinger, J. Phys. G **37**, 085001 (2010).
[8] G. W. Bennett, B. Bousquet, H. N. Brown, G. Bunce, R. M. Carey, P. Cushman, G. T. Danby, P. T. Debevec, M. Deile, H. Deng, et al. (Muon (g-2)), Phys. Rev. D **80**, 052008 (2009), 0811.1207, URL https://ui.adsabs.harvard.edu/abs/2009PhRvD..80e2008B.
[9] R. Chislett (Muon g-2), EPJ Web Conf. **118**, 01005 (2016).
[10] M. Abe, S. Bae, G. Beer, G. Bunce, H. Choi, S. Choi, M. Chung, W. da Silva, S. Eidelman, M. Finger, et al., Prog. Theo. Exp. Phys. **2019**, 053C02 (2019), 1901.03047, URL https://ui.adsabs.harvard.edu/abs/2019PTEP.2019e3C02A.
[11] E. Noether, Nachrichten von der Gesellschaft der Wissenschaften zu Göttingen, Mathematisch-Physikalische Klasse **1918**, 235 (1918).
[12] R. L. Garwin, L. M. Lederman, and M. Weinrich, Physical Review **105**, 1415 (1957), URL https://ui.adsabs.harvard.edu/abs/1957PhRv..105.1415G.
[13] C. S. Wu, E. Ambler, R. W. Hayward, D. D. Hoppes, and R. P. Hudson, Physical Review **105**, 1413 (1957), URL https://ui.adsabs.harvard.edu/abs/1957PhRv..105.1413W.
[14] J. H. Christenson, J. W. Cronin, V. L. Fitch, and R. Turlay, Phys. Rev. Lett. **13**, 138 (1964).
[15] M. Kobayashi and T. Maskawa, Prog. Theor. Phys. **49**, 652 (1973).
[16] C. Jarlskog, Phys. Rev. Lett. **55**, 1039 (1985).
[17] A. Hocker, H. Lacker, S. Laplace, and F. Le Diberder, AIP Conf. Proc. **618**, 27 (2002), hep-ph/0112295.
[18] M. Pospelov and A. Ritz, Phys. Rev. D **89**, 056006 (2014), 1311.5537.
[19] C.-Y. Seng, Phys. Rev. C **91**, 025502 (2015), 1411.1476.
[20] M. Raidal, A. Schaaf, I. Bigi, M. Mangano, Y. Semertzidis, S. Abel, S. Albino, S. Antusch, E. Arganda, B. Bajc, et al., Eur. Phys. J. C **57**, 13 (2008), 0801.1826.
[21] J. H. Smith, E. M. Purcell, and N. F. Ramsey, Phys. Rev. **108**, 120 (1957).
[22] D. Berley, R. L. Garwin, G. Gidal, and L. M. Lederman, Phys. Rev. Lett. **1**, 144 (1958).

[23] K. Jungmann, Ann. Phys. **525**, 550 (2013).

[24] T. E. Chupp, P. Fierlinger, M. J. Ramsey-Musolf, and J. T. Singh, Rev. Mod. Phys. **91**, 015001 (2019).

[25] J. N. Butler, arXiv e-prints arXiv:1709.03006 (2017), 1709.03006, URL `https://ui.adsabs.harvard.edu/abs/2017arXiv170903006B`.

[26] L. Masetti and A. Collaboration, Nuclear and Particle Physics Proceedings **303-305**, 43 (2018), URL `https://ui.adsabs.harvard.edu/abs/2018NPPP..303...43M`.

[27] A. Crivellin and M. Hoferichter, Science **374**, 1051 (2021), 2111.12739.

[28] A. Crivellin and J. Matias, in *1st Pan-African Astro-Particle and Collider Physics Workshop* (2022), 2204.12175.

[29] O. Fischer et al., Eur. Phys. J. C **82**, 665 (2022), 2109.06065.

[30] V. Cirigliano, B. Grinstein, G. Isidori, and M. B. Wise, Nuclear Physics B **728**, 121 (2005), hep-ph/0507001, URL `https://ui.adsabs.harvard.edu/abs/2005NuPhB.728..121C`.

[31] R. S. Chivukula, H. Georgi, and L. Randall, Nucl. Phys. B **292**, 93 (1987).

[32] L. J. Hall and L. Randall, Phys. Rev. Lett. **65**, 2939 (1990).

[33] A. J. Buras, P. Gambino, M. Gorbahn, S. Jager, and L. Silvestrini, Phys. Lett. B **500**, 161 (2001), hep-ph/0007085.

[34] G. D'Ambrosio, G. F. Giudice, G. Isidori, and A. Strumia, Nucl. Phys. B **645**, 155 (2002), hep-ph/0207036.

[35] V. Andreev, D. Ang, D. DeMille, J. Doyle, G. Gabrielse, J. Haefner, N. Hutzler, Z. Lasner, C. Meisenhelder, B. O'Leary, et al., Nature **562**, 355 (2018).

[36] T. S. Roussy, L. Caldwell, T. Wright, W. B. Cairncross, Y. Shagam, K. B. Ng, N. Schlossberger, S. Y. Park, A. Wang, J. Ye, et al., *A new bound on the electron's electric dipole moment* (2022), URL `https://arxiv.org/abs/2212.11841`.

[37] B. Abi, T. Albahri, S. Al-Kilani, D. Allspach, L. P. Alonzi, A. Anastasi, A. Anisenkov, F. Azfar, K. Badgley, S. Baeßler, et al. (Muon $g-2$ Collaboration), Phys. Rev. Lett. **126**, 141801 (2021), URL `https://link.aps.org/doi/10.1103/PhysRevLett.126.141801`.

[38] T. Aoyama, N. Asmussen, M. Benayoun, J. Bijnens, T. Blum, M. Bruno, I. Caprini, C. M. Carloni Calame, M. Cè, G. Colangelo, et al., Phys. Rep. **887**, 1 (2020), 2006.04822.

[39] J. L. Feng, K. T. Matchev, and Y. Shadmi, Nucl. Phys. **B613**, 366 (2001), hep-ph/0107182.

[40] A. Crivellin, M. Hoferichter, and P. Schmidt-Wellenburg, Phys. Rev. D **98**, 113002 (2018), 1807.11484, URL `https://ui.adsabs.harvard.edu/abs/2018PhRvD..98k3002C`.

[41] A. G. Grozin, I. B. Khriplovich, and A. S. Rudenko, Phys. Atom. Nucl. **72**, 1203 (2009), 0811.1641.

[42] Y. Ema, T. Gao, and M. Pospelov, Phys. Rev. Lett. **128**, 131803 (2022), 2108.05398.

[43] X. G. He, G. C. Joshi, H. Lew, and R. R. Volkas, Phys. Rev. D **43**, 22 (1991).

[44] R. Foot, Mod. Phys. Lett. A **6**, 527 (1991).

[45] X.-G. He, G. C. Joshi, H. Lew, and R. R. Volkas, Phys. Rev. D **44**, 2118 (1991).

[46] W. Altmannshofer, M. Carena, and A. Crivellin, Phys. Rev. D **94**, 095026 (2016), 1604.08221.

[47] I. Bigaran and R. R. Volkas, Phys. Rev. D **105**, 015002 (2022), 2110.03707.

[48] A. Crivellin and M. Hoferichter, JHEP **07**, 135 (2021), [Erratum: JHEP 10, 030 (2022)], 2104.03202.

[49] G. M. Pruna, PoS **FPCP2017**, 016 (2017), 1710.08311.

[50] A. Crivellin and M. Hoferichter, arXiv e-prints arXiv:1905.03789 (2019), 1905.03789, URL `https://ui.adsabs.harvard.edu/abs/2019arXiv190503789C`.

[51] G. W. Bennett, B. Bousquet, H. N. Brown, G. Bunce, R. M. Carey, P. Cushman, G. T. Danby, P. T. Debevec, M. Deile, H. Deng, et al. (Muon g-2), Phys. Rev. D **73**, 072003 (2006), hep-ex/0602035, URL `https://ui.adsabs.harvard.edu/abs/2006PhRvD..73g2003B`.

[52] L. Thomas, The London, Edinburgh, and Dublin Philosophical Magazine and Journal of Science **3**, 1 (1927).

[53] V. Bargmann, L. Michel, and V. L. Telegdi, Phys. Rev. Lett. **2**, 435 (1959), URL `https://ui.adsabs.harvard.edu/abs/1959PhRvL...2..435B`.

[54] H. Iinuma, H. Nakayama, K. Oide, K.-i. Sasaki, N. Saito, T. Mibe, and M. Abe, Nucl. Instr. Meth. Phys. Res. A **832**, 51 (2016).

[55] M. Haj Tahar and C. Carli, Phys. Rev. Acc. Beams **24**, 034003 (2021), 2008.12058, URL `https://ui.adsabs.harvard.edu/abs/2021PhRvS..24c4003H`.

[56] I. I. Rabi, N. F. Ramsey, and J. Schwinger, Rev. Mod. Phys. **26**, 167 (1954).

[57] P. N. Murgatroyd, American Journal of Physics **59**, 949 (1991), URL `https://doi.org/10.1119/1.16680`.

[58] S. Agostinelli, J. Allison, K. Amako, J. Apostolakis, H. Araujo, P. Arce, M. Asai, D. Axen, S. Banerjee, G. Barrand, et al., Nucl. Instrum. Meth. A **506**, 250 (2003), URL `https://doi.org/10.1016/s0168-9002(03)01368-8`.

[59] M. V. Berry, Proc. Roy. Soc. Lond. **A392**, 45 (1984).

[60] J. J. Sakurai and J. Napolitano, *Modern quantum mechanics; 2nd ed.* (Addison-Wesley, San Francisco, CA, 2011), URL `https://cds.cern.ch/record/1341875`.

[61] A. Papa, F. Barchetti, F. Gray, E. Ripiccini, and G. Rutar, Nucl. Instr. Meth. Phys. Res. A **787**, 130 (2015), ISSN 0168-9002, new Developments in Photodetection NDIP14.

[62] M. Sakurai, Ph.D. thesis, ETH Zürich (2022), dISS. ETH NO. 28992.

[63] J. Kaminski, Y. Bilevych, K. Desch, C. Krieger, and M. Lupberger, Nucl. Instr. Meth. Phys. Res. A **845**, 233 (2017), URL `https://ui.adsabs.harvard.edu/abs/2017NIMPA.845..233K`.

[64] X. Llopart, R. Ballabriga, M. Campbell, L. Tlustos, and W. Wong, Nucl. Instr. Meth. Phys. Res. A **581**, 485 (2007), URL `https://ui.adsabs.harvard.edu/abs/2007NIMPA.581..485L`.

[65] D. Barna, M. Novák, K. Brunner, C. Petrone, M. Atanasov, J. Feuvrier, and M. Pascal, IEEE Trans. Appl. Supercond. **29**, 4900108 (2018), 1809.04330.

[66] H. Noma, T. Shioda, and Y. Yoshizawa, Nuclear Instruments and Methods **184**, 587 (1981), URL `https://ui.adsabs.harvard.edu/abs/1981NucIM.184..587N`.

[67] M. Firth, E. Habel, L. Krempasky, and F. Schmeissner, Conf. Proc. C **730508**, 79 (1973).

[68] A. Yamamoto, Y. Makida, K. Tanaka, F. Krienen, B. Roberts, H. Brown, G. Bunce, G. Danby, M. G-Perdekamp, H. Hseuh, et al., Nuclear Instruments and Methods in Physics Research Section A: Accelerators, Spectrometers, Detectors and Associated Equipment **491**, 23 (2002), ISSN 0168-9002, URL `http://www.sciencedirect.com/science/article/pii/S0168900202012329`.

[69] D. Barna, Phys. Rev. Acc. Beams **20**, 041002 (2017).

[70] A. Molodyk, S. Samoilenkov, A. Markelov, P. Degtyarenko, S. Lee, V. Petrykin, M. Gaifullin, A. Mankevich, A. Vavilov, B. Sorbom, et al., Scientific reports **11**, 1 (2021).

[71] A. Jaeger, Master's thesis, ETHZ (2021).

[72] A. Stoykov, R. Scheuermann, and K. Sedlak, Nuclear Instruments and Methods in Physics Research A **695**, 202 (2012), 1107.2545, URL `https://ui.adsabs.harvard.edu/abs/2012NIMPA.695..202S`.

[73] S. Ritt, R. Dinapoli, and U. Hartmann, Nuclear Instruments and Methods in Physics Research A **623**, 486 (2010), URL `https://ui.adsabs.harvard.edu/abs/2010NIMPA.623..486R`.

[74] L. Galli, A. Baldini, P. W. Cattaneo, F. Cei, M. De Gerone, S. Dussoni, F. Gatti, M. Grassi, F. Morsani, D. Nicolò, et al., Journal of Instrumentation **9**, P04022 (2014), URL `https://ui.adsabs.harvard.edu/abs/2014JInst...9P4022G`.

[75] W. T. Scott, Rev. Mod. Phys. **35**, 231 (1963), URL `https://link.aps.org/doi/10.1103/RevModPhys.35.231`.

[76] H. Augustin, I. Perić, A. Schöning, and A. Weber, Nuclear Instruments and Methods in Physics Research Section A: Accelerators, Spectrometers, Detectors and Associated Equipment **979**, 164441 (2020), ISSN 0168-9002, URL `https://www.sciencedirect.com/science/article/pii/S016890022030838X`.

[77] H. Augustin, N. Berger, S. Dittmeier, D. M. Immig, D. Kim, L. Mandok, A. Meneses Gonzalez, M. Menzel, L. O. S. Noehte, I. Perić, et al., in *International Workshop on Vertex Detectors (VERTEX2020)* (2021), p. 010012, URL `https://ui.adsabs.harvard.edu/abs/2021vede.confa0012A`.

[78] C. Ross, M. McEwen, A. McDonald, C. Cojocaru, and B. Faddegon, Medical physics **35**, 4121 (2008).

[79] N. Berger, A. Buniatyan, P. Eckert, F. Förster, R. Gredig, O. Kovalenko, M. Kiehn, R. Philipp, A. Schöning, and D. Wiedner, Journal of Instrumentation **9**, P07007 (2014), 1405.2759, URL `https://ui.adsabs.harvard.edu/abs/2014JInst...9P7007B`.